Spring 5-15-2019

A Test of the Equivalence Principle using a Long-Period Torsion Balance

Maneesh Jeyakumar
Washington University in St. Louis

WASHINGTON UNIVERSITY IN ST. LOUIS

Department of Physics

Dissertation Examination Committee:
Ramanath Cowsik, Chair
James Buckley
Rajan Chakrabarty
Henric Krawczynski
Kater Murch

A Test of the Einstein Equivalence Principle using a Long-Period Torsion Balance

by
Maneesh Jeyakumar

A dissertation presented to
The Graduate School of
of Washington University in
partial fulfillment of the
requirements for the degree
of Doctor of Philosophy

May 2019
St. Louis, Missouri

Table of Contents

List of Figures

List of Tables

Acknowledgments

I would like to thank Professor Ramanath Cowsik for teaching and guidance, both in physics and in life. I am indebted to the members of the GEE Lab, who've helped a great deal over the years; Thank you Tsitsi, Adam, and Dawson! I would also like to thank the other members of my committee for their feedback and insights as well.

The support I've received from my friends, both here in St. Louis and back home, have been invaluable, I would not have made it this far without them! I would also like to thank my girlfriend Rebecca, and her family, who've been very supportive of me while I finished my studies.

And most of all, I would like to thank my parents for everything they've done for me.

Maneesh Jeyakumar

Washington University in St. Louis

May 2019

Dedicated to my parents.

ABSTRACT OF THE DISSERTATION

A Test of the Equivalence Principle using a Long-Period Torsion Balance

by

Maneesh Jeyakumar

Doctor of Philosophy in Physics

Washington University in St. Louis, 2019

Professor Ramanath Cowsik, Chair

The thesis describes an experimental test of Einstein's Equivalence Principle using a long-period torsion balance. The instrument was operated for a period of ~ 5 months in a remote laboratory at Tyson Research Center. The angular orientation of the balance was recorded with an autocollimating optical lever. Environmental parameters, such as temperature, pressure, and humidity, were also recorded. The thesis focuses on the analysis of this data. Accordingly, novel image processing and tracking algorithms were developed to measure the deflections of the balance over the duration of the experiment. A model of the signal arising from any violation of the equivalence principle was developed and the data was analyzed to search for such signals. Finally, the results of the analysis are presented.

Chapter 1

Synopsis

All successful theories of gravity so far have at their foundation an equivalence principle (EP) of some form. Galileo enunciated the first equivalence principle (EP) and demonstrated its validity. His measurements of the gravitational acceleration experienced by objects with differing composition and mass demonstrated that the acceleration is independent of these properties. This principle would come to be known and the Universality of Free Fall (UFF). The mathematical embodiment of UFF in Newtonian mechanics is the equivalence between the inertial mass and the passive gravitational mass. However, the language used to define the UFF will evolve over time and highlights different theorical perspectives. In Chapter 2 begins with an overview of the historical understanding and interpretation of equivalence principles in theories of gravity. We will formally define the different EPs and discuss its implications of its validity or violation.

The most successful theory of gravity thus far is General Relativity (GR). The foundational assumption underlying is the Einstein Equivalence Principle (EEP). EEP is composed of three subprinciples. The three subprinciples are called the Weak Equivalence Principle (WEP), Local Lorentz Invariance (LLI), and Local Position Invariance (LPI). The WEP is equivalence to the UFF but defined in the language of relativity. The three subprinciples of the EEP are usually defined as three independent theoretical principles with non-overlapping empirical consequences. However, there are compelling arguments have been made for a deeper interconnectivity between them have been made. In 1960, Leonard I. Schiff made such an argument. Schiff's conjecture postulates that *..." any complete, self-consistent theory of gravity that embodies the WEP must also necessarily embody EEP*" [2,3]. The goal of the experiment described in thesis is to search for violations of the EP with a higher degree of sensitivity, and thereby constrain the strength of EP-violations. The result of this experiment will place limits on the violation of the Weak Equivalence Principle (WEP) and, given Schiff's conjecture, place limits on the Einstein Equivalence Principle (EEP) as well. A brief survey of the field is provided, and historically important experiments are discussed.

Chapter 3 will introduce the concepts underlying torsion balance experiments. It begins by presenting a model of the signal produced by EP-violations in the gravitational field of the sun. The model is used to calculate torque due an EP violation over the course of a year. A model of the torsion balance is used to study the response of the balance to this torque. The torsion balance is modelled as a damped, driven, harmonic oscillator. The equation of motion is solved to produce an expression for the angular displacement of the balance.

This model is also used study the thermal noise spectrum of balance. The thermal noise spectrum is derived from the equation of motion using the fluctuation-dissipation theorem.

The fundamental thermal limit is obtained by calculating the power spectrum of the thermal torque acting on the balance.

The high sensitivity of the balance requires that the experiment be located as far as possible from external disturbances that could drown out the signal. This problem is addressed by locating the instrument in a bunker at the Tyson Research Center, near Eureka, Missouri. In Chapter 4, the major components of the instrument and the experimental setup inside this bunker is described in detail. The design and construction of the balance is described first, followed by a description of the fiber used to suspend the balance. The relevant properties of the fiber, such as its torsional constant, are also calculated. The suspension system attaches to the fiber and executes the mechanical damping of the amplitude of the balance oscillations. This system and its components will be described.

In order to operate the balance with the required sensitivity, it must be isolated from the environment as must as possible. To this end, the balance and its suspension system are contained within a vacuum chamber, which is pumped down to pressures on the order of 10^{-9} Torr. The vacuum system is briefly described in Chapter 4 as well.

Chapter 4 also features section on the autocollimating optical lever (autocollimator), a highly precise goniometer used to track the torsional oscillations of the balance. The autocollimator measures the balance deflections using an optical system that creates an image whose position depends on the angular orientation of the balance.

Chapter 5 will discuss the efforts to develop a robust image processing algorithm to analyze this image and track its movements with the highest attainable resolution.

Chapter 6 presents the data collected by the instrument and focuses on the data analysis methodology. The key ideas and concepts underlying the analysis are introduced in this chapter. Then each step of the analysis procedure is discussed in detail and applied to the torsion balance data and the result of the analysis is presented. The appendix to Chapter 6 discusses some of the various methods investigated during the development of the analysis methodology.

Chapter 2

The Equivalence Principle

ABSTRACT:

This chapter will discuss the Equivalence Principle and motivate experiments testing its validity. The equivalence principle is introduced be providing historical context on its conception and evolution over time. Next, we discuss the fundamental role of the equivalence principle in modern physics and why it requires further experimental validation. This chapter concludes with a discussion of past and future experimental tests of the equivalence principle.

2.1 Historical Background

It had been believed, since Aristotle, that the velocity with which an object falls in a vacuum is directly proportional to its weight. In the 16th century, Galileo Galilei proved this notion false through experimentation. His measurements of the speed of balls rolling down an incline demonstrated that the mass of the balls had no discernable effect on the measurement. This one was one of the first tests of the Universality of Free Fall (UFF), a concept that would eventually evolve into the Einstein Equivalence Principle (EEP), the foundational assumption that lies at the heart of general relativity.

Newton's Laws of Motion and the Law of Universal Gravitation would provide the theoretical underpinning and mathematical framework with which the observation of the UFF could be understood. Newton's 2nd law of motion relates the mass of an object to its motion in response to an applied force. The property of an object that governs its response when acted upon by an external force is defined as its inertial mass, succinctly stated by the equation:

$$F = m_I a \tag{2.1}$$

Similarly, the Law of Universal gravitational force relates the attractive force felt between two objects is directly proportional to the product of their passive gravitational mass; a property possessed by every object. The Law of Universal Gravitation is written as:

$$F = \frac{G m_G M_G}{R^2} \tag{2.2}$$

The acceleration of an object in response to a gravitational force can be found be from these two equations:

$$a = \frac{GM_G}{R^2}\left(\frac{m_G}{m_I}\right) \tag{2.3}$$

In the framework of Newtonian Mechanics, the Equivalence Principle (EP) states that the ratio of the inertial mass of an object (m_I) to its passive gravitational mass (m_G) is equal or a constant for all objects. (A universal constant which can be set to unity by choosing the units of measurement). If true, this implies:

$$a_{gravity} = \frac{GM_G}{R^2} = g \tag{2.4}$$

In the case of an object falling the gravitational field of the Earth, the Equivalence Principle directly implies the Universality of Free Fall. While Newton asserted the validity of the EP, he also realized the importance of experimentally justifying this assumption. The Newton-Bessel test of the EP searches for violations of the EP using simple pendulums of equal length, but with bobs of differing composition (see Figure 2.1). Newton, and later Bessel, measured the period of the oscillation of the pendulums. The period of oscillation depends on the ratio of the inertial mass ($m_{1,2}^I$) to passive gravitation mass ($m_{1,2}^G$) by:

$$T_{1,2} = 2\pi\left(m_{1,2}^I \Big/ m_{1,2}^G\right)^{1/2}\sqrt{l/g} \tag{2.5}$$

Newton tested the UFF for celestial bodies by studying the Earth-Moon system in the gravitational field of the sun. He showed that if the Earth and the Moon have different accelerations, violating the UFF, then the orbit of the moon will be polarized in the direction of the sun.

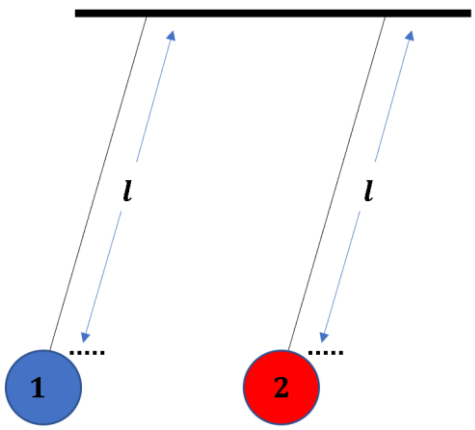

Figure 2.1: The Newton-Bessel test measures the period ($T_{1,2}$) of oscillation (in the small angle regime) of simple pendulums. The pendulums have equal length ($\boldsymbol{l}$) but have bobs that differ in composition. If the ratio of inertial mass to gravitation mass differ for the different bobs, then the period of their oscillations will not be equal: $T_1 \neq T_2$

A huge leap in the precision of tests of the EP was made in the late nineteenth century by Baron Roland v. Eötvös when he introduced his torsion balance to tests of the EP (see Figure 2.2). A conceptual diagram of Eötvös's torsion balance experiment is depicted in Figure 2.3. The test bodies at the ends of the balance are composed of different materials and experience a gravitational force directed towards the center of the Earth:

$$\vec{F}^{g}_{1,2} = m^{G}_{1(2)} g \tag{2.6}$$

The balance also experiences a centrifugal force due to the rotation of the earth:

$$\vec{F}^{Inertial}_{1(2)} = m^{I}_{1(2)} \omega^{2}_{\oplus} R_{\oplus} \cos\theta \tag{2.7}$$

The two forces acting on the test bodies create a deflection from the vertical axis. If the ratio of the inertial and gravitational masses is different for the two test bodies, then the deflection of each mass differs, creating a net torque on the balance that can be measured, by rotating the balance assembly by a 180^{o} [42]. Eötvös's paper was published posthumously in the early 20th century.

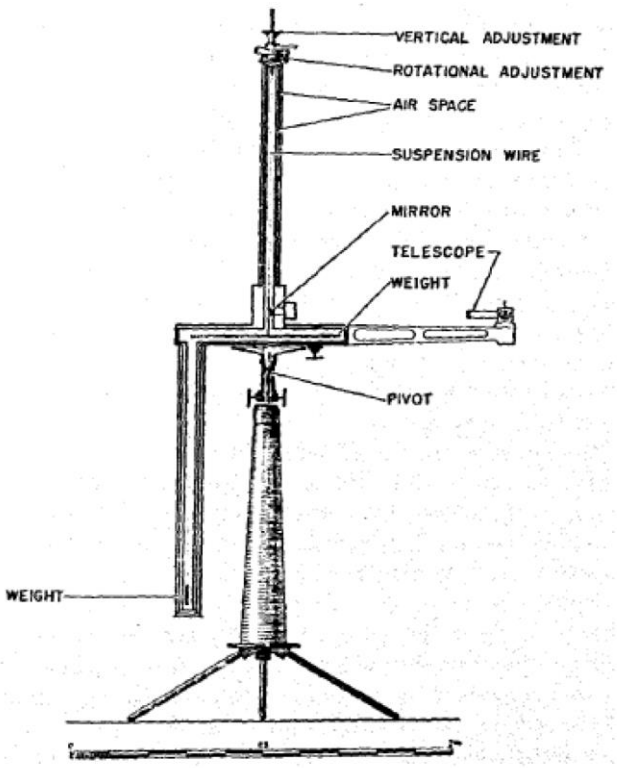

Figure 2.2: A drawing of Baron Eötvös's torsion balance, used to search for violations of the EP. Obtained from [28].

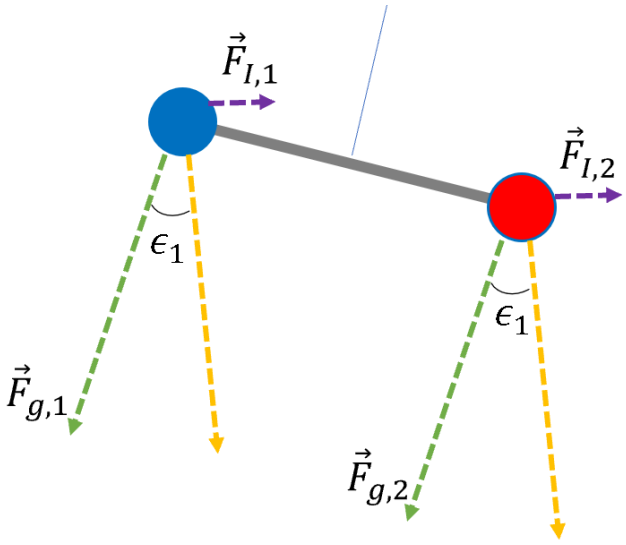

Figure 2.3: A diagram depicting the Eötvös experiment.

The Eötvös experiment established the validity of the Equivalence Principle until Einstein's formulation of General Relativity (GR) and the effort to unify GR with quantum mechanics demanded higher precision tests of the EP.

2.2 Modern Understanding of the Equivalence Principle

The Equivalence Principle in modern physics is understood as the Einstein Equivalence Principle, the foundational assumption of all "metric" theories of gravity – theories that describe the phenomenon of gravity as the curvature of spacetime [2-4,43]. The EEP lies at the heart of general relativity, and the defines the mathematical structure of the theory.

Simply stated, the Einstein equivalence principle asserts the universality of free-fall and that all non-gravitational laws of physics are unchanged in a gravitational field. It is neither derived nor explained by other theories or fundamental principles. The credibility of the EEP relies entirely on the results of experimental tests of its implications. One of these implications is that all non-gravitational interactions contribute equally to the inertial mass (m_I) and the passive gravitational mass (m_G). The EEP also implicitly assumes that falling objects are bound by non-gravitational forces only.

The strong equivalence principle (SEP) asserts that gravitational interactions similarly contribute equally to the inertial and gravitational masses. Laboratory tests of gravity can only test the WEP, constraints on violations of the SEP must come from observations of the dynamics of celestial bodies, where the gravitational self-energy of the bodies involved are substantial enough to make measurable predictions [13].

In this chapter, we will follow Will's formulation of the Einstein Equivalence Principle [2,3]. The EEP is comprised of three sub-principles:

The Weak Equivalence Principle (WEP)

The trajectory of a non-spinning freely falling test mass is independent of its internal structure and composition. Also known as the universality of free fall, it requires that all interactions, except gravitational ones, contribute equally to the inertial and gravitational mass.

Local Lorentz Invariance (LLI)

The outcome of all non-gravitational experiments is independent of the velocity of the locally inertial frame in which they are carried out. (A "locally inertial frame is a freely falling", non-rotating, reference frame small enough that inhomogeneities in external fields are negligible.)

Violations of LLI imply the existence of a universal rest frame and can by tested by searching for shifts in energy levels of atoms (Hughes-Drever experiments) that due to Lorentz-non-invariant electromagnetic interactions associated with the universal rest frame. One interpretation of the such a violation is an anisotropy in the inertial mass in the atom on the order of $\delta m_I^{ij} \sim \sum_A \delta^A \frac{E^A}{c^2}$, where E^A is the energy of a physical interaction, labelled by A, and δ^A is a dimensional parameter that measures the strength of the anisotropy. If we suppose that the violation of Lorentz invariance occurs due to the change in the speed of light relative to the limiting speed of test particles (c_0), then Lorentz violation can be measured by parameter $\left(\frac{c_{light}^2}{c_0^2} - 1\right)$ [2,3].

Local Position Invariance (LPI)

The outcome all non-gravitational experiments is independent of the position (of the locally inertial frame) in spacetime in which it is carried out. LPI can be tested by measuring the differences in the ticking rate of two identical clocks in two different frames, such as the gravitational redshift experiment. If LPI holds, the frequency shift, Z is given by: $Z = \Delta\nu/\nu = \Delta U/c^2$. ΔU is the difference in the Newtonian potential between the two rest frames. If LPI is violated, then $Z = (1 + \alpha)\Delta U/c^2$, where α is a parameter that depends on the clock [2,3].

An equivalent definition of WEP, LLI and LPI places emphasis on the invariance of the laws of physics [4,43]: "*all non-gravitational laws of physics take some standard form in a locally inertial frame that is independent of the velocity and its location in spacetime".*

The validity of the WEP implies the existence of a set of "preferred" trajectories through spacetime that depends only on the initial spacetime position and velocity [2,4,43].

2.2.1 Testing the Weak Equivalence Principle

If the WEP is valid, the rest mass-energy of the constituent particles of objects as well as the interactions between these constituents contribute equally to the inertial and passive gravitational mass. This equivalence between inertial and gravitational mass implied that the acceleration of an object in a gravitational field is independent of the mass of the object, and thereby independent of the particles and physical interactions that constitute object and bind it together.

A violation of the WEP can be measured by comparing the spacetime trajectories of two test bodies. A violation is observed if the ratio of the inertial mass and gravitational mass are

no longer equivalent. This implies that the energies of the different physical interactions that define the internal structure of the test body do not, in general, contribute equally to the inertial and gravitational mass. This property can be described in terms of a dimensionless parameter characterizing the "strength" of the difference in contribution to inertial mass and passive gravitational mass as:

$$m_G = m_I + \sum_A \eta^A \frac{E^A}{c^2} \tag{2.8}$$

E^A is the energy of a physical interaction (such as electromagnetism), labelled by A, and η^A is the dimensionless parameter that determines the extent to which the interaction A violates the WEP.

The overall violation of the WEP by a test body is characterized by the Eötvös parameter, named after Baron Eötvös who first formulated the parameter to interpret the results of his experiment. The Eötvös parameter is a dimensionless measure of the strength of WEP violation, it is obtained from the difference in the ratio of inertial mass to the passive gravitational mass of two objects (labelled 1 and 2):

$$m_{I,1(2)} a_{1(2)} = m_{G,1(2)} g = \left(m_{I,1(2)} + \sum_A \eta^A \frac{E^A_{1(2)}}{c^2} \right) g \tag{2.9}$$

$$a_{1(2)} = \left(1 + \sum_A \eta^A \frac{E^A_{1(2)}}{m_{I,1(2)} c^2} \right) g \tag{2.10}$$

The Eötvös parameter is given by:

$$\eta_{EP} \equiv \frac{|a_1 - a_2|}{\frac{1}{2}|a_1 + a_2|} = \sum_A \eta^A \left(\frac{E^A_1}{m_{I,1} c^2} - \frac{E^A_2}{m_{I,2} c^2} \right) \tag{2.11}$$

2.2.2 Schiff's Conjecture

While it might appear that the three subprinciples of the EEP are unrelated, due to the role it plays in constraining the mathematical formulation that can be used to describe the phenomenon of gravity, it has been theorized that there may be a deeper connection between the WEP, LLI, and LPI [2-4,7,43,50]. In 1960, Leonard Schiff conjectured that violations of WEP will also imply violations of the LLI and LPI [5]. A test of the WEP is therefore also a test of the EEP. This idea has been developed by Dicke, Nordtvedt, Will and others who have made compelling theoretical argument for this validity [2-4,13-14,19-21,28,43-44].

2.2.3 Motivations for Further Study

The unification of GR with the Standard Model is greatest challenge facing modern physics. Over the decades various theoretical models have been formulated, and nearly every single one of them predict a violation of the WEP at some level [19-21]. Tests of the WEP at ever higher levels of precision are required to constrain and guide theoretical studies.

Tests of the equivalence principle are also among the most precise tests of GR to date [2-4,19-21,44]. Given the fundamental role of GR in our understanding of gravity, its foundations must be subjected to the most stringent experimental tests.

Dark matter and dark energy provide further motivations for further study of the equivalence principle. Current measurements of dark matter predict that it comprises nearly a quarter of the energy density of the universe, and nearly 85% of the matter in the universe [46]. Yet we currently have no experimentally verified knowledge of its nature other than that it is composed of matter that does not interact electromagnetically with ordinary matter. Theoretical

models of the substance have raised the possibility that dark matter may non-gravitationally interact with ordinary matter. Tests of the equivalence principle can place constraints on such interactions, as well as constraining violations of the WEP from dark matter within our galaxy [22,38,46].

2.3 Survey of Laboratory Tests of the Equivalence Principle

In early 1960s, a significant leap forward in tests of the WEP was made by Roll, Krotkov, and Dicke [28]. The Dicke experiment searched for violations of the equivalence principle in the gravitational field of the sun. Called the Solar Attractor approach, this experiment allowed Dicke *et. al* to place a limit three orders of magnitude better than the limit placed by Eötvös [4,28]. While the gravitational acceleration due to the sun is less than the centrifugal acceleration produced by the rotation of the earth, the earth's rotation modulates any EP-violating signal due to the sun. Technological advances and the ability to monitor data over long spans offered great advantages in detecting EP-violations [28]. Dicke placed a limit of EP-violations at $\eta^{EP}_{Al,Au} = 3 \times 10^{-11}$. In 1972, Braginsky, using the Solar Attractor approach, was able to improve this limit to $\eta^{EP}_{Al,Pt} = 9 \times 10^{-13}$ [9].

In addition to the solar approach, tests of the EP using a rotating torsion balance were developed by the Eöt-Wash group at the University of Washington [8,10-12,22-23,30]. This torsion balance experiment uses a torsion balance mounted on a turntable and rotated at uniformly rate. In this approach, a local gravitational source producing a larger gravitational acceleration can be used as the attractor. The modulation of the signal can also be chosen,

allowing them to set a rate far from the diurnal or sidereal rates that are associated with astronomical sources as well as various sources of noise (e.g. diurnal temperature swings). The downside of the method is that the rotation rate must be precisely controlled to ensure uniformity. In addition, local gravitational gradients must be measured to a very high degree of precision in order to account for and remove their influence.

In addition to terrestrial experiments, there are space-based tests of the equivalence principle currently underway. One such experiment is MircroSCOPE; this experiment will test the WEP in Earth's gravitational field between two test bodies of different composition in space. The test masses are highly sensitive differential accelerometers launched into space aboard minisatellites [51].

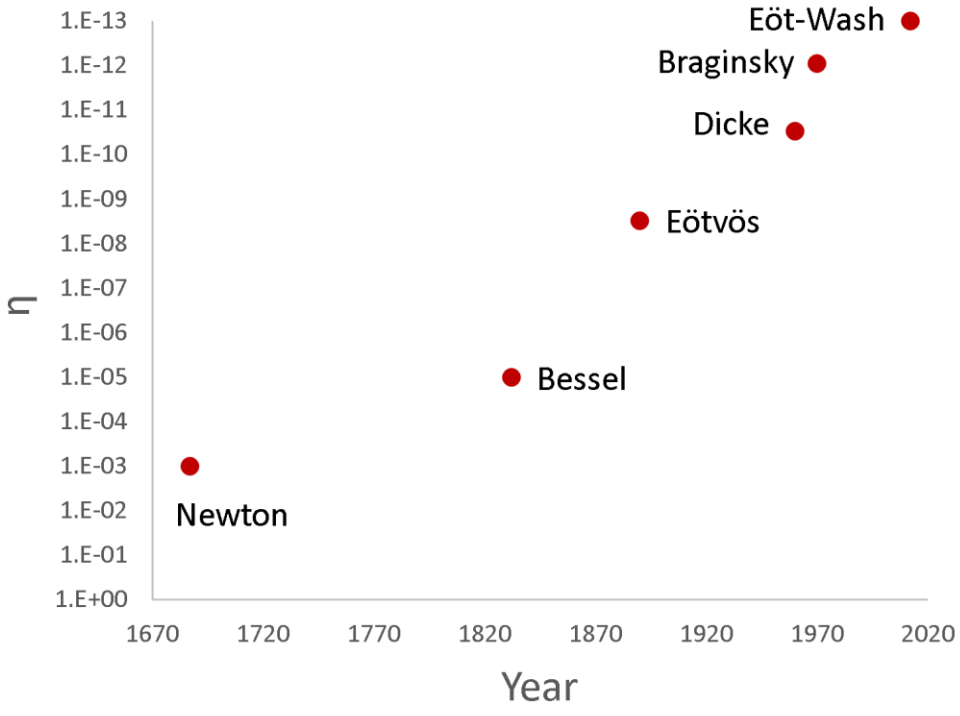

Figure 2.4: The various limits placed on violations of the equivalence principle by different investigators over the years.

Chapter 3

Torsion Balance Experiments

ABSTRACT:

This chapter will describe the conceptual basis of torsion balance experiments. The torsion balance used in this experiment and its application to measurements of WEP violations is investigated. Then we will investigate the thermal properties of the balance

The torsion balance is a highly sensitive detector of mechanical torques. It has been used to search for oil fields and mines and to study the Earth's physical properties. Its utility lies in the design. The torsion balance responds to forces acting in its horizontal plane and is insensitive to the direct gravitational attraction of Earth. The fiber that suspends the balance orients itself along the direction of gravity and precisely cancels it out. The balance will still be sensitive to gravitational gradients with components in the horizontal plane of the balance, and they can introduce systematic errors in measurements. The balance used in this experiment is designed to minimize coupling to gravitational gradients.

The body of a torsion balance designed to measure violations of the Weak Equivalence Principle (WEP), in general, consists of an azimuthally symmetric framework of beams with test bodies of equal mass but differing composition placed at the ends of beams. If the test bodies have a composition dependent response to a gravitational field there will be a net torque acting on the balance, and this torque can by related to the Eötvös parameter characterize the strength of a WEP violating interaction.

The torque on the balance is extracted from the measurements of the angular displacement of the balance by a position sensitive detector. In this experiment, we use an autocollimating optical lever. By monitoring the angular displacement of the balance over time, the torque can be estimated and the Eötvös parameter for the violation of the WEP measured. The modulation of the signal by uniformly rotating the balance with respect to the attractor produces a sinusoidal signal that can be detected with high precision [9-11,22-23,25].

Another common method of measurement of torque works by nullifying the torque using a feedback circuit. For example, the change in the motion of the balance as in the previous

method is observed using an optical lever, but the measured displacement is used as the input in a PID loop controlling electrodes that apply a torque to cancel out the motion due to the external torque. The external torque is inferred from the voltage on the electrodes. The torque can also be inferred by measuring changes in the free period of the balance [8-12,11,24,25,].

3.1 The Torsion Balance and Model of the Expected Signal

Our balance is cross-shaped and has of four test bodies of approximately equal mass, with the two masses at the end of each balance arm differing in composition. This arrangement forms a compositional dipole. This cross-shaped balance has cylindrical symmetry about the fiber axis and top-bottom symmetry about the horizontal plane of the balance. These symmetries reduce the sensitivity of the balance to horizontal gradients because the quadrupole moment tensor of the balance is (ideally) diagonal: $I_{xx} = I_{yy} = {}^{1}/_{2}\, I_{zz}$ [6,8-12]. Imperfections in construction can lead to asymmetries that will couple to horizontal gradients and lead to a torque acting on the balance. However, a static gradient will generate a torque that does not change with time. It will be shown in Chapter 6 that the analysis procedure filters out only those torques that vary in time with a period of $\sim$ 1 day. The torsional balance also has other modes of oscillation (e.g. pendular modes and violin modes) besides the torsional mode on the horizontal plane of the balance. These oscillations can be reduced and eliminated using a magnetic damping mechanism described in Chapter 4.

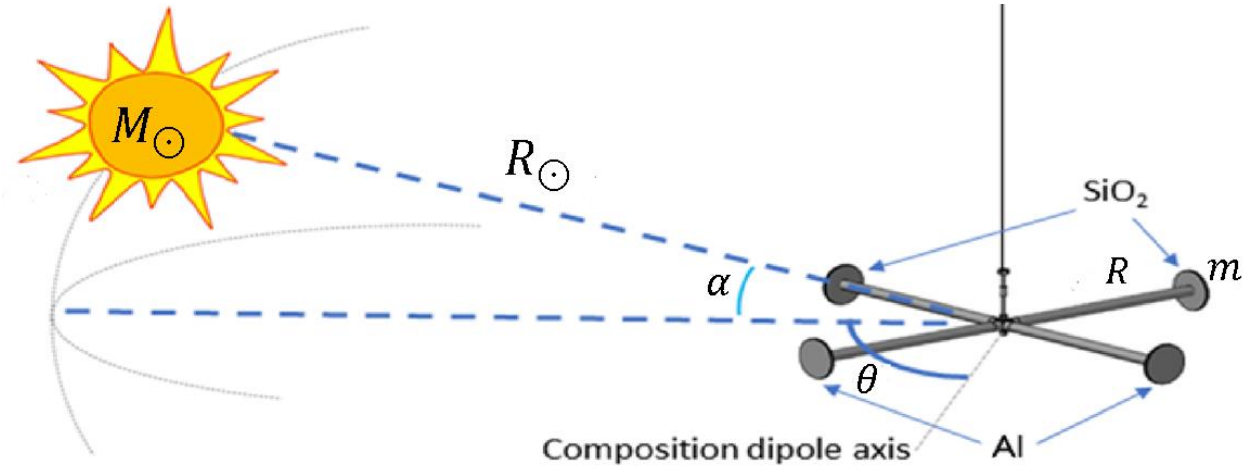

Figure 3.1: Torsion balance in the field of the sun. R is the length of the balance arms, m the mass of the test bodies, $\theta$is the angle between the composition dipole and the component of the line of sight to the sun that on the horizontal plane, α is the elevation of the sun over the horizonal plane.

3.1.1 Measuring WEP Violations using the Torsion Balance

A torque due to violation of the WEP is generated by the composition dependent acceleration of the test masses in a gravitational field. The compositional dipole formed by the arrangement of the masses allow this torque to be formulated analogously to the torque on an electric dipole in an external electric field (see Figure 3.2). The compositional dipole, $\vec{d}$, is:

$$\vec{d} = 2(m_A - m_B)\vec{r} = \frac{2R}{\sqrt{2}}\,(m_A - m_B)\hat{r} \tag{3.1}$$

R is the length of the balance arms.

The composition dependence of the torque on the balance is demonstrated by parameterizing m_A and m_B in terms of a mass "pseudo-charge":

$$m_A = m(1 + \tilde{\Delta}) \tag{3.2a}$$

$$m_B = m(1 - \tilde{\Delta}) \tag{3.2b}$$

Plug Equations 3.2 a-b equations into the expression for the dipole moment:

$$\vec{d} = \frac{2m(2\tilde{\Delta})R}{\sqrt{2}}\,\hat{r} \tag{3.3}$$

Consider a torque due to a violation of the WEP in the gravitational field of the sun. The amplitude of the torque is given by:

$$\tau_{EP} = \left|\vec{d} \times \vec{a}_{\odot}\right| = \frac{2a_{\odot}m(2\tilde{\Delta})R}{\sqrt{2}}\sin\theta \tag{3.4}$$

The mean acceleration induced by the gravitational field of the sun on the balance is: $a_{\odot} = {(a_A + a_B)}/{2}$. The differential acceleration due the composition dependent mass pseudo-charge is $\Delta a_{EP} = a_{\odot}(2\tilde{\Delta})$. It follows that the Eötvös parameter is equal to $(2\tilde{\Delta})$.

Taking the elevation of the sun into account, the amplitude of the EP-violating torque in the $\hat{z}$ direction is given by:

$$\tau_{EP} = \eta_{EP} D a_{\odot} \sin\theta \cos\alpha \tag{3.5}$$

D is the compositional dipole moment: $D = mR\sqrt{2}$.

The differential acceleration of the balance due to an EP-violating force is obtained by calculating the balance acceleration. Setting $\Delta a_{EP}(t) = \eta_{EP} a_{\odot}\cos(\alpha)\sin\theta$:

$$\tau_{EP} = I\ddot{\phi}(t) = D(\Delta a_{EP}(t)) \tag{3.6}$$

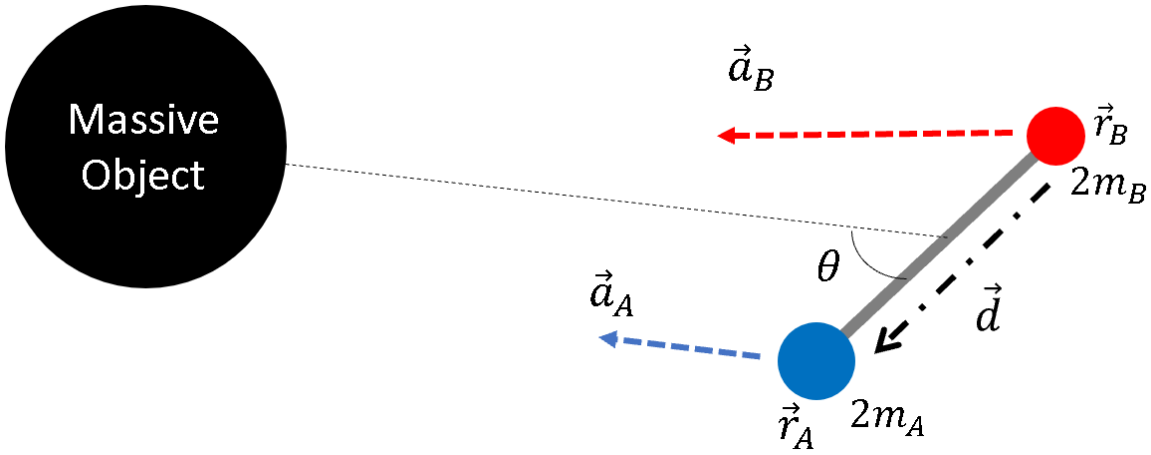

Figure 3.2: The compositional dipole equivalent of our balance. θ is the angle between the compositional dipole and the component of the line of sight to the massive object generating the gravitational field on the horizontal plane of the balance.

$$\Delta a_{EP}(t) = \frac{I}{mR\sqrt{2}.}\ddot{\phi}(t) \tag{3.7}$$

θ and α change with the rotation of the earth, leading to a torque with modulated at the diurnal frequency ($f_d = 1/86400s$). If the amplitude of the differential acceleration, Δa_{EP}, is:

$$\Delta a_{EP} = \eta_{EP} a_{\odot} \tag{3.8}$$

The Eötvös parameter is:

$$\eta_{EP} = \frac{\Delta a_{EP}}{a_{\odot}} \tag{3.9}$$

3.1.2 The Torsion Balance as a Damped Harmonic Oscillator

In order to gain an understanding of the response of the torsion balance to an EP-violating signal, we model the balance as a damped harmonic oscillator driven by a sinusoidal torque and a fluctuating thermal torque:

$$\ddot{\phi} + 2\beta\dot{\phi} + \omega_0^2\phi = \frac{\tau_{EP}}{I}\cos\omega_s t \tag{3.10}$$

I is the moment of inertia, ϕ is the angular displacement of the balance, β is a damping parameter, and ω_0 is the natural frequency of the balance. See Chen and Cook for a detailed derivation of the solution to this equation [24].

We make the following substitutions and approximations: $I = {\kappa_f}/{\omega_0^2}$ (where κ_f is the torsional rigidity of the suspension fiber) and $Q = {\sqrt{\omega_0^2 - 2\beta^2}}/{2\beta} \approx {\omega_0}/{2\beta}$.

The particular solution of this equation is:

$$\phi_p(t) = A(\omega_s)\,\frac{\tau_{EP}}{\kappa_f}\cos(\omega_s t - \delta) \tag{3.11}$$

Where δ is the phase lag of the balance response:

$$\delta = \tan^{-1}\left(\frac{{\omega_s\omega_0}/{Q}}{(\omega_0^2 - \omega_s^2)}\right) \tag{3.12}$$

In our experiment, $\delta = \tan^{-1}\left(\frac{{\omega_s\omega_0}/{Q}}{(\omega_0^2 - \omega_s^2)}\right) \approx {\omega_s}/{\omega_0 Q} \approx 0$.

$A(\omega)$ is equal to:

$$A(\omega) = \frac{\omega_0^2}{\sqrt{\left(\omega_0^2 - \omega_s^2\right)^2 + \left(\frac{\omega_s \omega_0}{Q}\right)^2}} \tag{3.13}$$

3.1.3 The Expected Signal

The balance used in this experiment has a natural period of approximately 12,700s, or $\omega_0 \approx 5 * 10^{-4}$ rad s^{-1}, a torsional constant of $k_f \sim 9 * 10^{-9}$ N m rad^{-1}, and a $Q \approx 800$. Using these parameters, we will investigate the expected angular deflection of the balance in the case of an EP-violating torque with a frequency of one solar day, $\omega_s = 7.27 * 10^{-5}$ rad s^{-1}. The behavior of the balance to an external torque obeys Hooke's Law to a high degree of accuracy ($A(\omega_s) \cong 1$ for our balance):

$$\phi = {}^{\tau_{EP}}/_{\kappa_f} \tag{3.14}$$

τ_{EP} is calculated from Equation 3.5. The expected deflection due to an EP-violating signal with an Eötvös parameter on the order of $\eta_{EP} \sim 10^{-14}$ is shown in Figure 3.3a-b. The corresponding amplitude spectral density of this signal is shown in Figure 3.4.

Figure 3.4 shows that a larger expected deflection will be produced by orienting the composition dipole along the N-S axis. Orienting the balance along the E-W axis reduces the expected deflection by a factor of ~ 0.625.

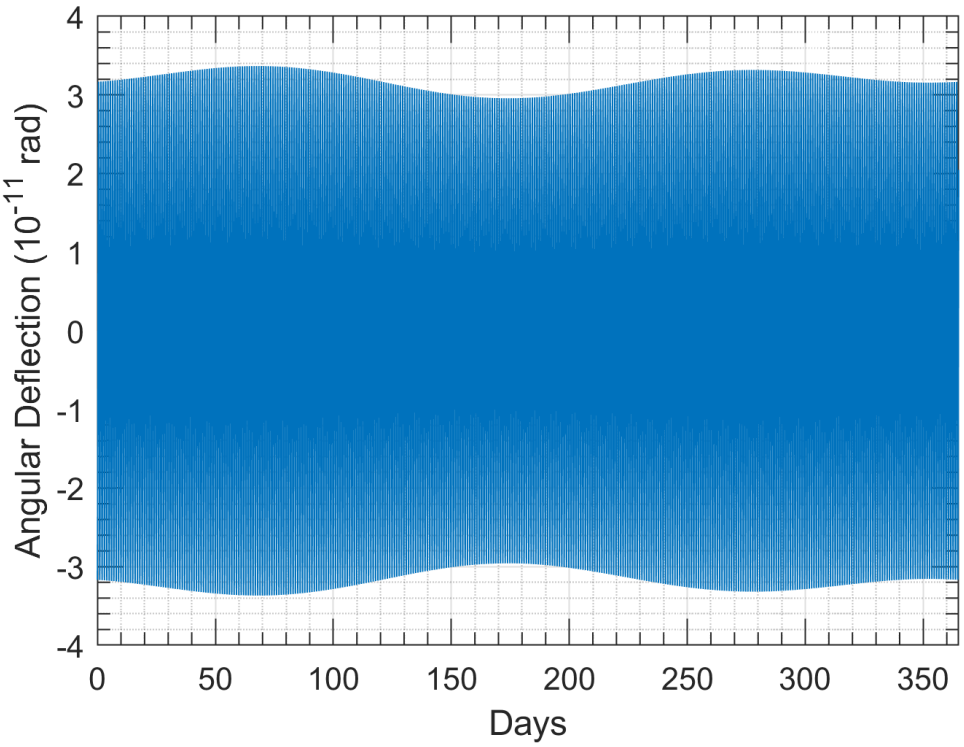
Angular Deflection (10^{-11} rad)
4
3
2
1
0
-1
-2
-3
-4
0
50
100
150
200
250
300
350
Days

(a)

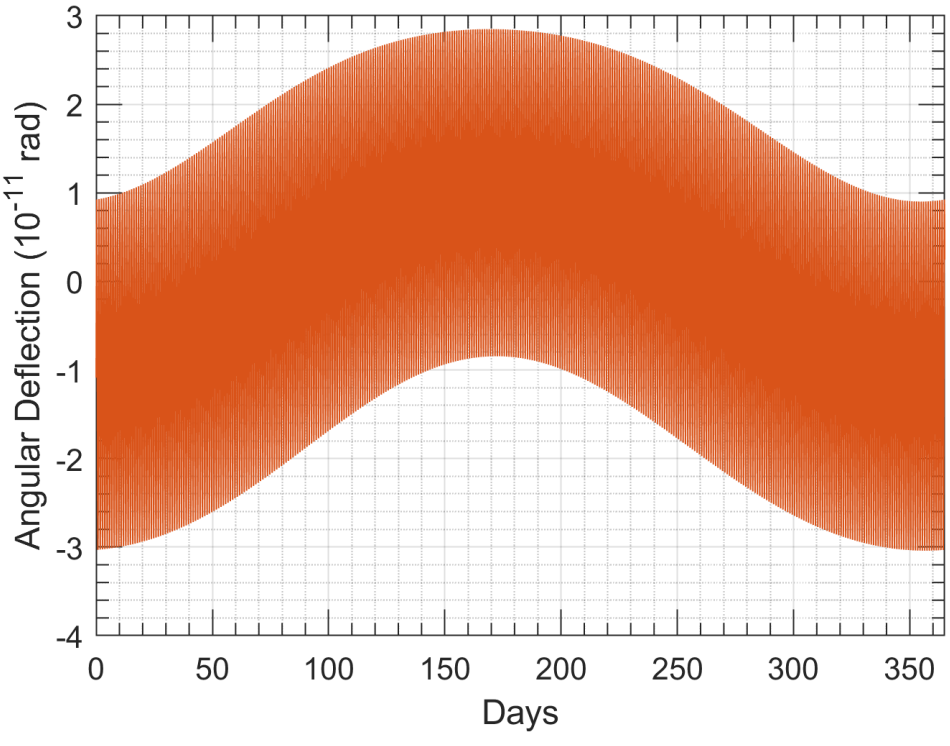
Angular Deflection (10^{-11} rad)
3
2
1
0
-1
-2
-3
-4
0
50
100
150
200
250
300
350
Days

(b)

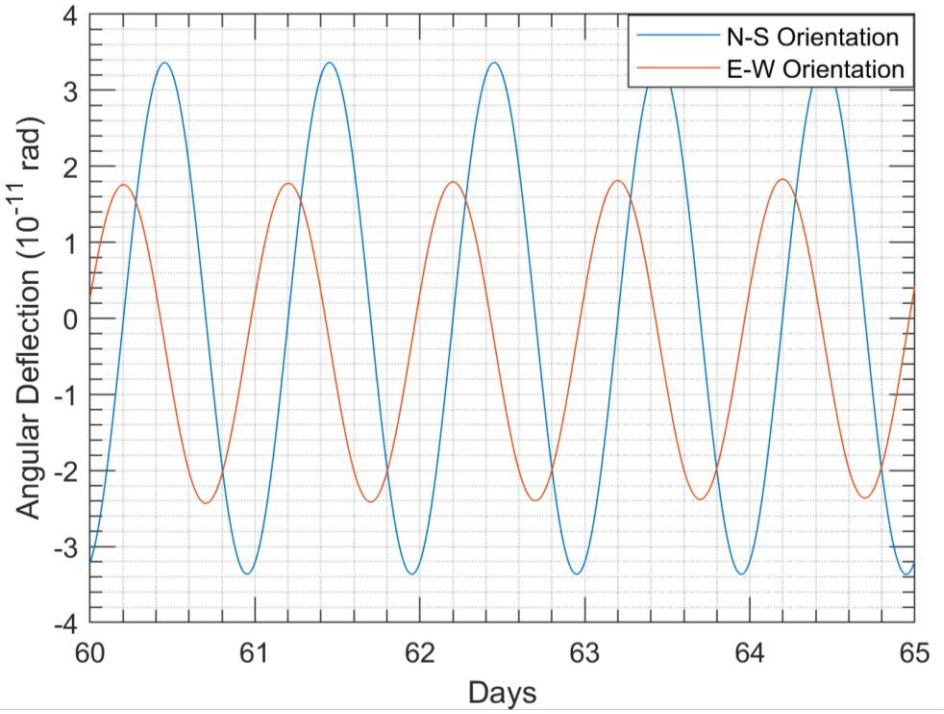

(c)

Figure 3.3: A plot of the expected angular deflection of the balance due to an EP-violating signal at $\eta_{EP} \sim 10^{-14}$ in the field of the sun. The plot begins on Jan 1, 2018 00:00:00 (UTC) and ends Dec 31, 2018 23:50:00 (UTC). The solar data was obtained from NASA's JPL Horizons website [41]. (a) Balance oriented along the N-S axis (b) Balance oriented along the E-W axis. (c) A 5-day segment of the expected deflection.

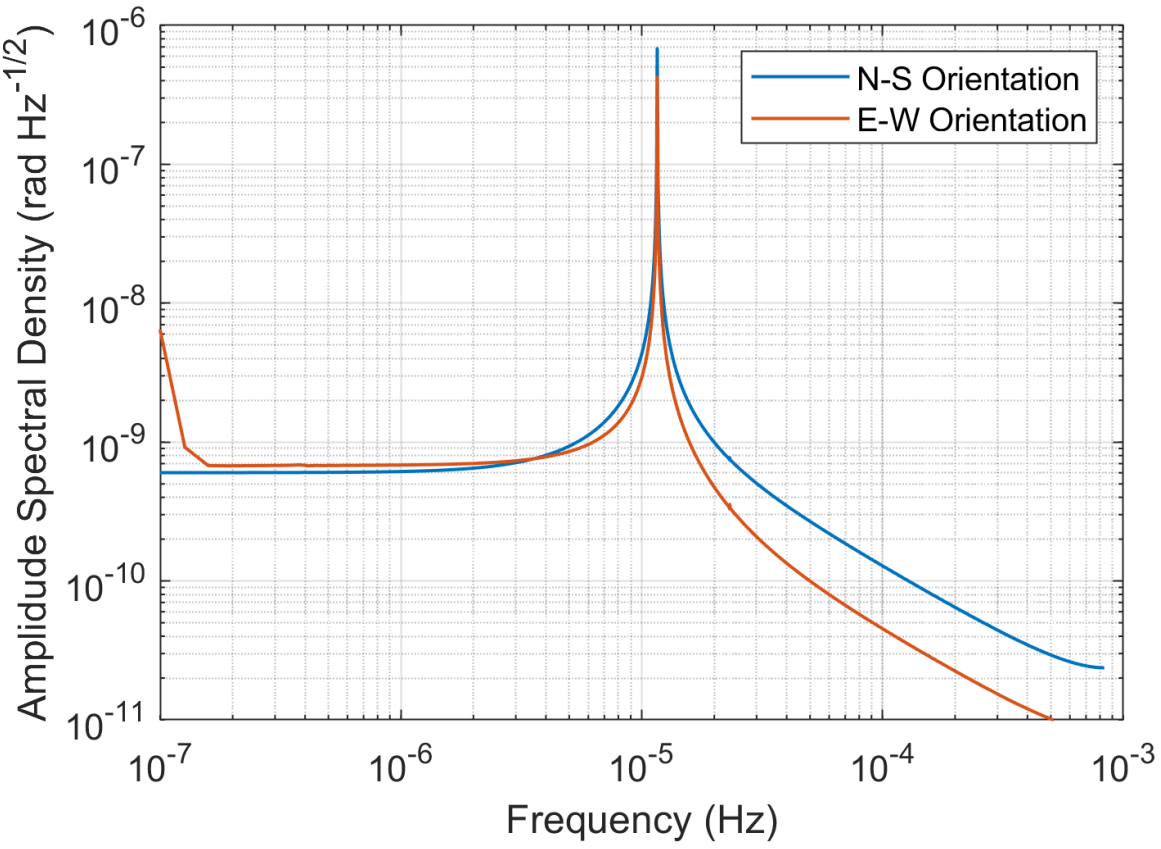

Figure 3.4: The amplitude spectral density of the expected deflection of the balance in the N-S and E-W orientations for a violation of the equivalence principle at the η_{EP}~10^{-14} level. In producing this plot, a $Q \approx 800$ (obtained from the balance data) was used.

3.2 Thermal Noise Spectrum

Thermal fluctuations place a fundamental limit on the resolution of measurements of the angular displacement of the balance. Thermal fluctuations can arise from interactions between the balance and an extrinsic noise source, e.g. dissipation due to eddy currents and drag forces, or from internal dissipation, e.g. due to internal friction in the fiber

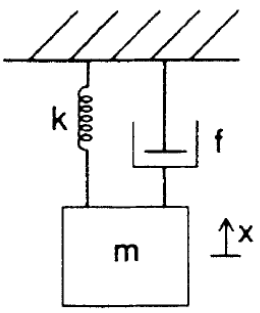

Figure 3.5 A mechanical oscillator, analogous to the torsion balance. The parameter f is the damping parameter, k is the spring constant, m is the mass. They are analogous to β, κ_f, and I, respectively, in the torsion balance system. Reproduced from [29].

In investigating the effects of these thermal fluctuations, we will follow Saulson and Callen's derivation of the thermal limit for a low-dissipation oscillator using the fluctuation-dissipation theorem [8-12,23,29,33-34]. This treatment is analogous to the analysis of thermal fluctuations in mechanical oscillators (see Figure 3.5 [29,30]. The differential equation for the torsion balance is:

$$I\ddot{\phi} + 2\beta\dot{\phi} + \kappa_f\phi = \tau_{th} \tag{3.15}$$

The β term is the damping parameter.

The fluctuation-dissipation theorem is used to derive the power spectrum of the thermal torque acting on the balance. For a single-mode oscillator whose suspension fiber has a torsional constant κ_f, and has a quality factor Q, the power spectral density of the thermal torque is given by [29,35]:

$$\tau_{th}^2(\omega) = 4k_B T R(\omega) \tag{3.16}$$

Where the mechanical resistance, $R(\omega)$, is the real part of a complex mechanical impedance, $Z(\omega)$: $R(\omega) \equiv \mathrm{Re}[\,Z(\omega)]$. k_B is the Boltzmann's constant and T is the absolute temperature.

The mechanical impedance is the measure of the resistance of the oscillator to motion when subjected to a harmonic force. It is defined as: $Z \equiv \tau/\dot{\phi}$, where τ is the applied force. The power spectral density of the angular deflections of the balance due to thermal fluctuations is given by:

$$\phi_{th}^2(\omega) = {}^{4k_B T Y(\omega)}\big/_{\omega^2} \tag{3.17}$$

Where the mechanical conductance, $Y(\omega)$, is the real part of the admittance.

The amplitude spectral density of the thermal torque is given by (in torque/rt Hz) is given by [8,25,29]:

$$\tau_{th}(\omega) = \sqrt{{4k_B T k_f}\big/{Q\omega_0}} \tag{3.18}$$

Where the quality factor, $Q = \omega_0 I/\beta$. The amplitude spectral density of the angular deflection (rad $\mathrm{Hz}^{-1/2}$) is:

$$\phi_{th}(\omega) = \left(\frac{\tau_{th}^2/\kappa_f^2}{\left(1 - {\omega^2}\big/{\omega_0^2}\right)^2 + \frac{1}{Q^2}\frac{\omega^2}{\omega_0^2}} \right)^{1/2} \tag{3.19}$$

While ϕ_{th} places a limit on the resolution of the angular deflection that can be made by at a single moment, the minimum angular deflection that the balance can resolve can be improved by increasing the number of observations by extending the observation time (t_{obs}, the time span of data collection.). The resolution is improved by a factor of $t_{obs}^{-1/2}$ [9, 24, 27]. For a signal $\omega_s \ll \omega_0$, we can estimate the minimum angular deflection that can be measured is:

$$\phi_{min} \sim \left(\frac{4k_B T}{Q\omega_0 k_f}\ \frac{1}{t_{obs}}\right)^{1/2} \tag{3.22}$$

In our experiment, the noise contribution due to velocity damping is significantly less than the damping due to internal dissipation.

Chapter 4

The Instrument

ABSTRACT:

This chapter will present the major components of the experimental apparatus used to search for equivalence principle violations. The apparatus consists of a vacuum chamber and vacuum system, the torsion balance and its suspension system, an electronic damping mechanism, an autocollimating optical lever, and sensors to monitor the environment, and thermal insulation. Each component of the instrument will be discussed.

The experiment takes place in a bunker at the Tyson Research Center in Eureka, Missouri. The bunker was built during the Korean War to store and protect munitions from attack. It was built partially into a hillside and with thick concrete walls. There is currently no way to control the temperature within the interior of the bunker. However, the interior is isolated from environmental noise and diurnal temperature fluctuations. Seasonal temperature changes are still experienced, but if the bunker remains largely undisturbed, the temperature swings are muted.

Today, Tyson is an environmental field station located away from major roads and cities. This isolation the location greatly reduces ambient noise from foot and vehicle traffic. The bunker is sealed when the instrument is in operation and the instrument is controlled remotely to minimize the disturbances that the highly sensitive balance in subjected to. Wireless internet connection, an uninterruptable power supply, and a backup generator was installed to ensure that the instrument remains in operation even when power to the bunker is lost.

Two sets of aluminum scaffoldings surround the instrument. The inner scaffolding suspended the instrument above the floor. The outer scaffolding is designed to access the upper half of the instrument comfortably and anchors the large Styrofoam sheets used for thermal insulation.

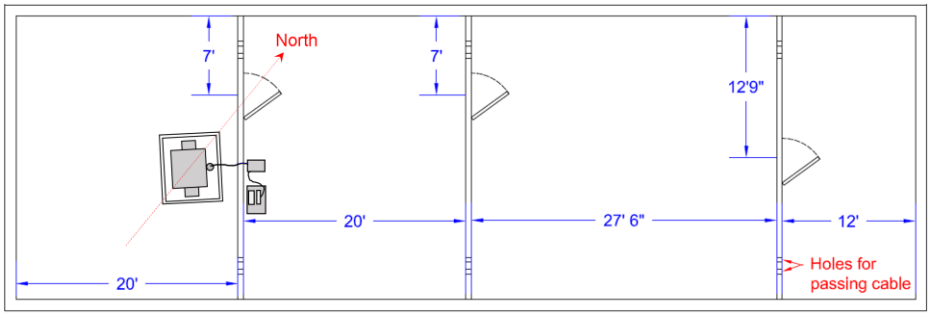

Figure 4.1: Bunker 42 floor plan.

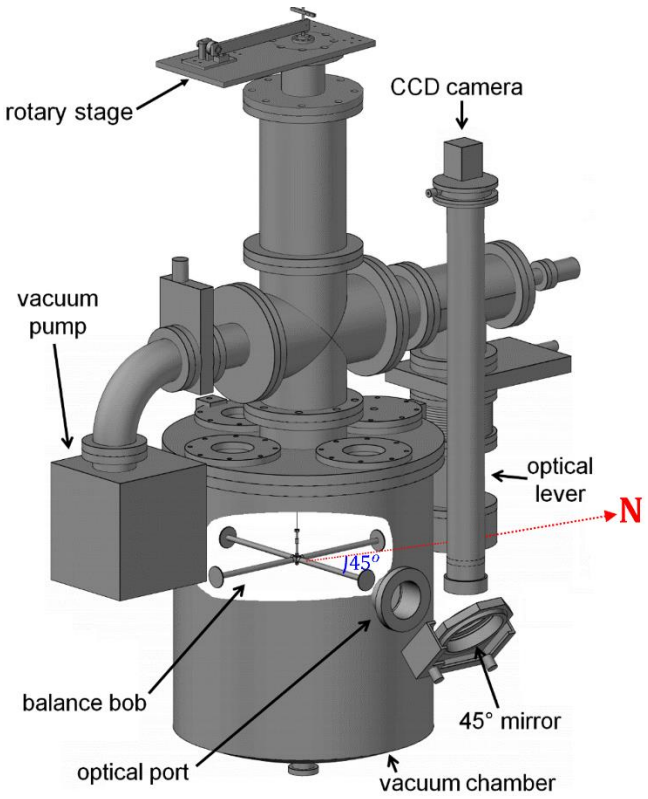

Figure 4.2: CAD drawing of the instrument and its major components. The dashed red line points North, making an approximately 45^{o} angle with the arm of the balance in front of the optical port.

4.1 Vacuum Chamber and Vacuum System

4.1.1 The Vacuum Chamber

The vacuum chamber consists of two parts. The upper part of the chamber is cross-shaped. The fiber is attached to the top of the chamber and down the "neck" of the chamber. The two "arms" of the chamber house two different vacuum pumps used to evacuate the chamber (see Figure 4.1). The upper part of the chamber is mounted on a scaffolding created from T-slotted aluminum frames.

The lower half of the chamber is large bell jar with an optical port, it houses the torsion balance and contains a safety mesh to catch the balance should the fiber break. The two parts of the chamber are separated when suspending the balance. The bell jar is raised and lowered using a wooden platform built for this purpose. Once the balance is secured and oriented in the proper direction, the lower half of the chamber is carefully raised until it meets the upper half. The two parts of the chamber are sealed together using C-clamps, and the platform is lowered.

The vacuum chamber is suspended above the ground, where seismic & vibrational noise and temperature fluctuations cannot directly interact with the chamber. The vacuum chamber has been observed holding a vacuum of $\sim 10^{-9}$ Torr.

4.1.2 The Vacuum System

The vacuum system consists of three pumps. The evacuation of the chamber begins with the operation of a scroll pump (model Edwards XDS). Once a rough vacuum ($\sim 10^{-3}$ Torr) has been established, then a turbomolecular pump is activated (Osaka Vacuum turbomolecular

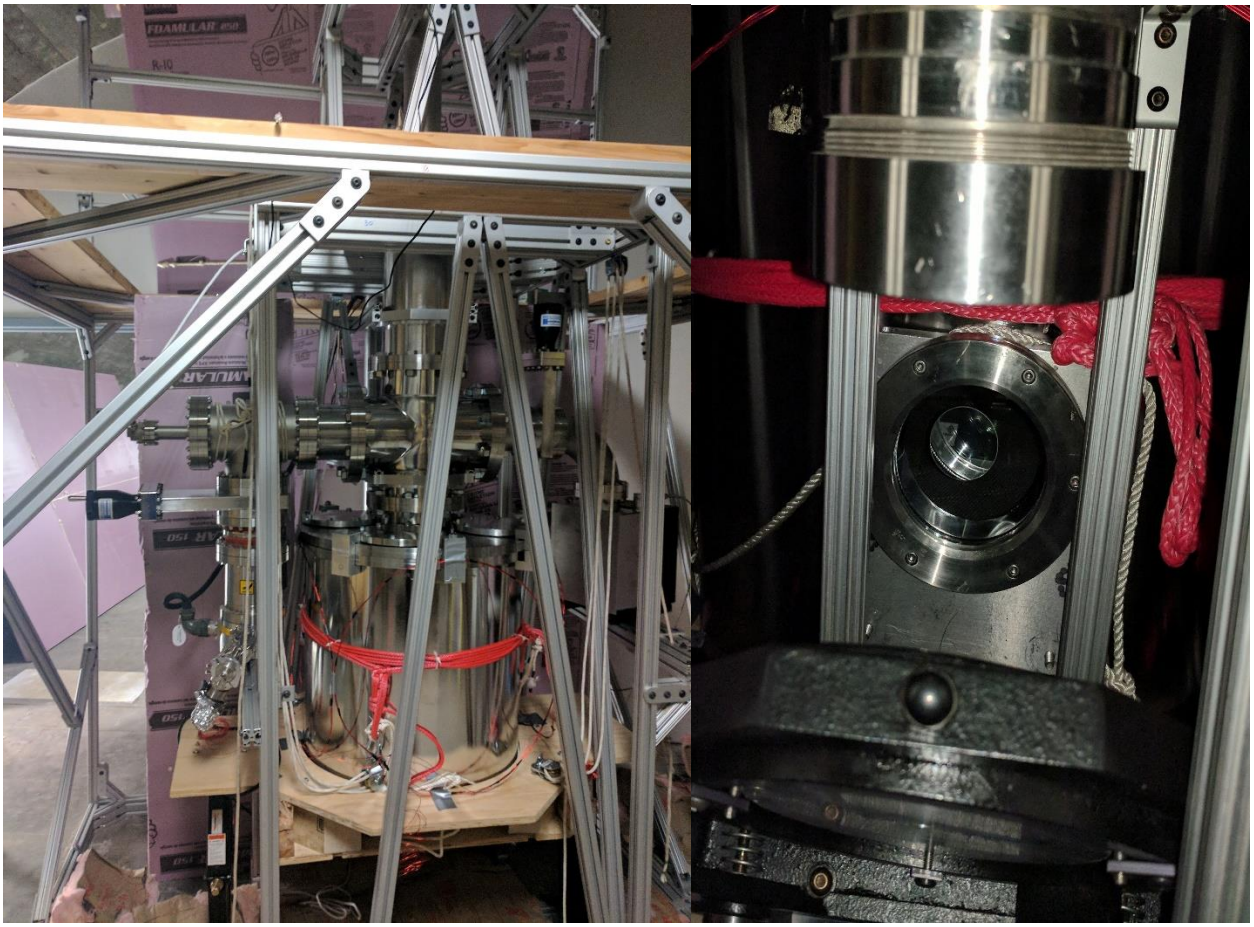

Figure 4.3: The vacuum chamber that houses the balance. The balance seen through the chamber's optical port.

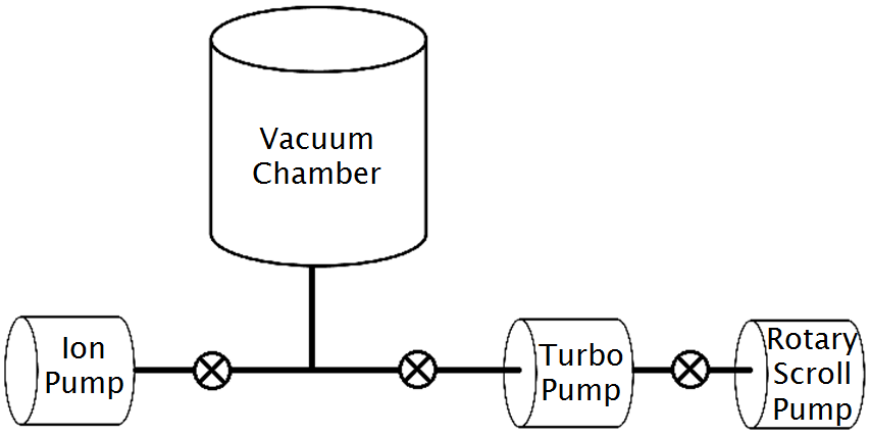

Figure 4.4: The vacuum system. Only the ion pump is in operation during data collection, to maintain the vacuum.

pump). This pump is backed by the scroll pump. When the turbomolecular pump reaches its limit ($\sim 10^{-8}$ Torr), an ion pump is activated (VacIon Starcell Ion Pump) to reduce the pressure and maintained from at around 10^{-9} Torr (started at around $\sim 7 \times 10^{-9}$ Torr and dropped down to $\sim 2 \times 10^{-9}$ Torr over the period of data collection). Once a stable vacuum is achieved, the turbomolecular pump and scroll pump are turned off. The ion pump, which has no moving components that can disturb the balance, maintains the vacuum.

4.2 The Balance and the Fiber

4.2.1 The Torsion Balance

The balance is designed to maximize the amount of "active mass", the mass of the test bodies that respond to and measure EP-violating interactions. The balance has a cross-shaped body with four arms, each attached to a disk-shaped test body.

The arms of cross-shaped balance are made from thin strips of aluminum foil rolled into tubes 24.00 ± 0.05 cm long and a 1.27 cm inner diameter. Each arm is attached to a cross-shaped centerpiece. The fiber is attached to the balance via a threaded rod assembly, which is screwed into place into the center of the centerpiece. The total length of the balance arms from the center to the test body attached to the ends of the arms is 25 cm. It is glued together with Loctite Hysol epoxy, a vacuum compatible epoxy. Holes were punched into each arm to allow trapped gasses to escape during the evacuation of the vacuum chamber.

Several factors aside from theoretical considerations factored into the choice of materials to form the test bodies. As mentioned in Chapter 3, the balance must have a very small mass quadrupole moment to minimize coupling to the horizontal component of gradients in the gravitational field. In order to obtain a high degree of symmetry with this balance design, the test bodies should, as much as possible, have equal mass and a similar size and shape. This restricted the choice of materials to those possessing similar mass densities. In addition, considerations of cost and machinability also factored into the decision.

The test bodies are disks with a diameter of 5.08 cm and a thickness of 0.3175 cm, constructed from aluminum (Al) and quartz glass (SiO_2). Aluminum and quartz glass have similar mass densities, but aluminum is slightly denser. To account for this and ensure equality in the masses, grooves have been cut into the aluminum disks. The aluminum used for construction was Al 1100, an alloy composed of a high percentage of aluminum (~99.6%). The quartz used to manufacture the test bodies have a ~99.995% SiO_2. The outward face of the quartz masses was ground and polished, and mirrored (by coating it with 1000 Å of aluminum).

The total mass of the balance is 75 g, with the four test masses together weighing

Figure 4.5: The Torsion balance.

57.33 g. Nearly 75% of mass of the balance actively couples to EP-violating torques. The moment of inertia of this balance is $\sim 3.8 \times 10^{-3}$ kg m^2.

4.2.2 The Suspension Fiber

The suspension fiber is ~1.6 m long and has a diameter of ~18 μm. The maximum load of this fiber is ~107 g, and the fiber is loaded to around 70% of its limiting strength by the balance. The torsional constant of the fiber (κ_f) is given by:

$$\kappa_f = {}^{\pi\mu r^4}/_{2l} \tag{4.1}$$

Where μ is the shear modulus of tungsten. The torsional constant is $\kappa_f \sim 9 \times 10^{-10}$ N m rad^{-1} and the period of the balance is $T = 2\pi\sqrt{I/\kappa_f} \sim 12{,}700$ s

4.3 Suspension System

The suspension system consists of a "rotary" feedthrough mechanism built in-house, for manual adjustment of the angular orientation of the balance, a picomotor-driven mechanism for minute adjustments of the angular orientation, which can also be used for damping torsional oscillations. A separate mechanism for damping the pendular oscillations of the balance, also built in-house, is attached in tandem and the fiber is attached to the end of this pendular damper.

4.3.1 Rotary Feedthrough Stage

The rotary feedthrough stage is used to make adjustments of the angular orientation of the balance. The adjustments can be made manually or using a picomotor piezo linear actuator. Manual adjustments to angular orientations of the balance are made by turning a nut attached to an adjustment rod that extends through the feedthrough (Figure 4.6, on the right). A picomotor linear actuator (Figure 4.6, on the left) drives the end of a lever arm clamped to the adjustment rod. The picomotor has a range of 1.27 cm or ~ 0.05 rad.

Well timed adjustments of the equilibrium angular orientation of the balance can reduce the amplitude of the torsional oscillations (see figure 4.7). Once the torsional oscillations have been damped down as much as possible manually, the picomotor can be used to further damp the oscillations.

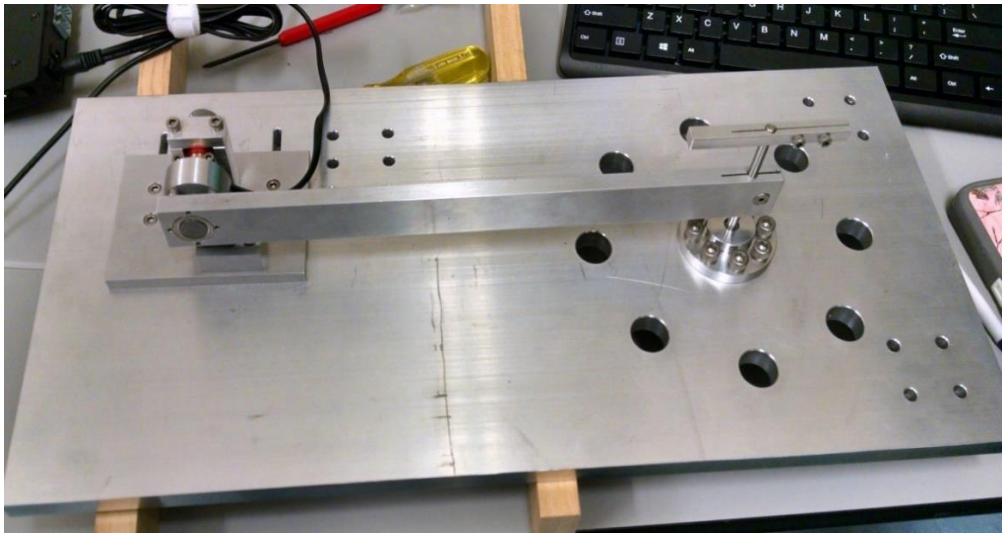

Figure 4.6: The rotary feedthrough stage. Used to adjust of the angular orientation of the balance.

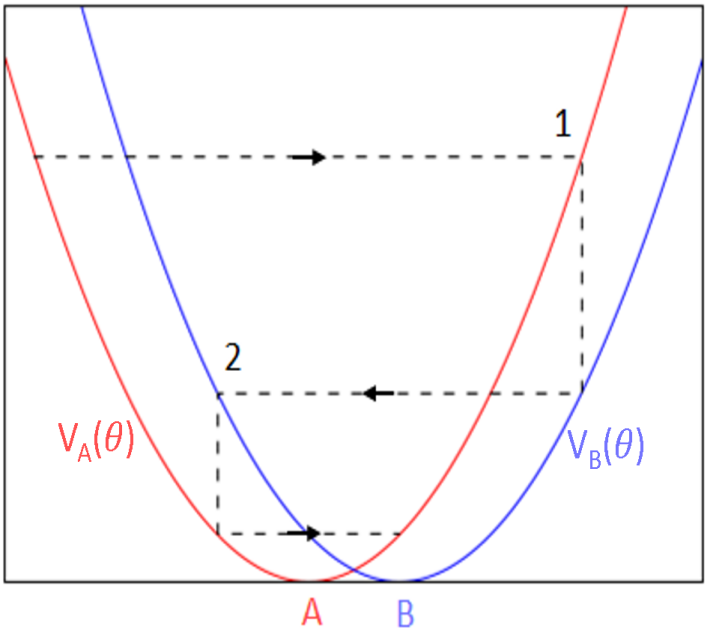

Figure 4.7: Damping the balance by shifting the equilibrium position. When the balance reaches the location marked 1 (on the red curve), the equilibrium position is shifted to position B. When the balance reaches position 2 (on the blue curve), the balance equilibrium position is shifted back to A. By these operations, the amplitude of the oscillations is reduced by twice the shift from A to B and the balance stays as before [6].

4.3.2 Pendular Damper

In addition to the torsional oscillations, the balance has other higher order modes of oscillation as well (for example, pendular swings, wobbles, bounces, and violin modes). These oscillations have frequencies several orders of magnitude higher than the torsional mode but can feed energy into the torsional oscillations through mode coupling. The most prominent and problematic high frequency mode of oscillation are pendular oscillations [47-49].

The eddy current damper consists of two ring magnets, a copper disk, and aluminum clamps that attach the fiber to the copper disk (see Figure 4.8). The copper disk is placed between two ring magnets. The plane of the copper disk is perpendicular to the magnetic field

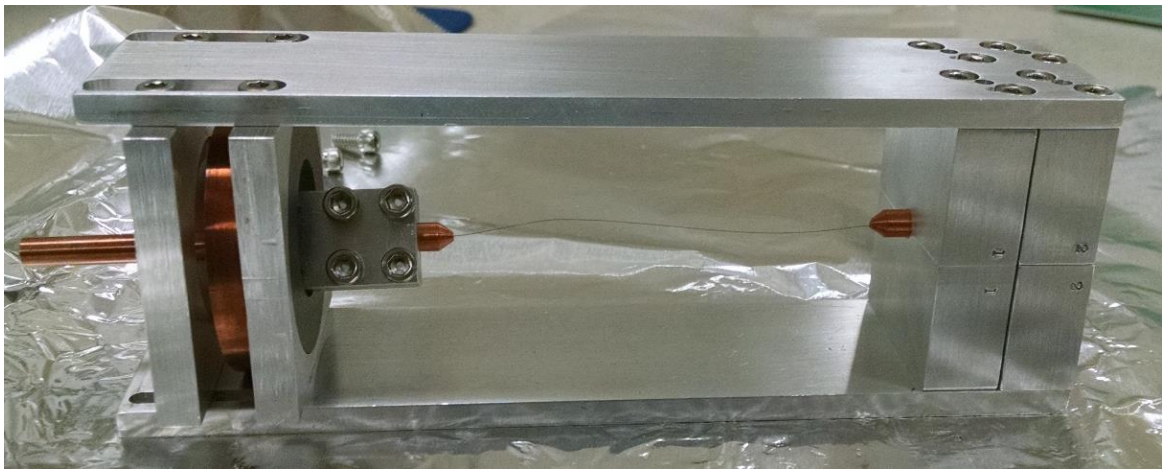

Figure 4.8: The pendular damper.

lines generated by the ring magnets. Pendular oscillations of the balance will cause the copper disk to swing as well, thereby generating eddy currents in the copper disk, which removes energy from the oscillations as they dissipate. The assembly also works to decouple the torsional oscillation from tilts.

4.4 Autocollimating Optical Lever

The autocollimating optical lever (the autocollimator) is a highly precise goniometer used to measure the angular deflection of the balance (see Figure 4.9, 4.10). A LED light source illuminates an array of slits. The light, diffracted by the slits, bounces off a flat mirror (M1) towards the field lens (L). The field lens is an achromatic lens with a focal length of one meter. The virtual image corresponding to M1 is located in the focal plane of the field lens, and the light passing through the field lens from M1 will be collimated. The collimated light is comprised of multiple beams, one for each slit. The light leaves the autocollimator and reflects off a gimbal mirror and directed towards the optical port on the vacuum chamber, through which the balance

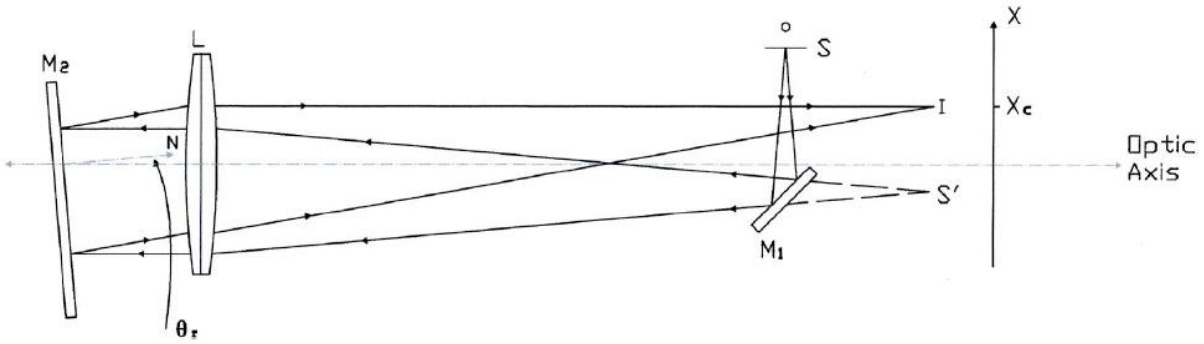

Figure 4.9: A diagram illustrating the working principle behind the autocollimator [6].

can be observed. The light bounces off the mirrored surface of the balance (M2) back onto the gimbal mirror and enters the autocollimator. The field lens focuses the incoming light into an image on its focal plane, where a linescan CCD camera (PerkinElmer linescan CCD) captures this image. The CCD is an array of 2048 pixels (with dimensions $14\mu\text{m} \times 14\mu\text{m}$). The position of the image on the CCD array depends on the angle made by the normal to M2's surface and the optic axis of the autocollimator. The autocollimator tracks the balance deflection by tracking the movement of the image.

An external trigger prompts the CCD to capture an image. The trigger rate used in the image acquisition is $\sim$1 kHz. 500 frames are summed to produce a single image for a sampling rate of 1 image every half second ($\sim$2 Hz). The image data is digitized by a NI 8-bit image acquisition device.

The image captured by the CCD is an array of peaks, the diffraction limited image created by the array of slits. The image is passed through an image processing routine to determine the direction of the normal to M2 (the mirrored surface of the balance) with respect to

the optic axis of the autocollimator (see Chapter 5). A change in the position of the image on the CCD array, Δx, corresponds to a balance deflection of:

$$\Delta\phi = {}^{\Delta x}/_{2f} \tag{4.2}$$

Where f is the focal length of the lens: $f = 100$ cm. A shift in the image position of one pixel, therefore, corresponds to a $\Delta\phi = 7\mu$rad.

4.5 Magnetic Damping System

The torsion balance is a highly sensitive measurement device. It is not possible to isolate the balance from the occasional sharp disturbance from the environment (such as a nearby earthquake), and these disturbances will feed energy into the amplitude of the torsional oscillations. An efficient damping mechanism is required to remove energy from the torsional oscillation inevitably introduced by external disturbances during data collection. To this end, a magnetic damping system was implemented.

This damping system uses two pairs of Helmholtz coils outside the vacuum chamber, placed orthogonally to each other. When the damping system is activated, they generate two orthogonal, uniform magnetic fields with a sinusoidal time-variation (created by sinusoidal currents passing through the coils). The two sinusoidal signals have a phase shift of $\pi/2$ with respect to each other These time-varying magnetic fields will damp the torsional oscillations inducing “eddy current loops” in the moving balance. The induced current and the coil-generated magnetic fields interact to produce a torque on the balance. The direction of the torque depends

upon whether the phase difference between the $\hat{x}$ coils and the $\hat{y}$ coils is positive or negative. When the balance changes direction, the phase of the current in one of the sinusoidal signals may be inverted to produce a torque that will continue to oppose the balance motion.

The sinusoidal currents in the coils are generated by amplifying the signals generated by an oscillator circuit. A voltage-controlled amplifier is used to control the damping strength by controlling the current passing through the coils. Unfortunately, during data collection the damping system encountered an error where it failed to properly change the induced torque. The use of magnetic damping was restricted to damping only the clockwise movements.

4.6 Environmental Sensors and Thermal Insulation

The ambient temperature of the bunker was monitored using six thermistors. Two thermistors monitored the upper half of the apparatus. The lower half of the balance, which encases the torsion balance, was monitored using four thermistors.

The thermistor was placed next to the chamber in the north-eastern, north-western, south-eastern, and south-western directions. The thermistors were arranged to allow for the measurement of temperature gradients in various directions. The data acquisition device collecting data from the upper half of the apparatus encountered failures frequently and therefore this data was not used in the analysis. The thermistors monitoring the lower half of the instrument performed smoothly. In addition to the temperature data, a weather station was used to collect pressure data (in Pascals) and relative humidity (in units of % Relative Humidity). Pressure and humidity data were sampled once every two minutes.

Figure 4.10: The damping coils are mounted on the chamber orthogonal to each other.

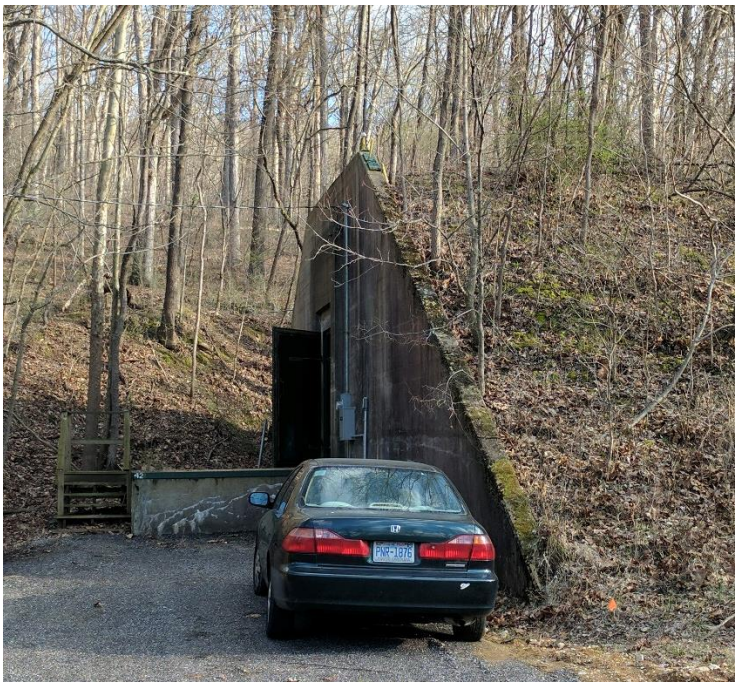

Figure 4.11: The bunker at Tyson Research Center.

Chapter 5

Development of Image Processing and Image Tracking Algorithms

ABSTRACT:

The angular orientation of the torsion balance is measured with a multi-slit autocollimating optical lever. Light from an array of parallel slits is collimated and then reflected off a plane mirror attached to the balance. The reflected light returns through the collimating lines and is imaged as a series of peaks onto a linear array or CCDs. The position of this image on the CCD array determines the angle between the normal of the mirror and the optical axis of the autocollimator. In this chapter we describe the algorithm that is developed to precisely locate the image position on the CCD and track it as the torsion balance executes oscillations.

5.1 Introduction

The design and development of a multi-slit autocollimating optical lever was first published by Cowsik [37]. The autocollimating optical lever (the autocollimator) is used to measure the small angular displacements of the masses on the end of the torsion balance with high accuracy by translating the angular displacement of the balance to a linear displacement of an image along the focal plane of the collimating lens. The image is created by a set of slits illuminated by a light source in the autocollimator. The collimated light, after reflection off a plane mirror on the balance, is imaged onto a linear CCD array. The CCD consists of a 1D array of pixels, 2048 pixels long (see Chapter 4). The slits create a pattern consisting of several approximately Gaussian peaks broadened by diffraction of the light as it passes through the slits (Figure 5.1). The linear displacement of this image as it moves across the CCD is measured with respect to a set of designated fiducial points on the CCD.

The key challenge addressed in this chapter is the development of an algorithm to track a diffraction-limited image whose profile is distributed over hundreds of pixels (Figure 5.1) with resolutions greater than the resolution of a single pixel. The traditional method used to "localize" the image for this instrument is to calculate the image centroid. The calculation of the image position is inherently limited by the Poissonian fluctuations in the photon count, i.e. the photon shot noise, and the centroid is particularly susceptible this noise. The limitations of the centroid method are well known, and other methods of image tracking have been used in the past by different investigators for similar auto-collimating optical levers [38]. The methods developed and described below seek to improve on all previous methods while working within the constraints placed by our instrument.

Since this chapter will describe the development of an image processing method to analyze the multi-peaked image produced by the multi-slit autocollimator design, a brief overview of the advantages of the multi-slit design will provided for context and to introduce the challenges inherent in image tracking.

5.1.1 Multi-Slit vs Single-Slit Image

Following the discussion in Cowsik [37], the key considerations underlying the design of this systems will be demonstrated using the centroiding method of image tracking. Before discussing the multi-slit design, we will consider the traditional single slit design, which produces an image consisting of a single, diffraction-broadened, peak (see Figure 5.2).

Single-Peak Image: To facilitate the discussion, we assume that the photon count distribution of this peak is described by a Gaussian function:

$$n(x) = \frac{N_0}{(2\pi\sigma^2)^{1/2}} e^{-(x-x_m)^2/2\sigma^2} \tag{5.1}$$

N_0 is the total number of photons within the peak, σ is the root mean square width of the image, x_m is the median of the distribution (i.e. the point at which the total number of photons counted before it equals the number of photons counted after). This is a decent approximation of the actual distribution of the image for the purposes of this discussion.

The shape of a distribution is characterized by its moments: $m_i = \int x^i n(x)\mathrm{dx}$. The centroid of the image (labelled byx_c) calculated using zeroth-order (m_0) and first-order (m_1) moments: $x_c = \frac{m_1}{m_0}$. For a Gaussian distribution:

$$x_c = \frac{\int x*n(x)\mathrm{dx}}{\int nIx)\mathrm{dx}} = \frac{N_0 x_m}{N_0} = x_m \tag{5.2}$$

The uncertainty in the photon count a small segment of the image, Δx, in the mean photon count of that segment is: $\Delta n(x) \sim [\Delta x * n(x)]^{1/2}$. The uncertainty due to photon shot noise along any point of the image is independent of the noise at any other point, the total uncertainty in the estimation of the 1st moment is therefore obtained by summing in quadrature. These uncertainties are introduced in the calculation of m_1:

$$\Delta m_1(x)^2 = \int \left[x\left(x * n(x)\right)^{1/2}\right]^2 \mathrm{dx} = \int x^2 n(x)\mathrm{dx} = m_2 = N_0(\sigma^2 + x_m^2) \tag{5.3}$$

The expression for the uncertainty in the centroid is given by:

$$x_c \pm \Delta x_c = x_c \pm \sqrt{\frac{(\sigma^2 + x_m^2)}{N_0}} \tag{5.4}$$

The position along the CCD array is measured from a fiducial point on the array. While Eq. 5.4 suggests that the uncertainty can be reduced by choosing a fiducial as close as possible to the image median, we have no a priori knowledge of the actual location of the median and the centroid of the image. Without this information, x_m cannot reasonably be smaller than σ. Therefore, the best possible resolution in the centroid is: $\Delta x_c \approx \sqrt{2\sigma^2/N_0}$.

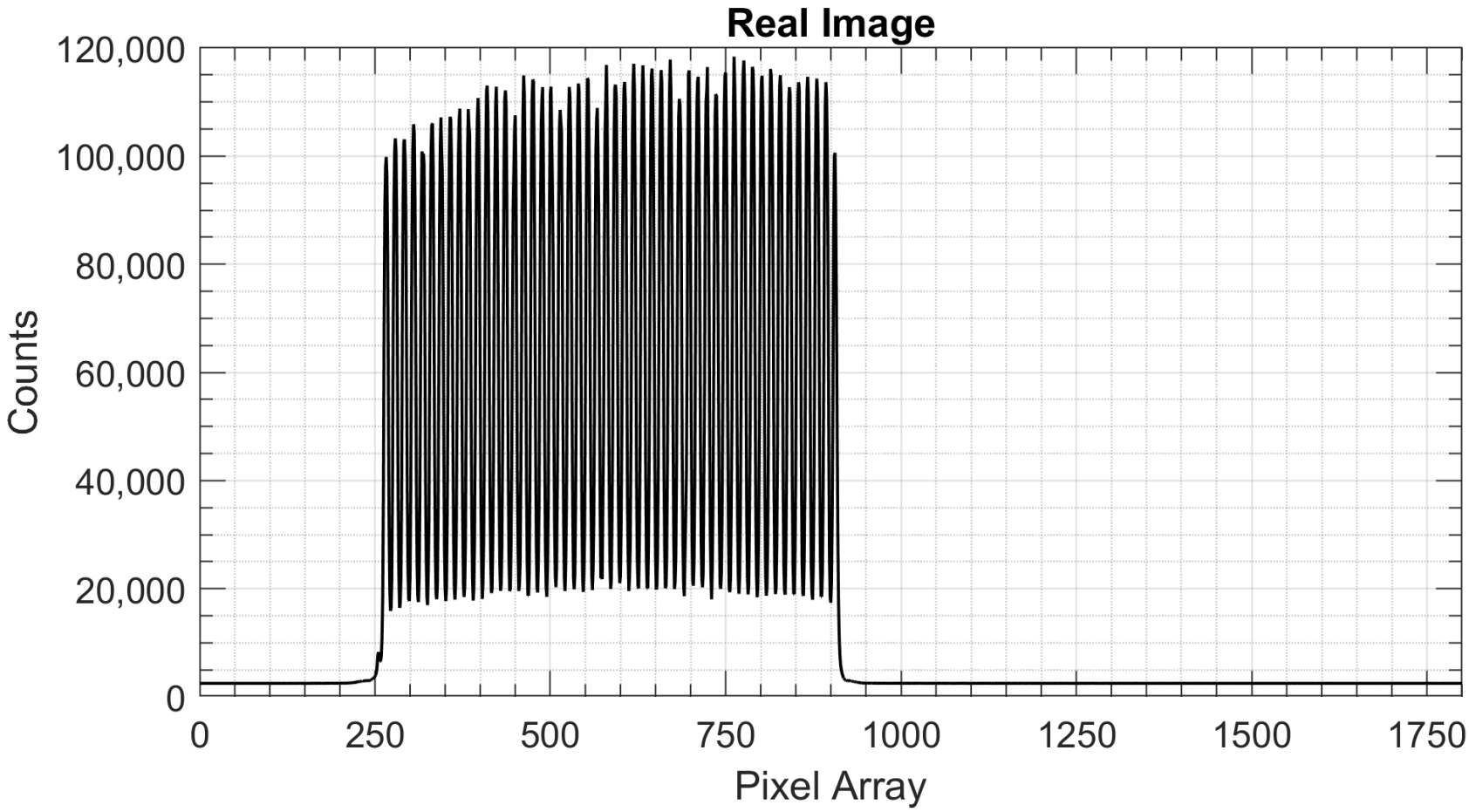

Figure 5.1: A plot of a real image captured by the CCD.

Multi-Slit Image: We will now consider an image consisting of multiple peaks generated by an array of identical slits separated by a distance, labelled "a". We first investigate the case where all positions are measured from a single fiducial point (as before). The position of the whole image is defined as:

$$x_c = {\sum m_{1,i}}\Big/{\sum m_{0,i}} \tag{5.4}$$

Where i denotes the peak. The number of slits is denoted by *k*, and $i = 1, \dots, k$.

We will again assume that the image produced by an individual slit has a perfectly Gaussian photon count distribution. The median of the image produced by the i^{th} slit, given our assumptions, is given by: $x_{m,i} = x_m + a(i-1)$, where x_m is the median of the peak closest to the fiducial. The uncertainty in the centroid of each peak is: $\Delta x_{c,i} = \left[N_{0,i}\left(\sigma^2 + x_{m,i}^2\right)\right]^{\frac{1}{2}}/N_{0,i}$. The average uncertainty in the whole image is sum, in quadrature, of the uncertainty in each peak

$$\langle (\Delta x_c)^2 \rangle^{1/2} = \frac{1}{k^{1/2}} \left(\sum_i \frac{\left(\sigma^2 + x_{m,i}^2\right)}{N_{0,i}} \right)^{1/2} \tag{5.5}$$

We will assume $N_{0,i} = N_0$ to simplify the calculations and better illustrate the concept. The expression for $x_{m,i}$ is plugged into Eq. 5.5. For a large number of slits (large *k*) the numerator can be expanded and simplified to give an approximate expression for the uncertainty in the position of the whole image:

$$\langle (\Delta x_c)^2 \rangle^{1/2} \sim \frac{k^{1/2} a}{N_0^{1/2}} \tag{5.6}$$

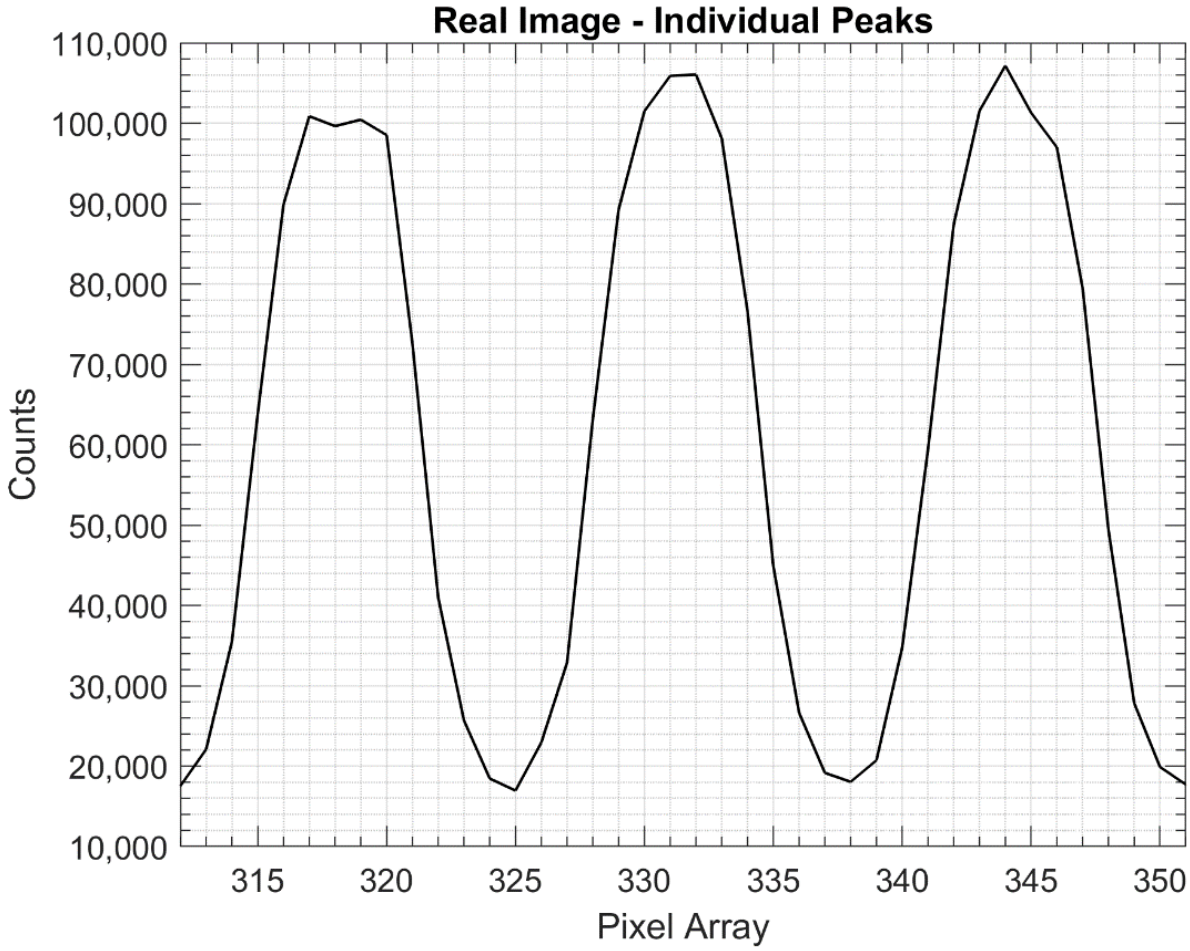

Figure 5.2: Plot of the individual peaks in a real image.

The uncertainty increases with the number of slits and use of multiple slits seems to degrade the resolution.

Instead of measuring the centroid of each peak from a single fiducial point, we now consider the case where each slit has its own fiducial point from which the centroid of the corresponding image peak is measured. The set of fiducial points are designated by $\{y_i\}$. Adjacent fiducial points, which correspond to adjacent slits, are separated by the same length separating the slits, i.e. the separation of adjacent slits is given by: $y_i - y_{i-1} \cong a$, and this implies that for each peak i: $x_{mi} \cong x_0$, where x_{mi} is the median location of the i^{th}peak. The resolution of the centroid is:

$$\langle(\Delta x_c)^2\rangle^{1/2} \approx \frac{1}{k^{1/2}} \left(\frac{k(\sigma^2+x_0^2)}{kN_0}\right)^{\frac{1}{2}} = \frac{(\sigma^2+x_0^2)^{1/2}}{k^{1/2}N_0^{1/2}} \tag{5.7}$$

The resolution of the whole image is now reduced by a factor of $k^{-1/2}$.

While this discussion has used the centroid method to illustrate the advantages in the implementation of the multi-slit design, as long as the position of each image peak is measured from its own fiducial point and the image position is determined by averaging the positions of the individual peaks, the improvements in resolution will be realized.

5.1.2 The Median Method

The median methods are a set of image tracking algorithms that define the image position as the location of the median of the image; The algorithms discussed below implement the calculation of the image median from the photon count distribution using different methods.

It will be shown how the median is more stable than the centroid method in the presence of the photon shot noise.

The median of the image, in comparison, is defined as the location, x_m, at which the following equality is satisfied:

$$\int_{x_0}^{x_m} n(x)\mathrm{dx} = \int_{x_m}^{x_f} n(x)\mathrm{dx} \tag{5.8}$$

Where $x \in \{x_0, x_f\}$.

In other words, the median of an image is the point at which the sum of all detected photons in the image prior to this point is equal to the sum of all detected photons in the image after this point. If the total number of photons in the image is labelled N_T, then the image median, x_m, can be expressed as:

$$\int_{x_0}^{x_m} n(x)\mathrm{dx} = \int_{x_m}^{x_f} n(x)\mathrm{dx} = \frac{N_T}{2} \tag{5.9}$$

In the case of a Gaussian distribution, the uncertainty in the median is:

$$\langle \Delta x_m \rangle = \frac{N_T^{1/2}}{2 \times G(x = x_m)} \approx \frac{1.5\sigma}{N_T^{1/2}} \tag{5.10}$$

With *k* slits, the expression in Equation 5.10 is divided by a factor of $k^{-1/2}$. When compared to Equation 5.7, it can be observed that defining the image position as the median of the image will theoretically allow for higher resolution measurements.

This chapter will first detail the image preprocessing steps taken to improve the remove the noisy background features in the image. Then, the different methods of image

localization are discussed and the results of tests of their performance are presented. Finally, we discuss the image processing algorithm eventually chosen to be implemented for data collection.

In discussing the image tracking algorithms and the image movement across the CCD we will use measure distances and displacements in pixels.

5.1 Image Pre-processing

Once an image is obtained, the first step in preparing the image for analysis is to remove as much of the background noise as possible. This step of the analysis begins by applying a threshold, all pixels with amplitudes below this threshold are set to zero. Then, the location of the valleys of the image peaks and their amplitudes are determined using a peak-finding routine. The width of each peak is defined as the difference between the valley locations within which the peak is contained. The peak widths are calculated and recorded.

The valley locations and amplitudes are used as the input to a second-order polynomial fit. The polynomial obtained from this procedure is calculated for the entire pixel array (Figure 5.3a). The resultant curve is then subtracted from the image data and all amplitudes less zero is set to zero (Figure 5.3b). This procedure removes the noisy background, leaving only well-defined peaks.

The final step is to use this image data to calculate a “Cumulative Counts” curve, which will be defined when the image tracking algorithm is discussed below.

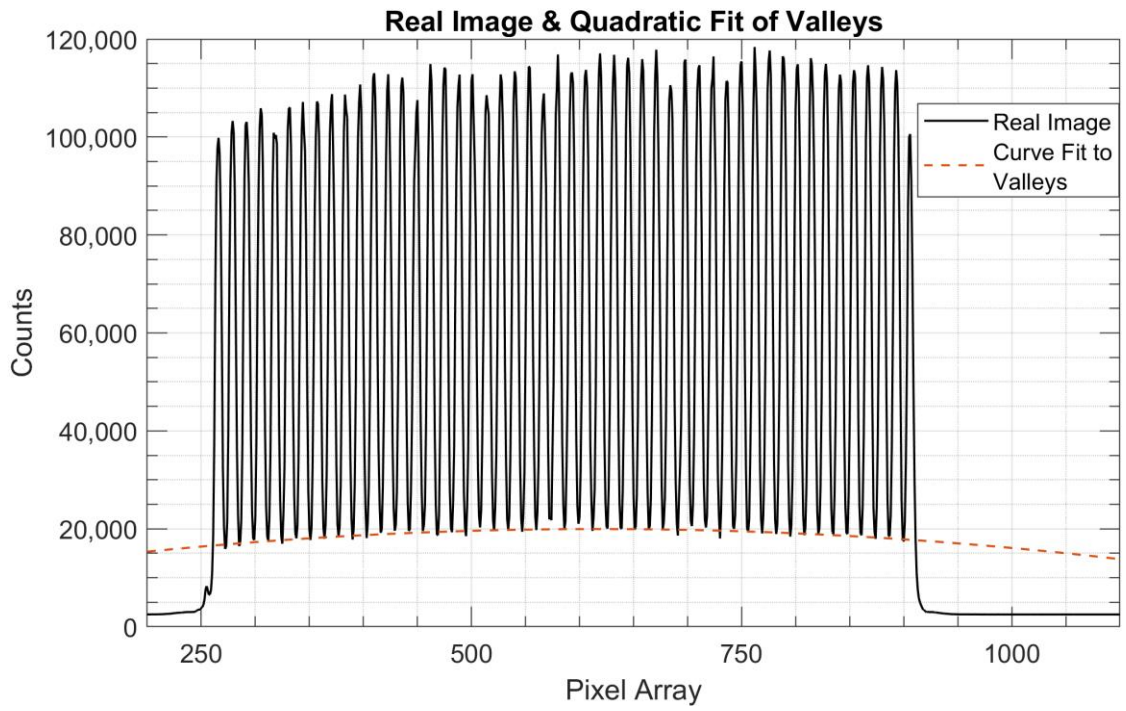

Figure 5.3a: Plot of the quadratic fit curve of the image valleys superimposed on the image.

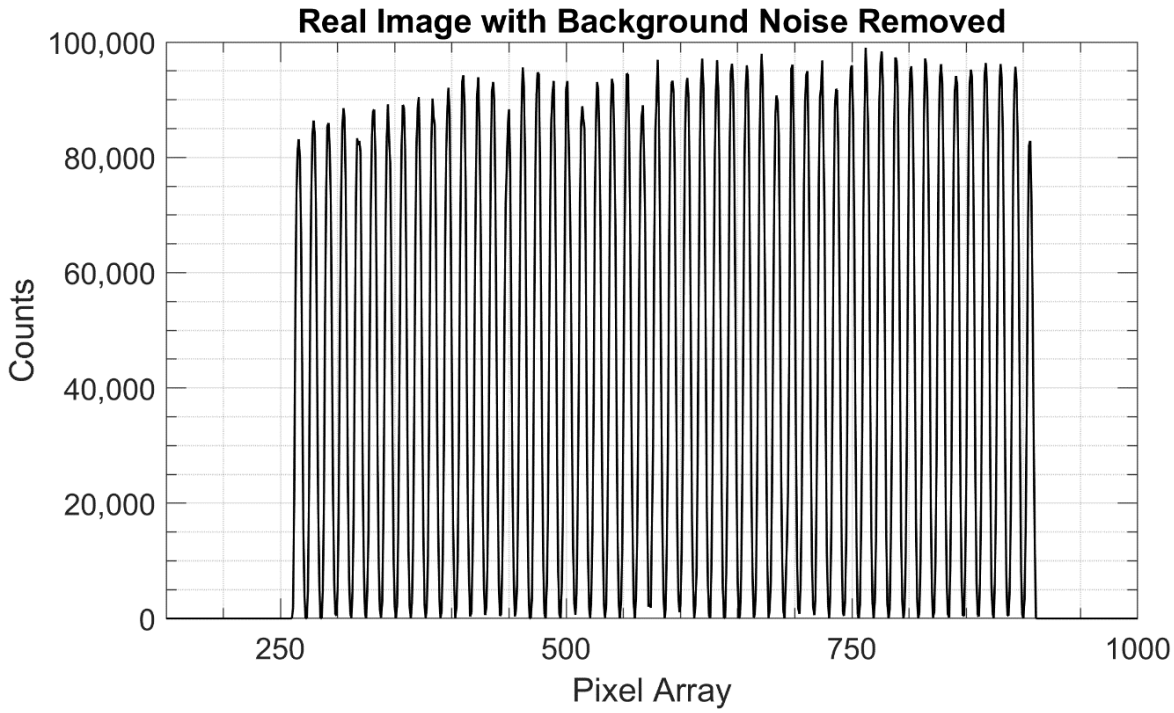

Figure 5.3b: Plot of the quadratic fit curve of the image valleys superimposed on the image.

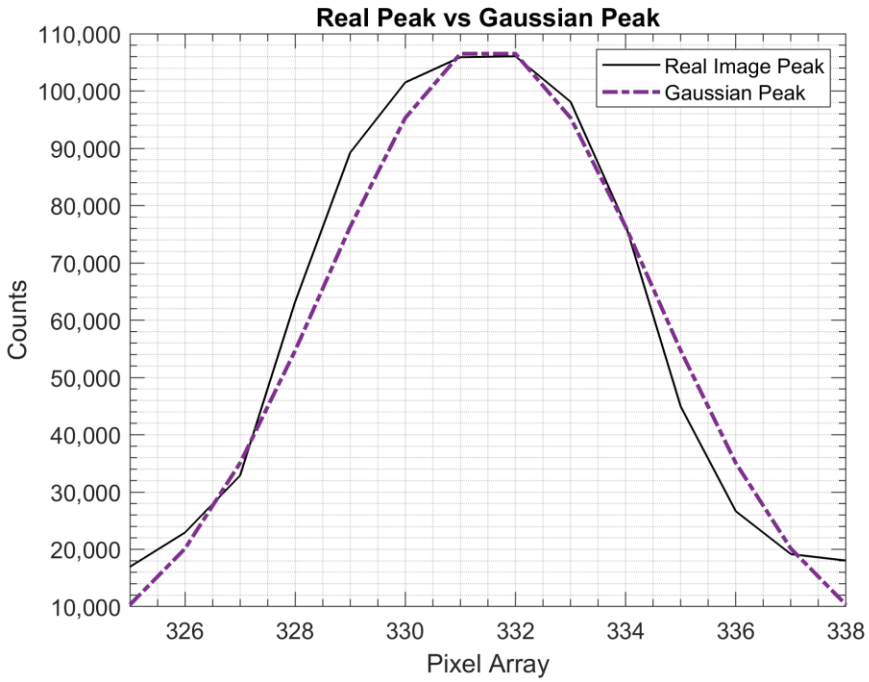

Figure 5.4: Plot of the count distribution peak from a real image vs a Gaussian distribution model of a peak. The non-Gaussian features of real images cannot always be removed, and may be problematic

5.3 Development of the Image Tracking Algorithm

In illustrating the analysis of images produces by the single and multi-slit designs, we made the assumption that the image peaks produced by the slits had a Gaussian photon count distribution and defined the position of the slit as its centroid. However, the discrete photon count distributions in real image data have many non-Gaussian features that cannot be removed in the preprocessing phase of the analysis (see Figure 5.4). The image data provides information on the number of photons counted within a pixel and offers no information regarding the subpixel spatial distribution of photons arriving on the CCD. The lack of knowledge of the real distribution becomes problematic when attempting to define the position of an image to sub-pixel accuracies. In non-symmetric peaks the centroid of the peak does not coincide with the median, and asymmetries in the peak can cause large fluctuations in the centroid location. This is especially deleterious if low-intensity pixels, which have lower signal to noise ratios (SNRs), are the source of the asymmetries in the peak; in the centroiding method, the noisy low-intensity pixels are weighted at least the same as pixels with higher photon counts (and therefore higher SNRs). Gains in the resolution can be made by developing a carefully designed image localization algorithm designed to compensate for these drawbacks.

Arp *et. Al.* [38] approached this problem by developing a peak finding routine that to calculate image position. Their method begins by applying a Gaussian fit to the peak and then taking the logarithm of the peak image data to reduces the influence of the low-intensity pixels. Then, they apply a quadratic fit using weighted ordinary least squares, where the weights are obtained from the initial Gaussian fit. The position of the image is defined as the location of the local maxima calculated from the quadratic fit. While a similar approach is described and investigated in this section, our instrument is not well suited for this approach. Their

autocollimator optics produces a stationary reference image of the slits as well as the image used in measurement. This reference image serves as ideal fiducial points for the measurement of image position. The local maximum of an image is normally subject to undesirable fluctuations, but this setup suppresses the influences of these fluctuations. The autocollimator used in our instrument utilizes fixed fiducials, the resolution of the position of the whole image is limited by the stability of the image position measured for individual peaks. In order to improve the angular resolution of the autocollimator, a robust image tracking algorithm is required.

5.3.1 The FFT-Phase Method

The FFT-Phase method calculates the change in the position of the image by taking advantage of the features of the image in the spatial frequency domain. The image peaks generated by the multiple slits creates a spatial pattern. In the whole image can be thought of as an individual peak that repeats itself at regular intervals. In simulated images, this interval was chosen to be 13 pixels. This is the average interval found between peaks in real images. The FFT amplitude plot of this image will have a large peak at the spatial frequency $f_* \cong \frac{1}{13 \text{ pixels}}$. For real images, the peaks will not in general repeat at precisely at regular intervals, nonetheless there will be a prominent peak in the spectral amplitude and f_* is defined as frequency corresponding to this peak.

The phase shift due to the displacement of an image as a function of the spatial frequency for the image is given by:

$$\phi = \left({}^{2\pi f_*}/_{NT}\right) \times x_c \tag{5.8}$$

Where N is the number of pixels, and T is the conversion factor translating displacements in pixel units to angular displacement (in radians)? The image displacement is then (in pixel units):

$$x_c = {\phi NT}/{2\pi f_*} \tag{5.9}$$

5.3.2 The Median Methods

The advantage of the median method over the centroid was described in the introduction. Real image data is not described by a continuous function, the median must be calculated using the discrete distribution curve to sub-pixel accuracies. Several different methods of implementing this calculation were investigated and their performance was tested against simulated data for robustness. The different methods for calculating the median are all implemented utilizing a new photon count distribution function, which is calculated from the image data. This distribution is called the called the "cumulative counts" distribution or the cumulative counts curve (or cumulative sum array), $C(x)$. (See Figure 5.4)

The cumulative counts distribution at the pixel number i is defined as:

$$C(x_i) = \sum_{j=1}^{i} n\,(x_j)\Delta x \tag{5.13}$$

Where the photon count is a function of the pixel location, labelled by x_i, is labelled $n(x_i)$. Δx in pixel units is simply 1. This function maps the location of a pixel (labelled by i) (x_i) to the cumulative sum of the photons counted by all the pixels before, and including, i.

Considerations in labelling locations to pixels:

The cumulative counts array is the discretized version of the (true) continuous, cumulative distribution function of the photon counts of an image peak. To accurately represent the (true) cumulative distribution function, we must map the elements of the cumulative counts array to locations on the pixel array as accurately as possible.

However, the only information that known with certainty is the total number of photons that were detected within a pixel and nothing can be said of the true spatial distribution of photon arrival within a pixel. The only statement that can be made with certainty is that the result of a spatial integration of the (true) distribution (from one edge of the pixel to the other) must equal the total number of photons detected by the pixel. The only location over the pixel array where knowledge of the photon distribution is known accurately is at the edge of a pixel. The true cumulative distribution of photons will be more accurately reproduced if the elements of the cumulative count array are assigned locations on the edge of their corresponding pixels (see Fig. 5.6).

The cumulative counts curve at the median of the image must be equal to $\frac{N_T}{2}$:

$$C(x_m) = {}^{N_T}/_{2} \tag{5.14}$$

All median finding algorithms start with finding the pixels associated with a cumulative photon count closest to $N_T/2$: pixels (x_i & x_{i+1}) where $C(x_i) \leq \frac{N_T}{2} < C(x_{i+1})$.The goal of the median finding methods is to estimate the subpixel location where the distribution function describing the cumulative sum of photons over an image peak has the value $N_T/2$. This

estimation is made entirely using the number of photons detected by the pixel and the cumulative sum array constructed from this data. A median finding method must use this information to estimate, as accurately as possible, the location of the median with subpixel resolution. Some of the different methods that were developed and investigated will be described. An appealing feature of these methods (with one exception) is that no a priori assumptions of the form of the photon count distribution are needed, these methods are effective for any distribution that is roughly peak shaped.

Taylor Expansion Method:

If the median (labelled by x_m) is located within pixel x_0, and we take x_0 to label the edge of the pixel, then the distance (dp) between x_0 and x_m can be found by using the Taylor expansion of the cumulative photon count function, C(x) (see Figure 5.7).

The Taylor expansion is:

$$C(x_m) = C(x_i + dp) = C(x_i) + \left.\frac{dC}{dx}\right|_{x_i} (dp) + \frac{1}{2!}\left.\frac{d^2C}{dx^2}\right|_{x_i} (dp)^2$$

$$= {}^{N_T}/_{2} \tag{5.15}$$

We use discrete differentiation to find the derivatives at x_i:

$$\left.\frac{dC}{dx}\right|_{x_i} = \frac{C(x_{i+1}) - C(x_{i-1})}{2}$$

$$\frac{1}{2!}\left.\frac{d^2C}{dx^2}\right|_{x_i} = \frac{C(x_{i+1}) - 2C(x_i) + C(x_{i-1})}{2}$$

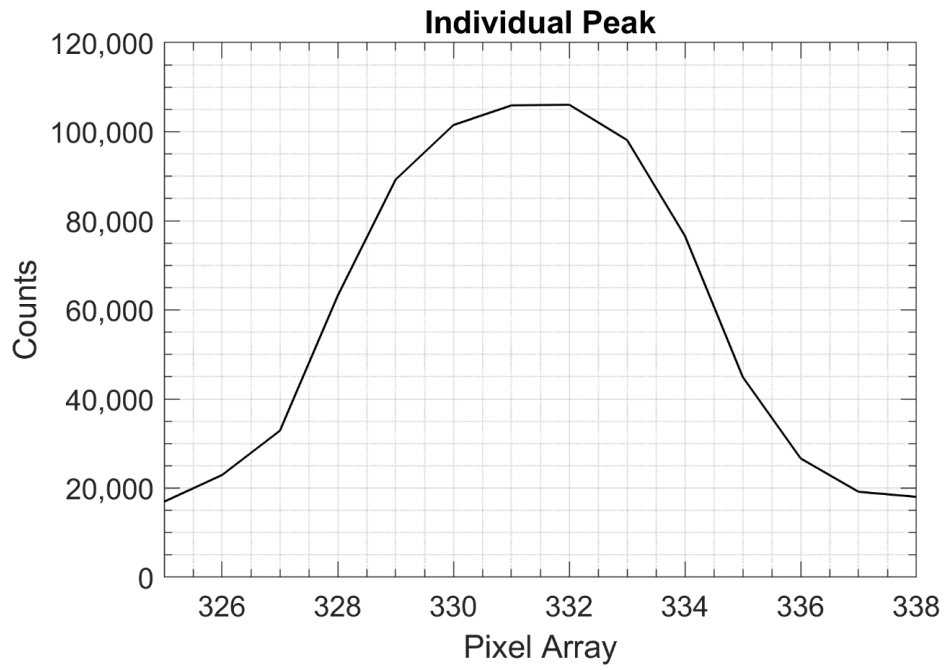

(a)

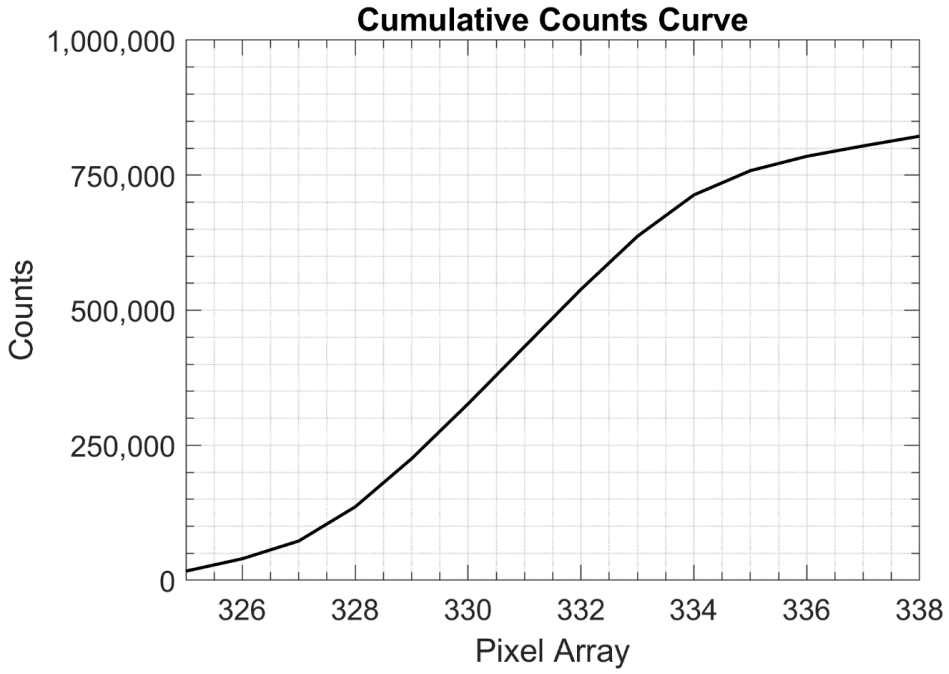

(b)

Figure 5.4: (a) Photon count distribution of an individual peak and (b) The corresponding cumulative photon count distribution

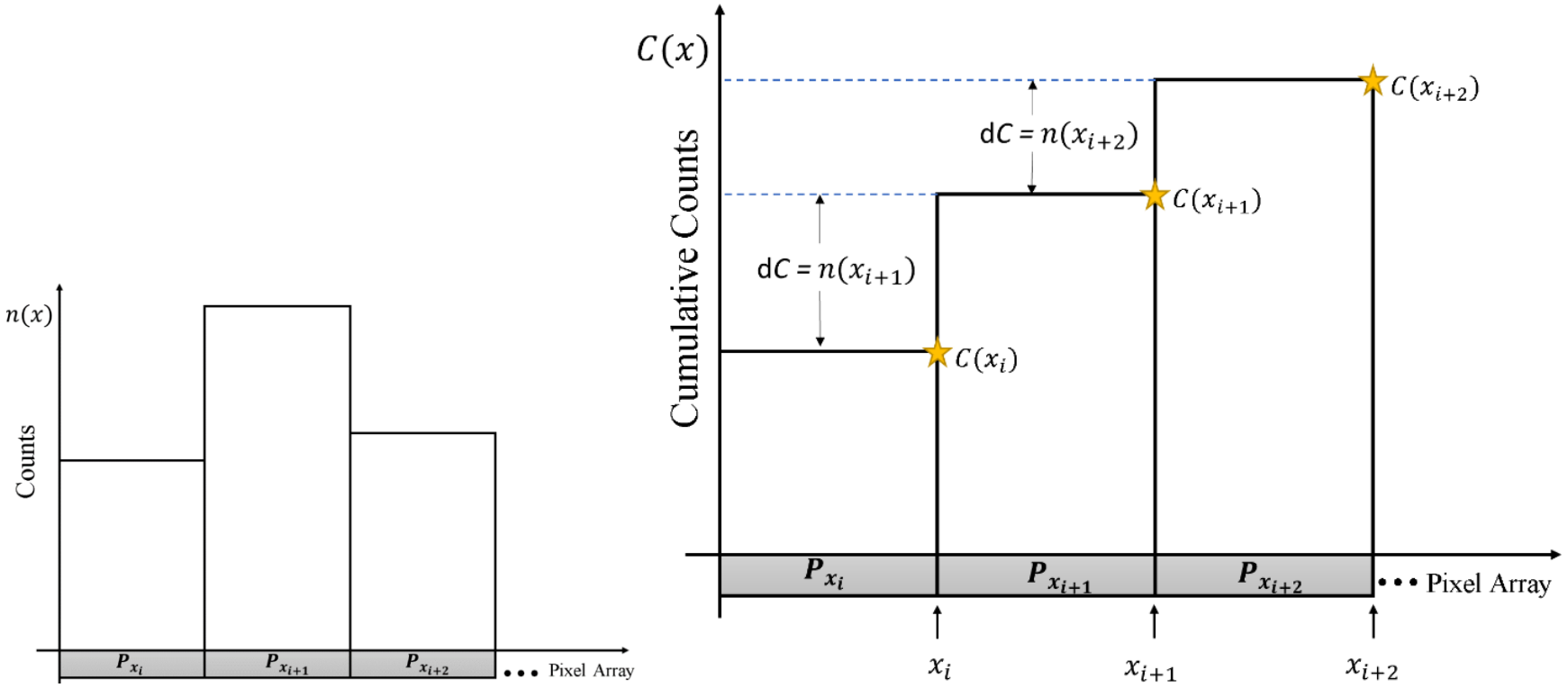

(a) **(b)**

Figure 5.6: (a) An illustration of the photon count distribution. The actual distribution within the pixel is not known, only the photon counts within the pixel. (b) An illustration of the corresponding cumulative counts curve. The only location within a pixel where the cumulative count distribution is known with certainty is at the edge of the pixel, and so the location of a pixel will be assigned to this point.

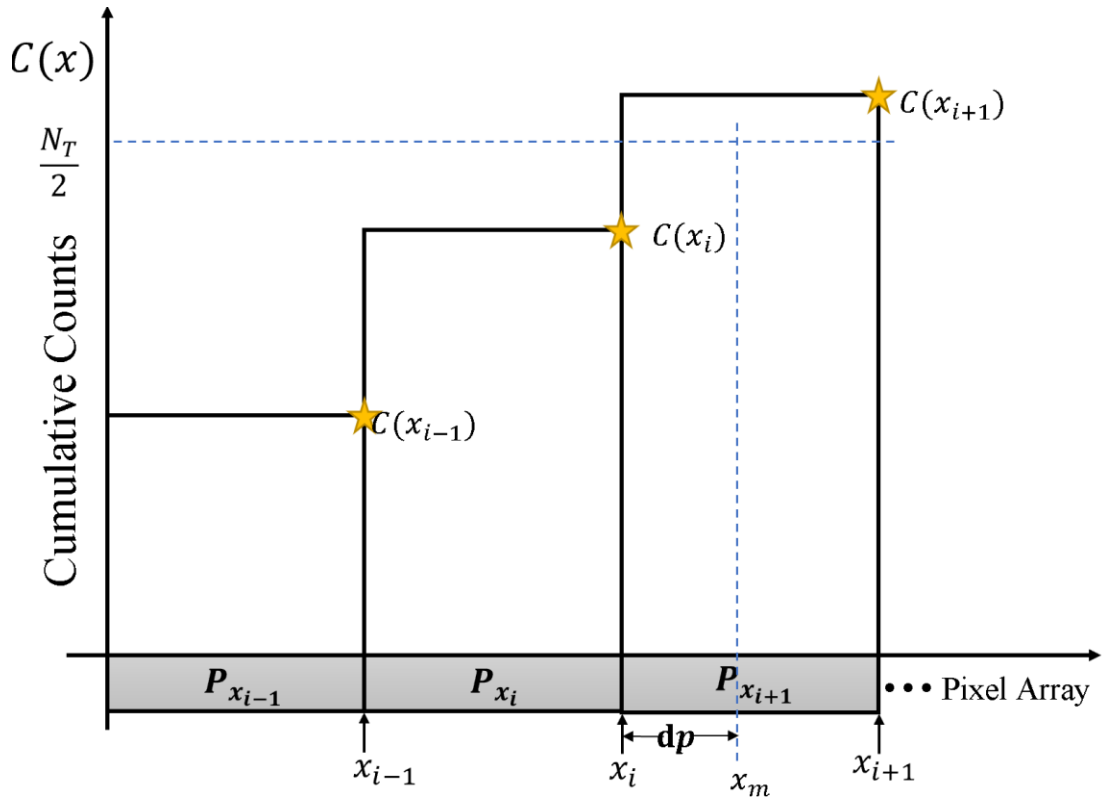

Figure 5.7: A visual illustration of the application of the Taylor Expansion method.

Then we solve for resulting polynomial for dp to estimate the location of the median.

This procedure to calculate the median was repeated for every peak in the image, and the median of the whole image was found by averaging the medians of the individual peaks (the averaging helps reduce the influence of fluctuations).

Two-Point Interpolation Method:

The location of the median can also be found by interpolation using the two points adjacent to the median. See Figure 5.8

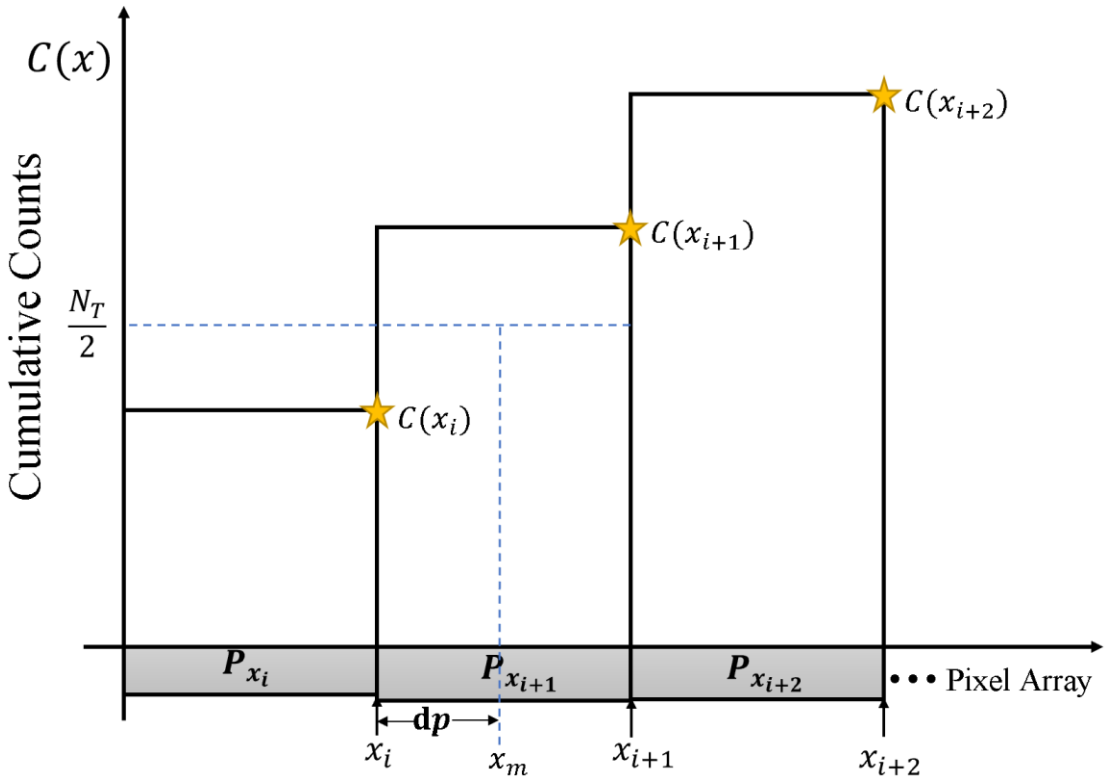

Figure 5.8: A visual illustration of the application of the Two-Point Interpolation method

The equation for the distance between x_i and x_m is:

$$dp = \frac{C(x_m) - C(x_i)}{C(x_{i+1}) - C(x_i)} = \frac{N_T/2 - C(x_i)}{C(x_{i+1}) - C(x_i)} \tag{5.16}$$

This method was implemented in the same way as the Taylor expansion method. The median of each peak was calculated, and the median of the whole image is found by averaging the medians of each peak.

Fourth Order Polynomial Fit:

This method estimates the median of a peak by fitting the cumulative sum curve to a fourth order polynomial. This polynomial is written as:

$$C(x) = K_0 + \sum_{i=1}^{4} K_i x^i \tag{5.17}$$

The fitting procedure begins, like the previous methods, with first identifying the point closest to the median (labelled x_0, and the corresponding element in the cumulative sum array as $C(x_0) = C_0$).

The point x_0 will be chosen as the reference point, and the polynomial can be rewritten as:

$$C(z) = K_0 + \sum_{i=1}^{4} K_i z^i \tag{5.18}$$

Where $z = x_j - x_0$.

The two adjacent points to the left of the median (labelled z_{-1} and z_{-2}t and the corresponding element in the cumulative sum array C_{-1} and C_{-2}) and the two points to the right (labelled z_1 and z_2, and the corresponding element in the cumulative sum array C_1 and C_2) are used to generate a fourth order polynomial that estimates the cumulative sum curve near the median. The resulting system of equations is:

$$C_0 = K_0 \tag{5.19a}$$

$$C_1 = K_0 + K_1 + K_2 + K_3 + K_4 \tag{5.19b}$$

$$C_{-1} = K_0 - K_1 + K_2 - K_3 + K_4 \tag{5.19c}$$

$$C_2 = K_0 + 2K_1 + 4K_2 + 8K_3 + 16K_4 \tag{5.19d}$$

$$C_{-2} = K_0 - 2K_1 + 4K_2 - 8K_3 + 16K_4 \tag{5.19e}$$

The K coefficients must be determined. They can be determined by solving the following system of equations:

$$K_1 = \frac{2}{3}(C_1 - C_{-1}) + \frac{1}{12}(C_{-2} - C_2) \tag{5.20a}$$

$$K_2 = \frac{2}{3}(C_1 + C_{-1}) - \frac{1}{24}(C_{-2} + C_2) - \frac{5}{4}C_0 \tag{5.20b}$$

$$K_3 = \frac{1}{6}(C_{-1} - C_1) + \frac{1}{12}(C_2 - C_{-2}) \tag{5.20c}$$

$$K_4 = \frac{C_0}{4} - \frac{1}{6}(C_1 + C_{-1}) + \frac{1}{24}(C_2 + C_{-2}) \tag{5.20d}$$

These equations can be simplified if the reference point is shifted to coincide with C_0. Then $C_0 = C(x_0) = 0$ & $C_1 = C(x_1) - C(x_0)$ & $C_{-1} = C(x_{-1}) - C(x_0)$ ...

Solving for the coefficients:

$$K_1 = [8(C_1 - C_{-1}) + (C_{-2} - C_2)]/12 \tag{5.21a}$$

$$K_2 = [16(C_1 + C_{-1}) - (C_{-2} + C_2)]/24 \tag{5.21b}$$

$$K_3 = -[2(C_1 - C_{-1}) - (C_2 - C_{-2})]/12 \tag{5.21c}$$

$$K_4 = -[4(C_1 + C_{-1}) - (C_2 + C_{-2})]/24 \tag{5.21d}$$

Solving for the coefficients will allow the location of the median to be estimated by solving:

$$C(x_m) = C(x_0 + \delta p) = \frac{N_T}{2} = \sum_{\alpha=1}^{4} K_\alpha (\delta p)^\alpha \tag{5.22}$$

Gaussian Parameters Method:

This approach begins similarly to the approached described in [38]. A Gaussian fit is used to estimate the location of the peak maxima. The peak is described by a quadratic function whose coefficients are obtained from the Gaussian fit. Unlike the approach described by Arp [38], this quadratic is integrated, and the resulting equation is solved for the median.

The pixels that compose the peak will be described by the following function:

$$\mathrm{dC} = f(x) = a + b\left(x - x_p\right)^2 \tag{5.23}$$

Where x_p is the location of the peak. The parameters $a, b, \& \, x_p$ are obtained by fitting the whole peak to a Gaussian function:

$$f(x) = a\, exp\left(-\left(x - x_p\right)^2 \Big/ 2\sigma^2\right) \tag{5.24}$$

This fitting method starts with a best guess for the amplitude (a), center (x_p), and standard deviation (σ), and calculates the residue between the peak data and the fit. If residue is greater than a set tolerance, then the fitting procedure is repeated to obtain more accurate parameters. The residue is once again calculated, and this process is repeated until the residue is below the tolerance. Then then output will be the parameters a, x_p, and σ.

These parameters are used to find the expression for dC. We can observe this by expanding the Gaussian fit to the second order using a Taylor expansion evaluated at the point $x = x_p$: $f(x) \cong f\left(x_p\right) + f'\left(x_p\right)\left(x - x_p\right) + f''\left(x_p\right)\left(x - x_p\right)^2 + \cdots$:

$$f(x) \cong a \times exp\left(-\left(x_p - x_p\right)^2 \Big/ 2\sigma^2\right) + a\left[\left(-\frac{x_p - x_p}{\sigma^2}\right) \times exp\left(-\left(x_p - x_p\right)^2 \Big/ 2\sigma^2\right)\right] \times \left(x - x_p\right) +$$

$$\frac{a}{2!}\left[\left(-\frac{1}{\sigma^2}\right) exp\left(-\left(x_p - x_p\right)^2 \Big/ 2\sigma^2\right) + \left(-\frac{x_p - x_p}{\sigma^2}\right)^2 \times exp\left(-\left(x_p - x_p\right)^2 \Big/ 2\sigma^2\right)\right] \times \left(x - x_p\right)^2 + \cdots$$

The expression for $f(x)$ obtained is:

$$f(x) \cong a\left(1 - \frac{1}{2\sigma^2}\left(x - x_p\right)^2\right) = a - b\left(x - x_p\right)^2 \tag{5.25}$$

Where

$$b = -a \Big/ 2\sigma^2 \tag{5.26}$$

Now we have an expression for the differential counts curve for points near the peak. The median of the image should also be located near the peak. We can now use this expression to find the location of the median, labelled x_m. We start by finding the pixel closest to location of the median, labelled x_j, where $\mathrm{C}(x_j) < \mathrm{C}(x_m)$.

We find x_m by solving this equation:

$$\mathrm{C}(x_m) - \mathrm{C}(x_j) = \left(\frac{T_{Counts}}{2}\right) - \mathrm{C}_j = \int_{x_j}^{x_m} \mathrm{dC} = \int_{x_j}^{x_m} a + b\left(x - x_p\right)^2 \,\mathrm{dx} \tag{5.27}$$

Evaluating the integral:

$$\int_{x_j}^{x_m} a + b\left(x - x_p\right)^2 dx = a\left(x_m - x_j\right) + \frac{b}{3}\left[\left(x_m - x_p\right)^3 - \left(x_j - x_p\right)^3\right] \tag{5.28}$$

Plug this into the equation and rearrange to get:

$$ax_m + \frac{b}{3}\left(x_m - x_p\right)^3 = \left(\frac{N_T}{2}\right) - \mathrm{C}_j + ax_j + \frac{b}{3}\left(x_j - x_p\right)^3 \tag{5.29}$$

We can solve this cubic equation for to obtain the location of the median. x_m. The solution to the cubic we want is the one that satisfies: $x_m > 0$ & $\mathrm{Im}(x_m) = 0$.

Unlike the other median methods described, this method has the disadvantage of making an a priori assumption of the form of the distribution. It is also a computationally intensive method, and it may inhibit the implementation of data acquisition systems with faster sampling rates in the future.

5.3.3 Testing the Methods with Simulated Images

The performance of the algorithms described thus far was tested using simulated images. The criteria used to judge the performance of these algorithms is their robustness in the presence of photon shot noise. An array of integers from 1 to 2048 is used to represent the CCD's array of pixels, it will be referred to as the pixel array. The simulated image consists of 110 identical peaks. Each peak is constructed using the equation for the Gaussian distribution with the pixel array used as the input to produce an output array of photon count in each pixel produced by the peak. The center of each peak is set at regular intervals along the pixel array. The interval length and the parameters of the Gaussian function that generates the peaks were chosen to replicate real image data as closely as possible. The whole image is the sum of the photon count arrays of individual peaks (see Figure 5.9). Although real images possess non-Gaussian features, the methods investigated were designed to be independent of a priori assumptions of the form of the peak distribution (except for the Gaussian Parameters method) and should be equally applicable to both Gaussian and non-Gaussian peaks.

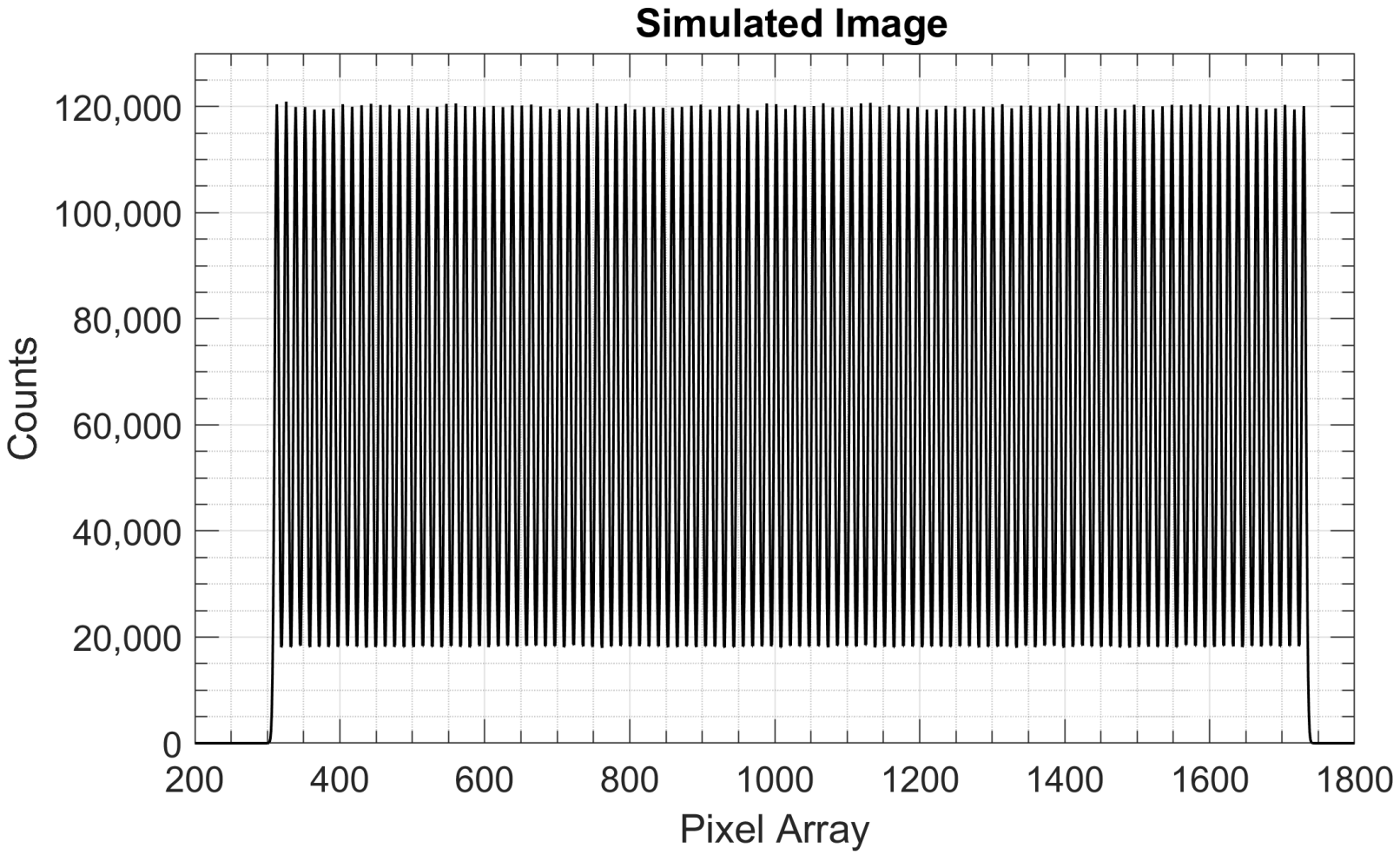

Figure 5.9: A simulated image. Each peak is generated by a Gaussian function. Noise is added to a pixel by random sampling of a normal distribution with zero mean and a standard deviation equal to the square root of the number of counts measured by the pixel.

Once the whole image has been generated, randomly generated noise in the photon count is introduced into each pixel to produce the final simulated image. Although fluctuations in photon count is Poissonian, for the large photon count numbers used in this simulation the Poissonian distribution converges to a normal distribution with a standard deviation equal to the square root of the average photon count. The noise in the photon count is generated by randomly sampling from this distribution. Ten thousand randomly generated simulated images are produced, representing a stationary image suffering with Poissonian fluctuations over time. The algorithms described thus far are applied to these images and the distribution of their results are analyzed. Since these images are stationary, the only factor that should change the results for the image position from one image to the next is the image's random Poissonian fluctuations. The "robustness" of the algorithm in the presence of photon shot noise is determined by the standard deviation of the distribution of the results. The smaller the standard deviation, the more robust the algorithm.

5.3.4 Results of Simulation

Each of the methods, with the exception of the Gaussian Parameters method, was applied to fifty thousand stationary, noisy, simulated images. The performance of these methods is measured by the standard deviation of these results. Fewer trials were performed on the Gaussian Parameters method due to the slow computation time. The distribution of the results of each method are plotted below.

The distribution in image position when the centroiding method is applied will be a useful baseline for improvement (Figure 5.10).

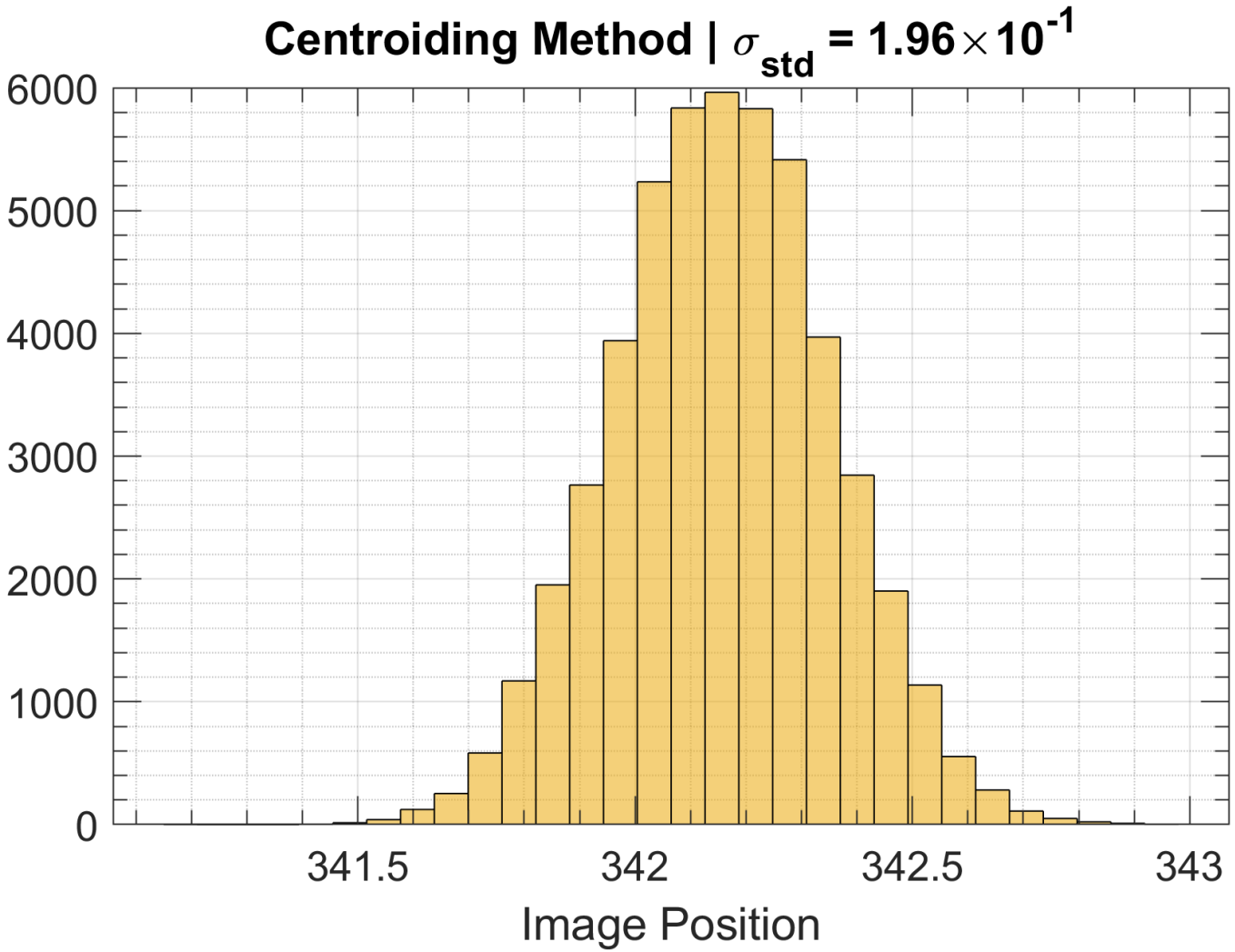

Figure 5.10: Distribution of image position using the centroiding method.

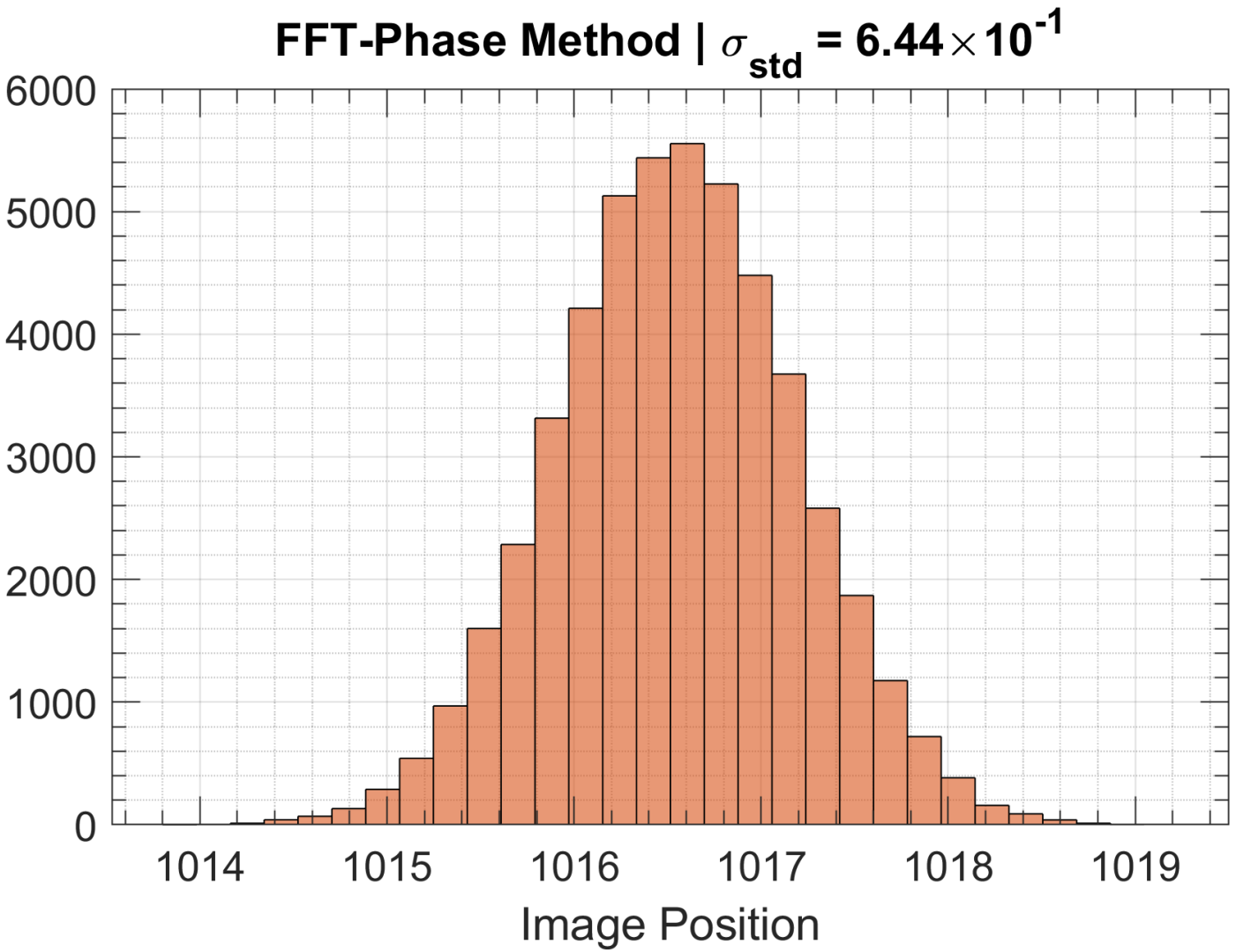

Figure 5.11: Distribution of image position using the FFT Phase method.

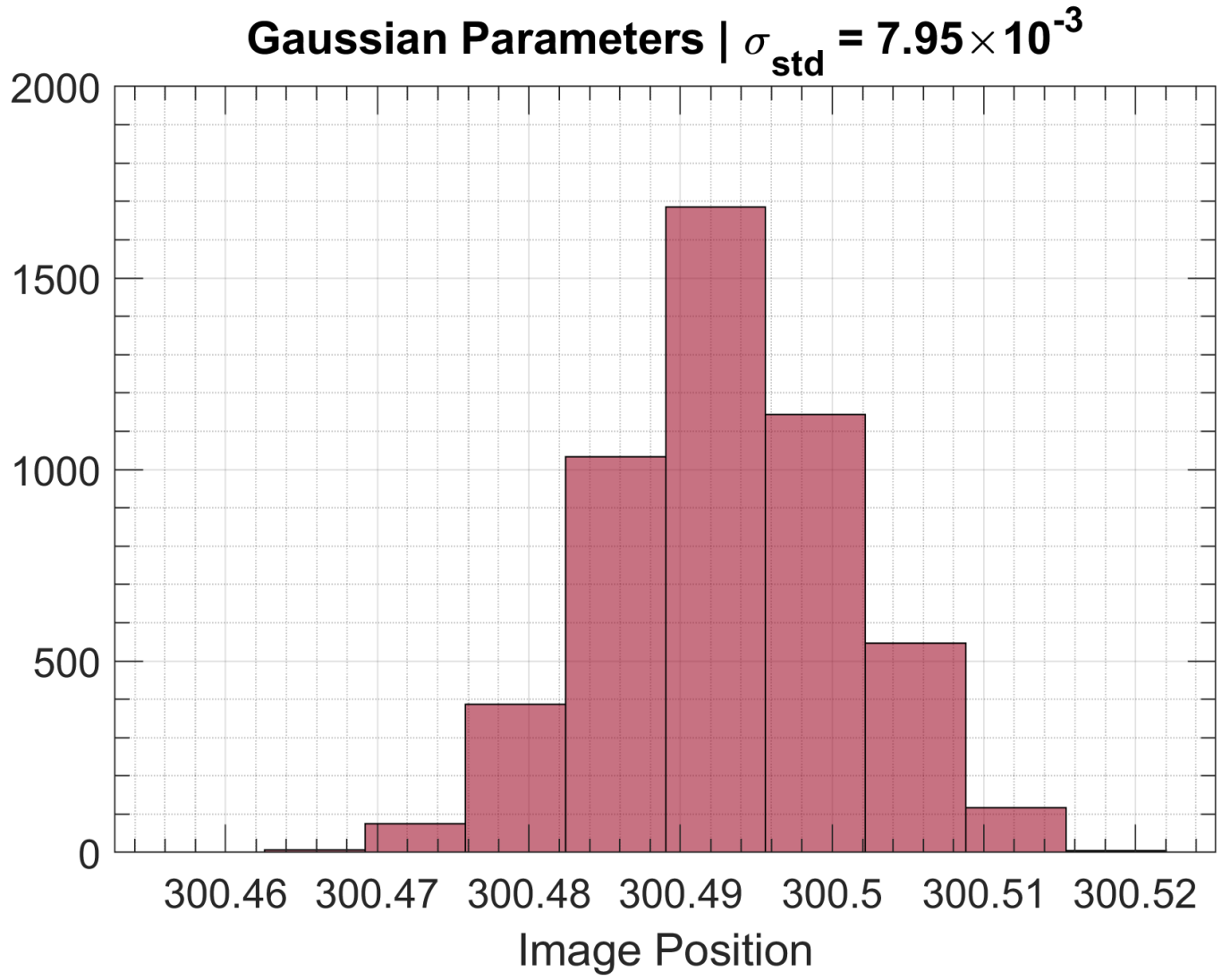

Figure 5.12: Distribution of image position using the Gaussian Parameters method.

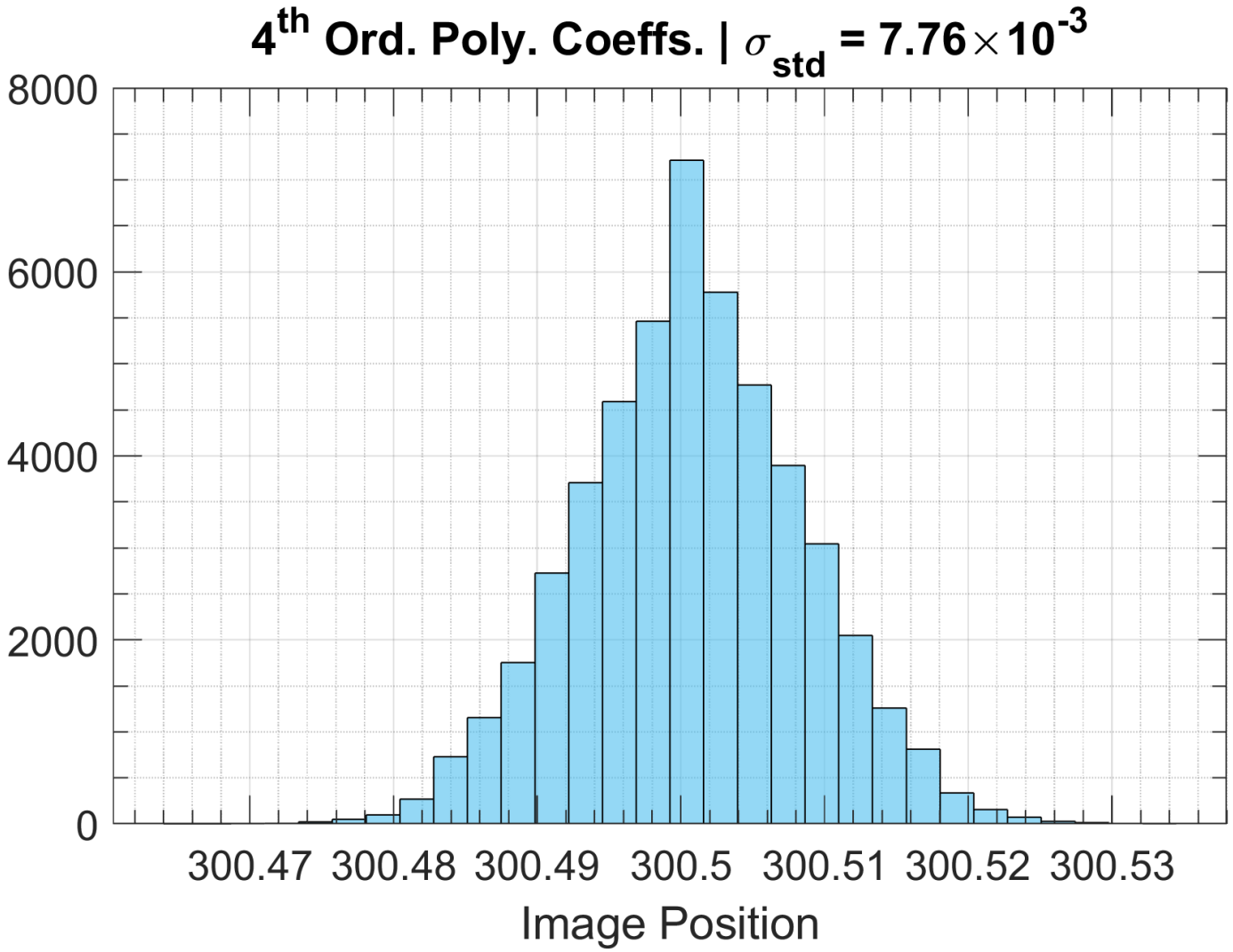

Figure 5.13: Distribution of image position using the 4th Order Polynomial Coefficients method.

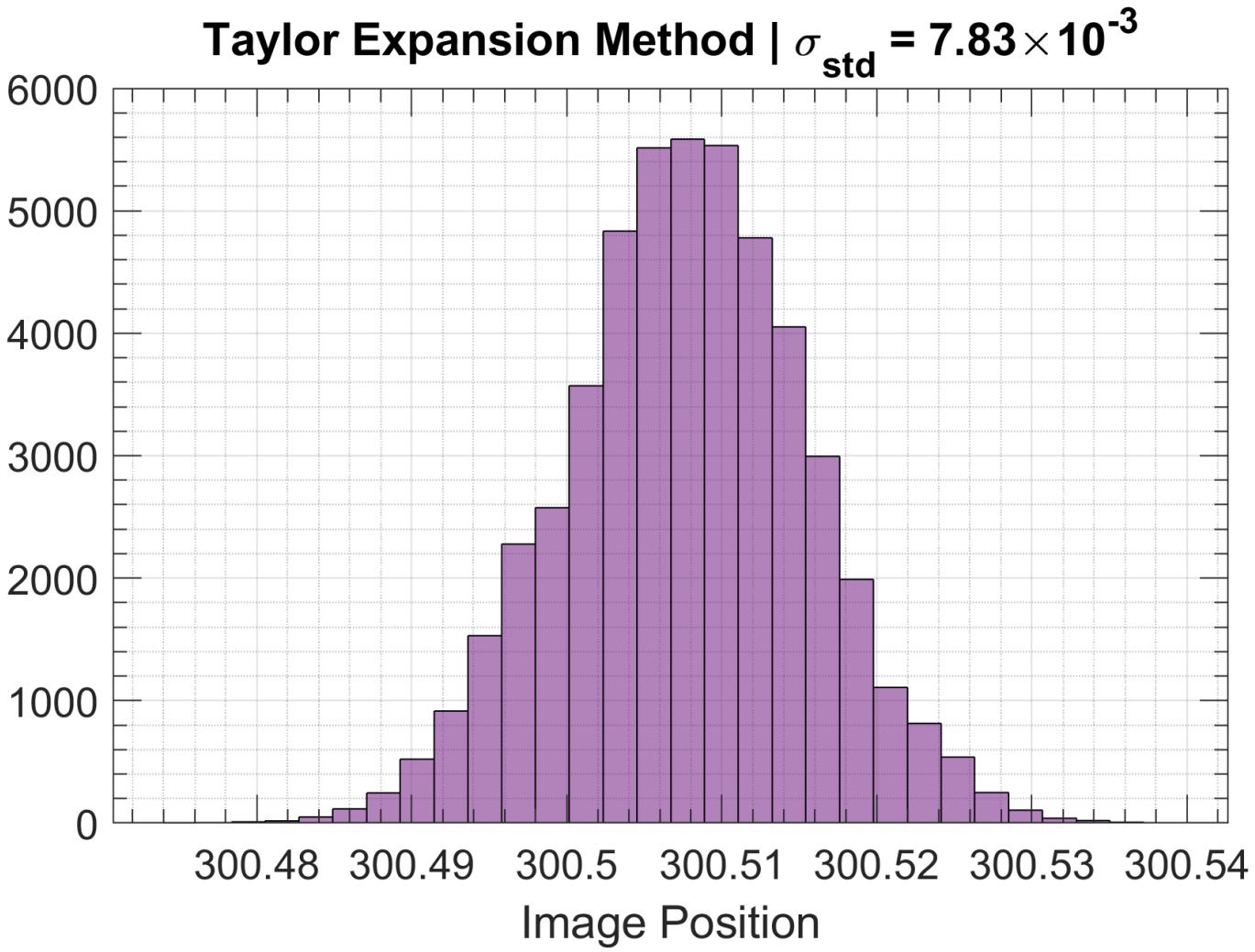

Figure 5.14: Distribution of image position using the Taylor Expansion method.

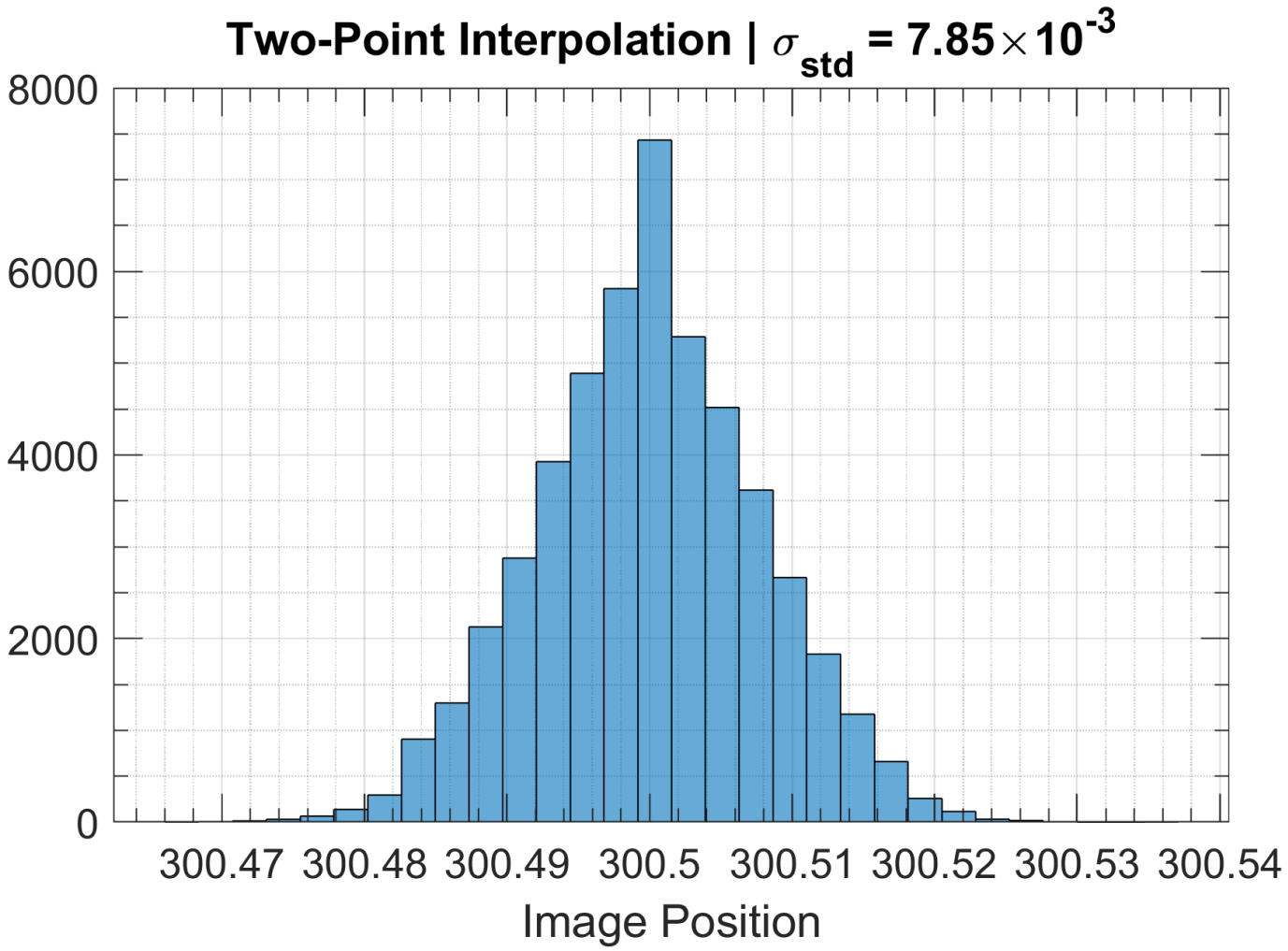

Figure 5.15: Distribution of image position using the Two Point Interpolation method.

The results show that the Taylor Expansion, 4th Order, and the Two-Point Interpolation algorithms are roughly comparable and significantly more robust than the centroiding method. The Two-Point Interpolation method chosen over the others for use in data collection, the simplicity of the Two-Point interpolation method allows for more clarity in its implementation.

5.4 Final Image Analysis Procedure

The balance position data is a time-series recording of the median of the whole image, sampled every half-second (2 Hz). The final image processing algorithm is implemented in LabVIEW, and the procedure is outlined, step by step:

0. IMAGE PREP: Position the image away from the edges of the pixel array.

1. IMAGE PREPROCESSING: Image data is an array with 2048 elements, each element corresponds to a pixel and contains the number of counts detected by the corresponding pixel.

    (i) Thresholding: all elements with counts below a threshold are set to zero.

    (ii) Estimate location & amplitude of valleys: Two methods of estimation have been implemented and examined for accuracy:

        (a) The PeakFinder VI in LabVIEW is set to detect valleys. This VI takes a threshold value greater than the valleys, and a value for the width of the valley (should be approximately ½ of the half-width of the peak).

(b) The PeakFinder VI in LabVIEW is better optimized for peak detection than valley detection. The image is first inverted to turn the valley into peaks, and then the PeakFinder VI is applied to find the peaks of this inverted image. A threshold value and peak width value can be provided as inputs. This approach produced accurate results for even highly noisy images and is comparatively less sensitive to the thresholds and peak width values.

(iii) Subtract remaining background noise: A second order polynomial is fit to the valley locations and valley amplitudes. The polynomial curve is calculated over the entire pixel array, and then subtracted out. This removes all of the remaining background noise. All negative values in the image array are set to zero.

2. IMAGE LOCALIZATION: The calculation of the image position.

(i) Separate the image into individual peaks: The data for an individual peak is a subset of the whole image - i^{th} peak is the subset of the whole image from the i^{th} valley to the $(i+1)^{th}$ valley.

(a) Width of each peak is calculated: Width of i^{th} peak is found by subtracting the location of the $(i+1)^{th}$ valley from the location of the the i^{th} valley.

(b) Generate fiducials for each peak

(ii) The Cumulative Sum (Counts) array (C. Sum array) is calculated: This calculation is carried out for each peak; each peak has a C. Sum array. The C. Sum array is calculated from the image array corresponding to a peak. Starting from the second element in the peak array, this element is replaced with the cumulative sum of all the elements before it.

(iii) Locate pixels adjacent to the median: The median of the image is defined as the location where the cumulative count distribution equals $\frac{N_T}{2}$, where N_T is the total number of counts in the peak: $C(x_m) = \frac{N_T}{2}$. The location of the median is estimated from the cumulative sum array elements corresponding to pixels adjacent to the median: $C(x_i) \leq \frac{N_T}{2} < C(x_{i+1})$.

3. For each peak, apply the Two-Point Interpolation Method to calculate the subpixel distance (dp) of the median from an adjacent pixel. The subpixel distance is added to the location of the median-adjacent pixel to obtain the location of the median of the peak along the pixel array. The difference between the median location of a peak and its corresponding fiducial is taken. The image position is obtained by averaging the results for each peak.

Chapter 6

Data Collection and Analysis

ABSTRACT:

This chapter discuss the data collected by the instrument from a roughly five-month period from January to May 2018. In addition to recording the balance deflection with the autocollimator, the instrument monitored the environmental parameters like temperature, pressure, and humidity in the bunker. The collected data is presented, and the significant features of the balance data are highlighted. Then we discuss the challenges associated with the analyzing this data and review of the methods developed and investigated to address these challenges. Finally, we describe the method that our investigation eventually converged on and apply the results of the analysis to place a limit on violations of the Equivalence Principle to gravitational fields produced by the sun and by galactic dark matter.

6.1 Data Collection

The instrument was in operation from late December 2017 to early June 2018. It took roughly four weeks for the balance drift to settle and to damp the balance oscillations down to an acceptable amplitude. The data used for analysis begins on January 19, 2018 at midnight ($t = 0$ at 1/19/2018, 00:00:00) and ends on May 14, 2018 at 6:58:19 am ($t = 9{,}961{,}099.44$ at 5/14/2018, 6:58:19).

In addition to the balance deflection, the temperature, temperature gradient, humidity, and pressure around the instrument chamber were recorded. Preliminary cross correlation analysis was carried out to determine the extent to which these variables influenced the balance. The results indicated minimum influence of these variable on the balance deflection. These environmental variables are presented in Appendix 6.2.

6.1.1 Balance Deflection Data

The balance data is shown in Figure 6.1. The most prominent features of the data are the trends and drifts in balance orientation over time, the torsional oscillations of the balance, and the high-frequency oscillations exhibited by the balance. A closeup of the torsional oscillations are shown in Figures 6.2 a-c and an example of the high-frequency oscillations are shown in Figures 6.3 a-b. These high-frequency oscillations are likely due to undamped pendular oscillations. The prominence of these features indicates that the balance eddy current damper and the fiber clamping mechanism requires improvement.

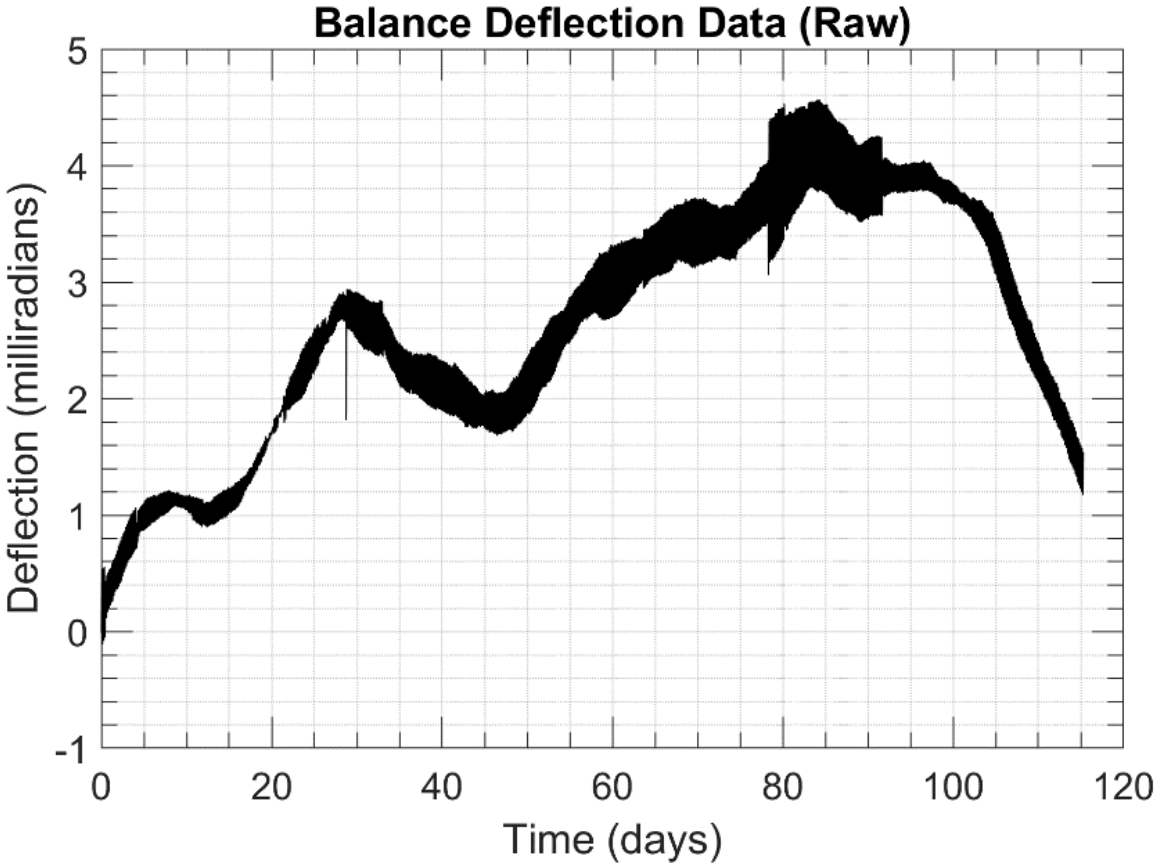

Figure 6.1: Plot of balance deflection over the approximately 110 days of data collection

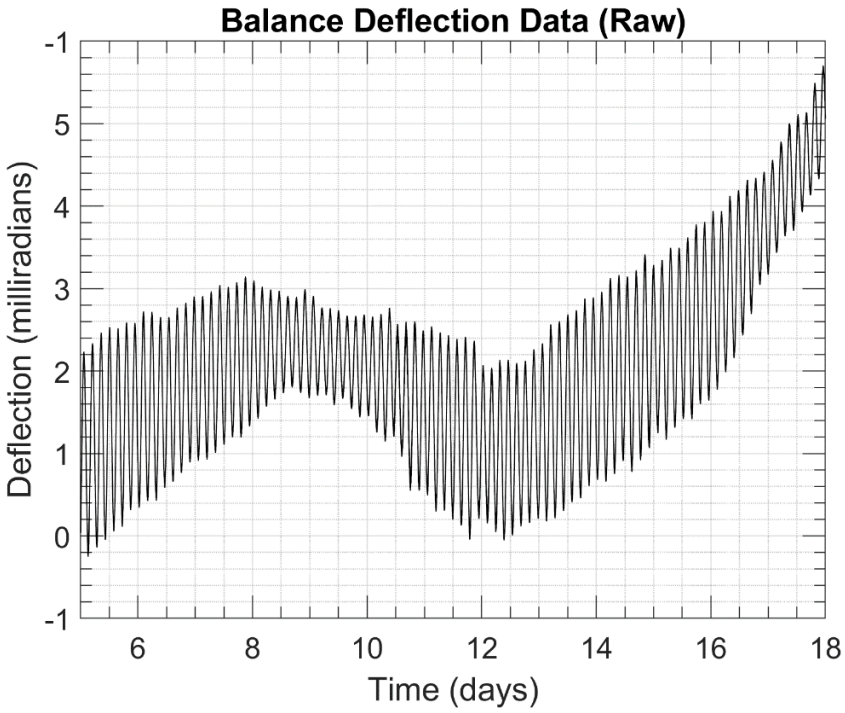

Figure 6.2a: Torsional Oscillations of the Balance

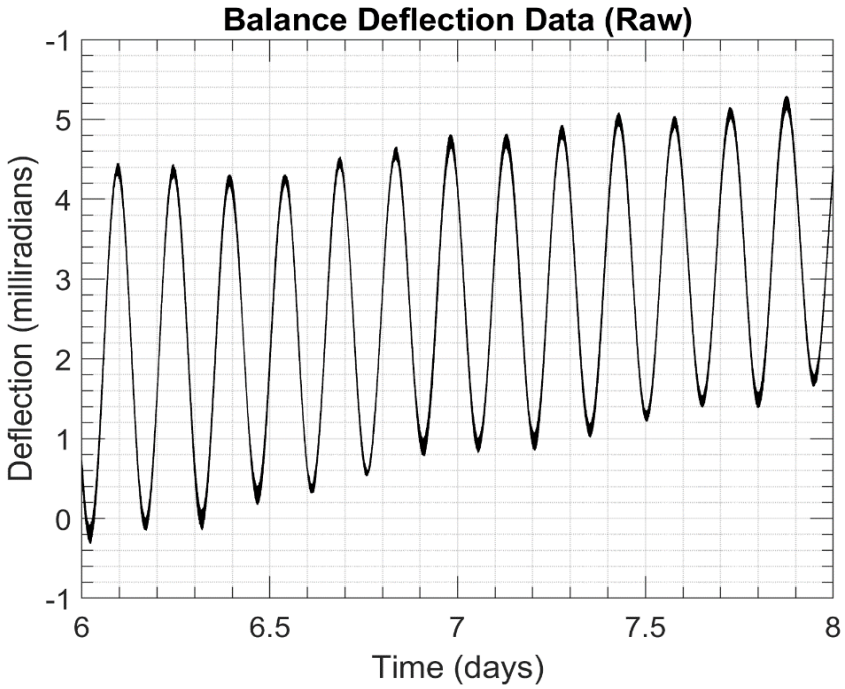

Figure 6.2b: Torsional Oscillations of the Balance

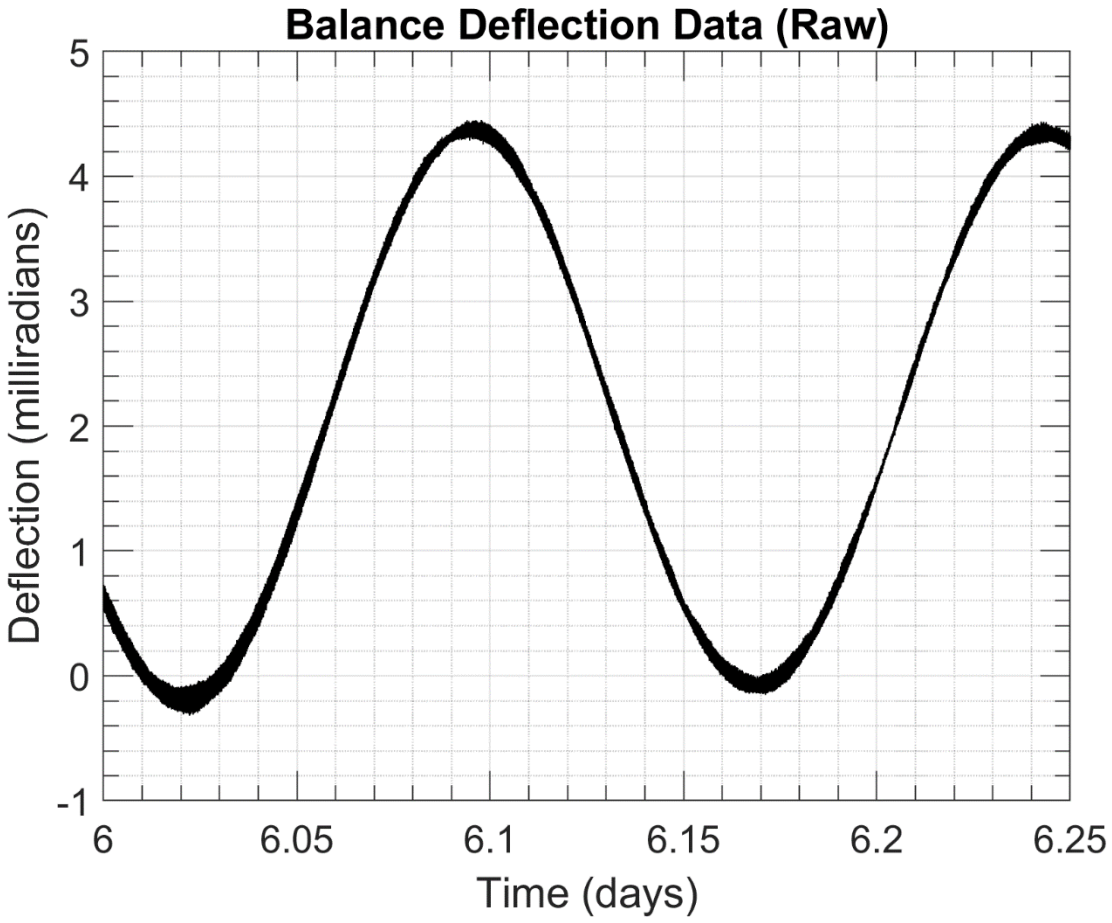

Figure 6.2c: Torsional Oscillations of the Balance

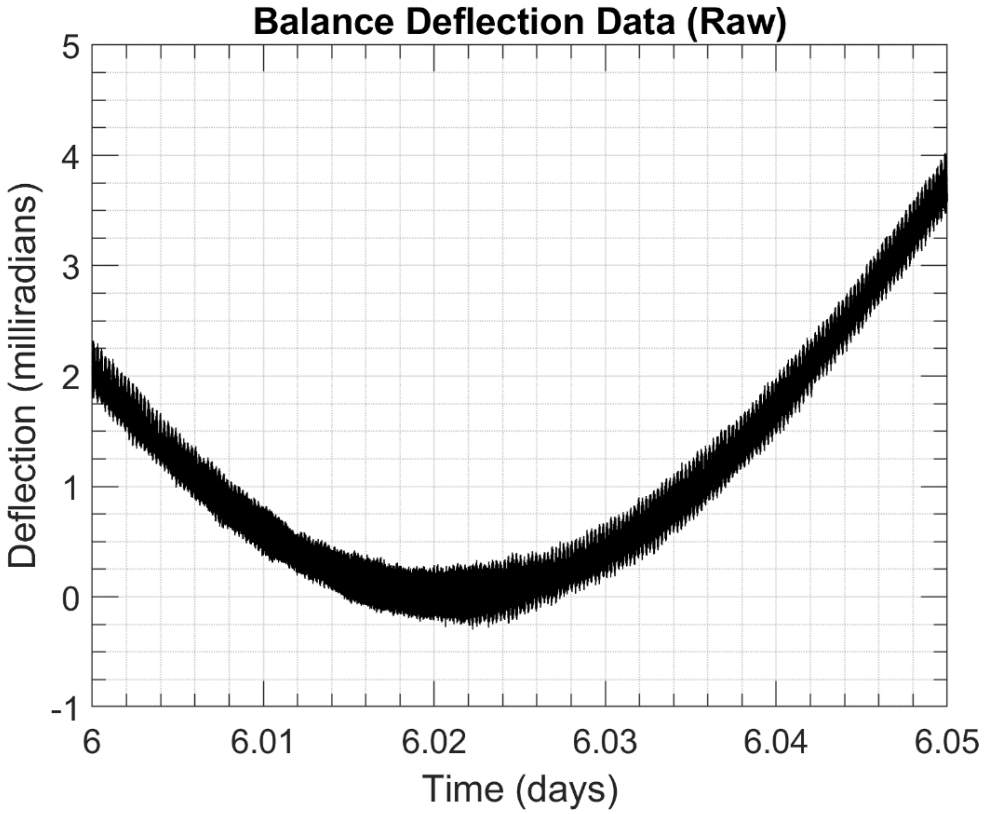

Figure 6.3a: High-frequency Oscillations of the Balance

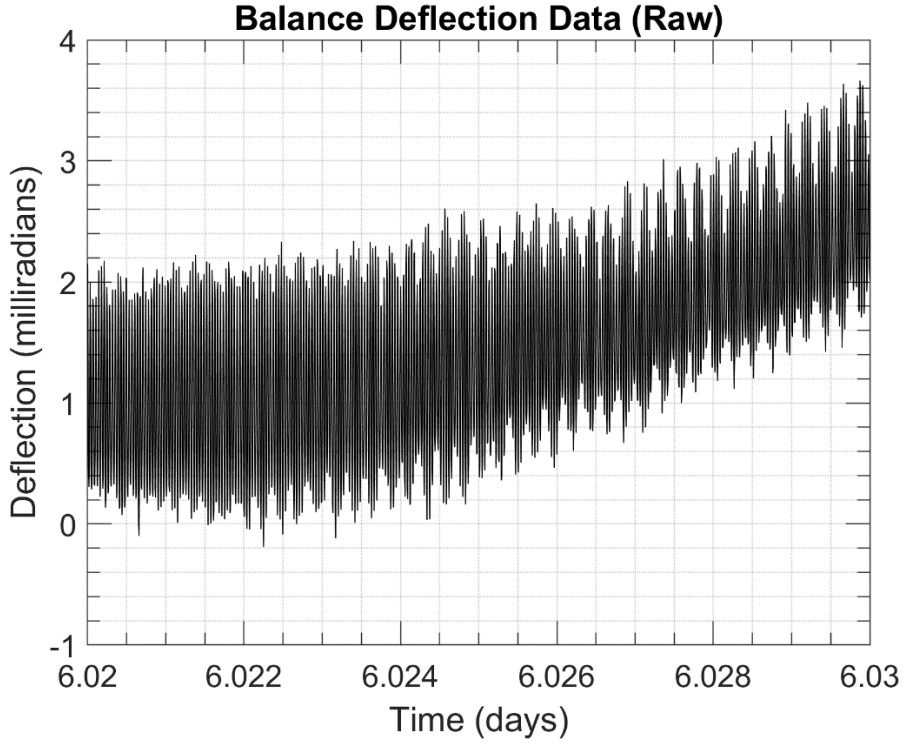

Figure 6.3b: High-frequency Oscillations of the Balance

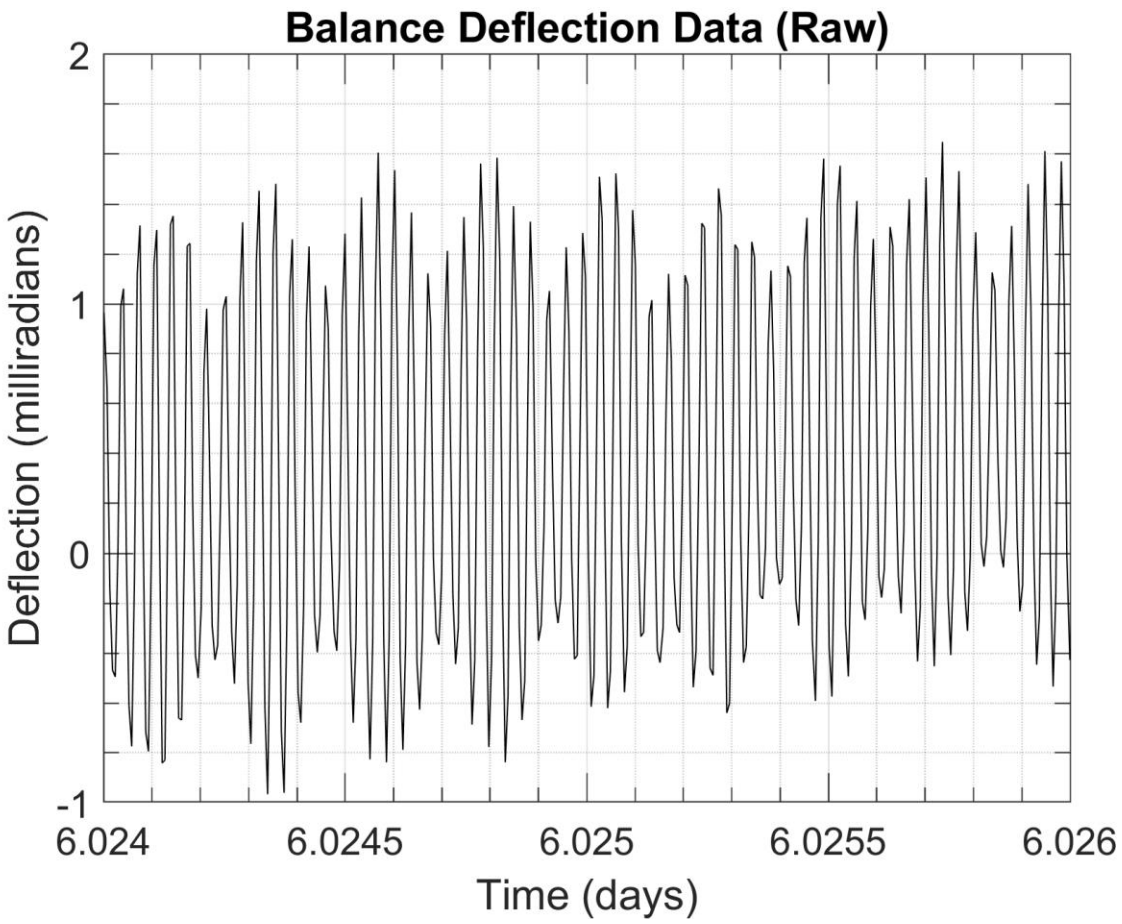

Figure 6.3c: High-frequency Oscillations of the Balance

6.2 Development of Analysis Methodology

The smallest upper-bound that can be placed Equivalence Principle (EP) violations is limited by the precision with which the EP-violating signals can be resolved and measured from the experimental data. An EP-violating torque, generated by an astronomical source, acting on our balance is modulated by the Earth's rotation and is precisely represented by a sinusoidal function. This signal is extracted and measured by taking advantage of the properties of sinusoidal function.

The precision of the analysis procedure is determined by the weakest signal that can be reliably measured. Improvements in the precision of the analysis will improve the bound placed on EP-violations. In order to distinguish such a faint signal from the data, the features in the data that drown out the signal must be subtracted out, the removal of these features must be carried out in such a way that we must be able to assert with confidence that the signal itself is not affected by the subtraction in any substantial manner.

Therefore, the primary challenge in the analysis is the elimination of all features in the data that would obscure a potential signal without eliminating or significantly distorting the signal itself. We must be able to assert with reasonable confidence that the removal of a feature will not prevent the faithful extraction of a potential signal. To this end, methods of analysis developed to for this purpose were carefully constructed to ensure that these extraneous features can be eliminated with only minimal distortions to potential EP-violating signals. Each of these methods will likely introduce some level of noise. Our effort is directed to ensuring that the analysis procedure does not result in an intolerable reduction of the signal.

6.2.1 Trend Removal

The first step of the analysis is to remove drifts and trends (referred to as trend removal). In order to minimize the introduction of artifacts in the analysis of forces acting on the balance during trend removal we only use the midpoints of the torsional oscillations - where the torque acting on the balance approach zero - to fit trends in the data. The fitting model uses 5 sine terms and 5 cosine terms of a Fourier series to estimate and subtract the trend. It is described in Appendix 6.2, where we demonstrate the application of this method a 12-day segment of the data.

6.2.2 Removal of Torsional Oscillations

Half-Cycle Sinusoidal Fit

This method divides each cycle of the torsional oscillations into half-cycles and applied a sinusoidal fit to these cycles and removes it from the data. Initially, we attempted to remove the torsional oscillations by fitting full cycles with a sinusoidal fit. However, it became evident that the torsional oscillations deviate from a purely sinusoidal oscillation due external forces acting on the balance. These oscillations are not symmetric, and they change in amplitude and shape over time. The removal of the torsional oscillations by fitting the full cycles induces distortions into the residual data due to the asymmetry of the oscillation. Attempts to compensate for the distortions induced by the subtraction of a sinusoidal fit produced unsatisfactory results. It was discovered, however, the distortions induced the subtraction of the fit can be minimized, and external signals better preserved, by dividing the data into half-cycles of an oscillation and fitting to these half-cycles.

First, a rough estimation of the peaks and valleys in the data is made using this smoothed data (see Figure 6.7). Next, the data set is segmented into half cycles. The first half cycle begins at a peak and ends at a valley. The locations and values of the peaks and valleys are stored in separate arrays. The extraction of the amplitude of diurnal signals from the half-cycle segments must be obtained from the estimation of the average force acting on the balance over the half-cycle.

This method is demonstrated using a 12-day long segment in Appendix 6.2.

6.2.3 Removal of High-Frequency Oscillations

Fourier Terms Subtraction

This method has been implement after the implementaion of the half-cycle fit. High frequency oscillations will be removed for each half-cycle segment. To keep continuity between segments, the last point in one segment will the first point in the next segment,

. The Fourier terms in each segment are calculated from the data. These segments are then subtracted from the data. Distortions of any underlying signals introduced during the removal of the high-frequency oscillation is minimized by subtracting terms whose mean is zero. The mean of each Fourier term subtracted is checked to ensure that this condition is met.

The first Fourier term calculated have a frequency of $2\pi/N$, where N is the number of data points in the segment. Each subsequent term is a multiple of this base frequency. The number of Fourier terms that are calculated equals the length of the segment. The frequencies

($\omega_i = \left(\frac{2\pi}{N}\right) * i$) of the Fourier terms calculated for each segment range from $\omega_1 = 2\pi/N$ to $\omega_N = 2\pi$.

Procedure for Calculating the coefficients of the Fourier terms:

i. At index i:

$$\mathrm{P(i)} \equiv \mathrm{P_i} \rightarrow \mathrm{P_i} = \sum_n \mathrm{a_n} \sin(\omega_n \times i) + \mathrm{b_n} \cos(\omega_n \times i) \tag{6.1}$$

ii. The frequency terms are given by: $\omega_n = \frac{2\pi n}{N}$, where *N* is the length of the segment

iii. $\mathrm{a_n}$ and $\mathrm{b_n}$ are calculated by:

$$\mathrm{a_n} = \frac{\sum_{i=1}^{N} \mathrm{P_i} \sin(\omega_n \times i)}{\sum_{i=1}^{N} \sin^2(\omega_n \times i)} \tag{6.2a}$$

$$\mathrm{b_n} = \frac{\sum_{i=1}^{N} \mathrm{P_i} \cos(\omega_n \times i)}{\sum_{i=1}^{N} \cos^2(\omega_n \times i)} \tag{6.2b}$$

6.2.4 Removal of Trends, Torsional Oscillations, High-Frequency Oscillation using 8th Order Butterworth Filters

The method eventually chosen to remove the drifts & trends, the torsional oscillations, and the high-frequency oscillations was the application of an 8th order Butterworth filters.

Butterworth filters were chosen for this analysis because they are *maximally flat* filters [39]. Butterworth filters were designed to maximize the passband flatness, with the drawback of possessing a more gradual roll-off. This ensures that the signal of interest is preserved with minimal distortions when this filter is applied. Butterworth filters of several different orders were

investigated for their ability to remove the undesirable features while persevering the signal. The 8^{th}-order Butterworth filter performed the best for the removal of the drifts & trends, torsional oscillations, and the high-frequency oscillations.

The drifts and trends were removed with a high-pass filter with a cutoff frequency corresponding to a period of 2 days. The torsional oscillations and the high-frequency oscillations were removed with a low-pass filter with a cutoff frequency corresponding to a period twice as long as the period of the torsional oscillations. These values were chosen to preserve the frequency of the EP-violating signal while maximizing the amount of the extraneous frequencies removed. The magnitude response curve of these filters is shown in Figure 6.4.

6.2.5 Signal Extraction from Calculation of Mean Acceleration:

Appendix 6.2 discusses additional efforts to develop an analysis method of estimating the mean acceleration of the balance that removes this noise while preserving the signal. These methods are applied after the removal of the features using a combination of the methods described above this data is referred to as the residuals and are applied to each half-cycle segment of the data. Here, we will discuss the method that was eventually chosen for implementation.

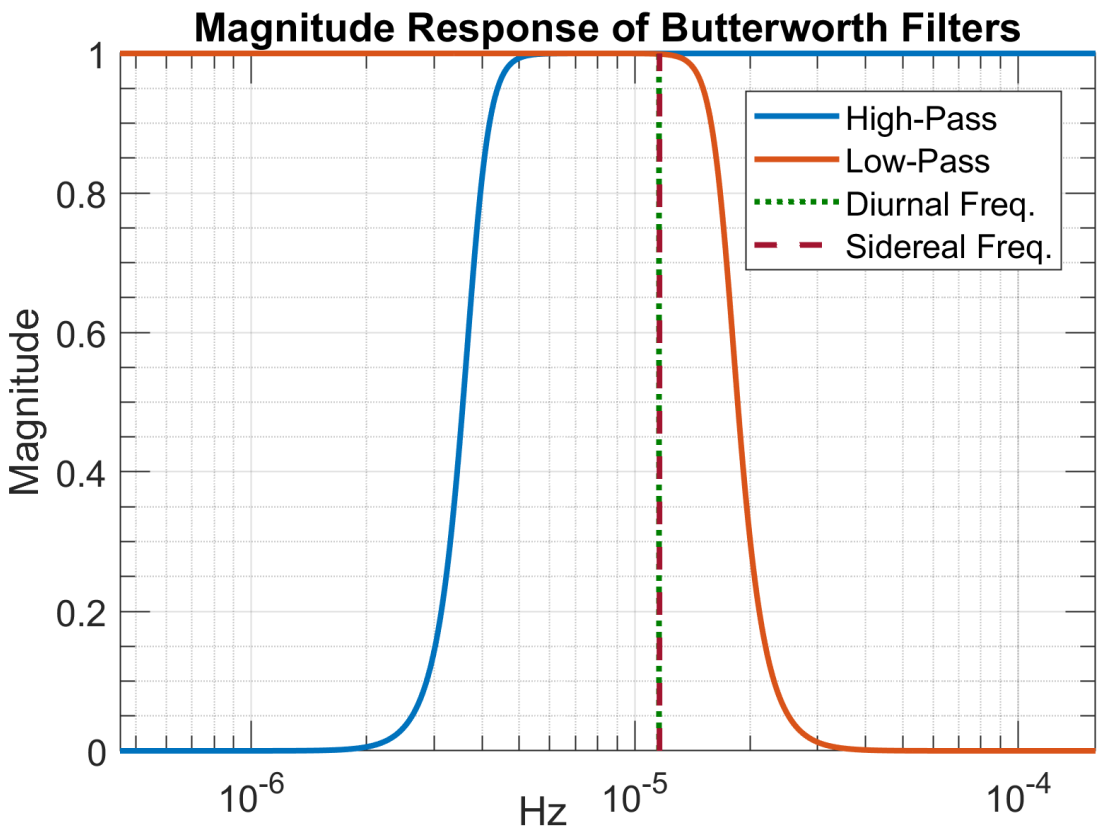

Figure 6.4: Magnitude response of the high-pass and low-pass 8th-order Butterworth filters. The diurnal frequency and the sidereal frequency, the frequencies of the EP-violating signals of interest, are marked,

Final Signal Extraction Method from Calculation of Mean Acceleration:

This method measures the mean acceleration of the balance by measuring the change in the velocity of the balance at roughly regular intervals. The ideal point to examine the behavior of the balance and calculate the mean acceleration of the balance over the period of an oscillation is to measure the change in the maximum velocity of the balance over period of oscillation. At the point of maximum velocity, the fiber restoration torque is zero and the only external forces act on the balance. The net effect of the external forces acting on the balance during a cycle is measured by the change in the maximum velocity from the previous cycle.

The sampling rate of this method is approximately one sample every $\sim 12{,}700$s, or around seven samples a day. This sampling rate is more than adequate to capture a diurnal or sidereal signal. We estimate the points in time when the velocity of the balance reaches its maximum value during an oscillation cycle. The max velocity locations are estimated by taking the first difference of the detrended data. First, smoothing (moving avg low pass filter) with a window length of 100 (points) is applied to remove the influence of high-frequency noise. Then, the first difference is calculated on this smoothed data, $\mathrm{d}\Phi$. The locations of the peaks in the first difference correspond to the points in the balance oscillations where the velocity is maximum.

Once the peaks in the $\mathrm{d}\Phi$ have been located, the filtered data around at these locations are analyzed to obtain the average acceleration. First, a linear fit is calculated using data 1000 seconds before and after, and the position of the balance near these points is described by:

$$\Phi_{fit}(t_i) = a + b \times t_i \tag{6.3}$$

The angular velocity of the balance at over this segment is obtained by differentiating this expression:

$$\frac{\mathrm{d}\Phi_{fit}}{\mathrm{d}t} = b \tag{6.4}$$

The mean acceleration of the balance over an oscillation cycle is calculated by numerical differentiation of the velocities at times corresponding to the peaks in $\mathrm{d}\Phi$: The change in maximum velocity of the balance must be due to external forces acting on the balance during an oscillation

$$\langle \ddot{\Phi} \rangle_j = \frac{b_j - b_{j-1}}{t_j - t_{j-1}} \tag{6.5}$$

The balance acceleration is sampled once every oscillation cycle, or about seven times a day, a sampling rate well above the Nyquist rate for the expected signal. The acceleration on the balance is related to the torque due to the signal by:

$$\langle \ddot{\Phi} \rangle = -\frac{\kappa_f}{I}\Phi + \frac{\tau_{signal}}{I} + \frac{\tau_{\mathrm{noise}}}{I} \tag{6.6}$$

The motion of the balance is dominated by the oscillation of the natural frequency. Accordingly, we set:

$$\Phi = -a \sin \omega_0 t + e \tag{6.7}$$

Where the e term corresponds to the other signals acting on the balance. It is obtained by calculating the mean value of the filtered position data over the segments. The corresponding acceleration is obtained by plugging Equation 6.7 into Equation 6.6:

$$\langle \ddot{\Phi} \rangle = -a\omega_0^2 \sin \omega_0 t - \omega_0^2 e + \frac{1}{I}(\tau_{signal} + \tau_{noise}) \tag{6.8}$$

The filtering, averaging, and the sampling at locations of maximum velocity removes the $-a\omega_0^2 \sin \omega_0 t$ term from Equation 6.8. The mean acceleration due to external torques is given by:

$$\frac{1}{I}\left(\tau_{signal} + \tau_{noise}\right) = \langle \ddot{\Phi} \rangle + \omega_0^2 e = \langle \ddot{\Phi} \rangle + \omega_0^2 \langle \Phi \rangle \tag{6.9}$$

The magnitude of the acceleration due to an EP-violating signal is obtained by extracting the component of $\langle d^2\Phi\rangle_j$ that is synchronous with the variation of the EP-violating signal by taking he inner product:

$$A_{EP} = \frac{\sum_j \left(\langle\ddot{\Phi}\rangle_j + \omega_0^2\langle\Phi\rangle\right)\times\cos(\omega_{EP}t_j+\varphi)}{\sum_j\left(\cos\left(\omega_{EP}t_j+\varphi\right)\right)^2} \tag{6.10}$$

Where φ is the phase of the signal at $t = 0$.

6.3 Data Analysis: Procedure, Results, and Conclusions

6.3.1 Data Analysis Procedure

1. The data is converted from pixel units to radians.

2. Remove Linear Trend: The initial position is set to zero, and a linear fit is calculated and subtracted out. See Figure 6.5.

3. The data is prepared for filtering and analysis by applying a Tukey window to reduce influence of edge effects from filtering.

4. Removal of Trends: Φ is detrended by applying an 8^{th} order high-pass Butterworth filter to the windowed position data. A cutoff frequency with a period of two days is used. See Figure 6.6.

5. Removal of High Frequency Noise and Torsional Oscillations: Torsional oscillations and higher frequency components are removed by applying an 8^{th} order low-pass

Butterworth filter to the detrended data. A cutoff frequency with a period 2 times the period of the torsional oscillations is used. Filtered data plotted in Figure 6.7.

6. Calculate $\langle\ddot{\Phi}\rangle$ for all cycles. We want the amplitude of the differential acceleration arising for EP-violation in units of m s^{-2}. The conversion is described in Chapter 3.

$$\langle\Delta a\rangle = \frac{I_m}{mR\sqrt{s}}(\langle\ddot{\Phi}\rangle + \omega_0^2 e) = 0.76 \times (\langle\ddot{\Phi}\rangle + \omega_0^2\langle\Phi\rangle) \tag{6.11}$$

Balance acceleration data plotted in Figure 6.8. The distribution of $\langle\Delta a\rangle$ values is shown in Figure 6.9. A Gaussian was fit to this distribution data to obtain the standard deviation of the $\langle\Delta a\rangle$ values. Values of $\langle\Delta a\rangle$ greater than 2.5 times this standard deviation were considered outliers. Several of these values coincided with nearby earthquakes, and it is likely that these values arose due to external shocks.

7. Calculate the magnitude of the EP-violating signal:

$$\Delta a(\mathrm{Al} - \mathrm{SiO_2}) = \frac{\sum_j \langle\Delta a\rangle_j \times \cos(\omega_{EP} t_j + \varphi)}{\sum_j (\cos(\omega_{EP} t_j + \varphi))^2} \tag{6.12}$$

8. Calculate the Uncertainty: The uncertainty is obtained by calculating the inner product of $\langle\Delta a\rangle$ and signals with frequencies adjacent to the expected frequencies of EP-violating signals $(\omega_{adj} = 2\pi f_{adj})$.

$$A_{Err} = \frac{\sum_j \langle\Delta a\rangle_j \times \cos(\omega_{adj} t_j + \varphi)}{\sum_j (\cos(\omega_{adj} t_j + \varphi))^2} \tag{6.13}$$

Over the range of chosen frequencies, the high-pass and low-pass Butterworth filters preserved the signals to about 98% or better fidelity.

A trend line is fit for the results:

$$A_{err,Trend}(f_{adj}) = a + b \times f_{adj} \tag{6.14}$$

The results for frequencies adjacent to the diurnal and the sidereal frequency are shown in Figure 6.10. The uncertainty in the results is defined as the RMS deviation of the projections from the trend line:

$$RMSD_{\langle \Delta a \rangle} = \pm \sqrt{\sum_{j=1}^{N} (A_{err,j} - A_{errTrend,j})^2 \Big/ N} \tag{6.15}$$

For an EP-violating signal with a diurnal and a sidereal frequency, the rms uncertainty in $\langle \Delta a \rangle$ is estimated to be:

$$RMSD_{\langle \Delta a \rangle} = \pm 3.46 \times 10^{-14} \text{ m s}^{-2} \tag{6.16}$$

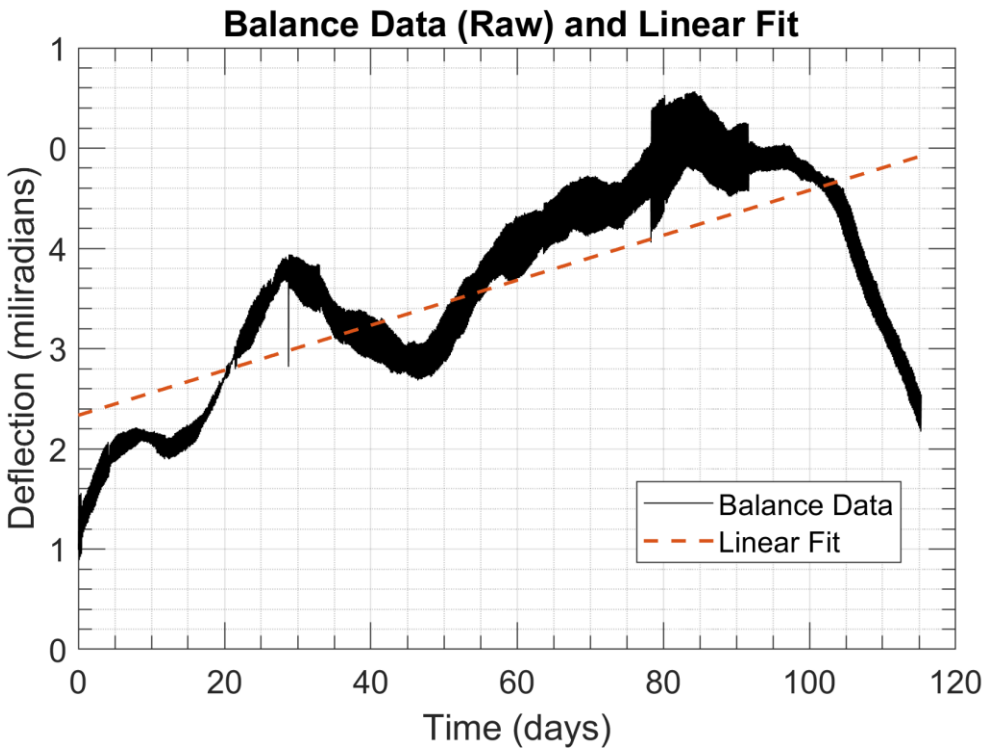

(a)

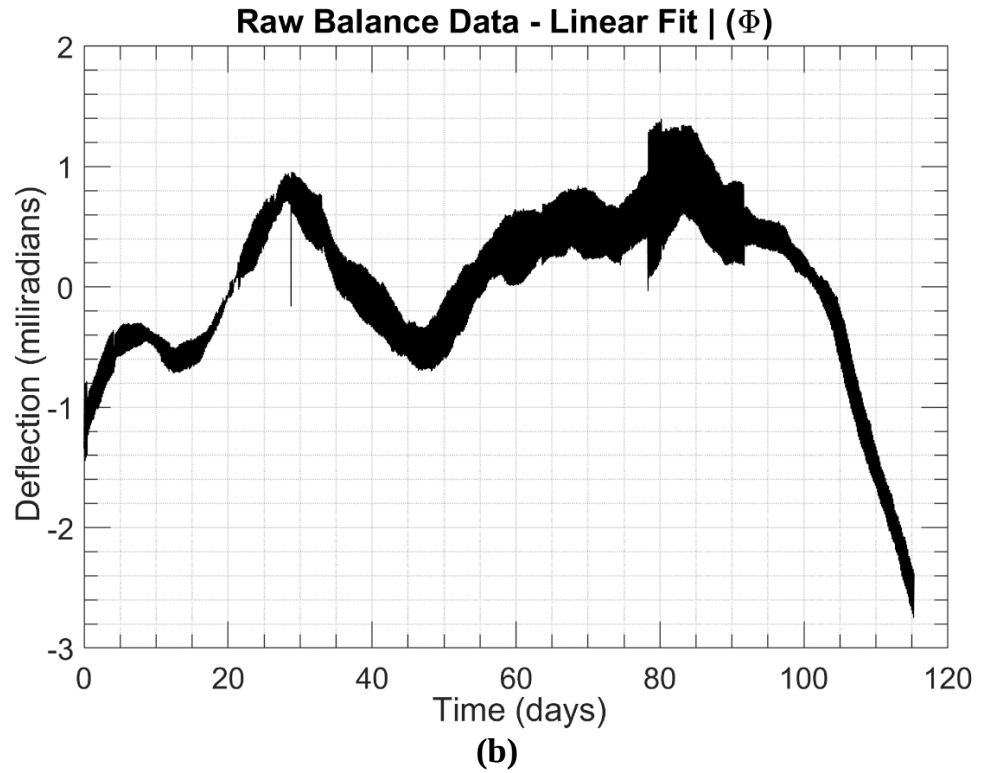

(b)

Figure 6.5: (a) Plot of the balance data and the Linear fit to be subtracted. (b) Plot of the data after subtraction of the linear fit

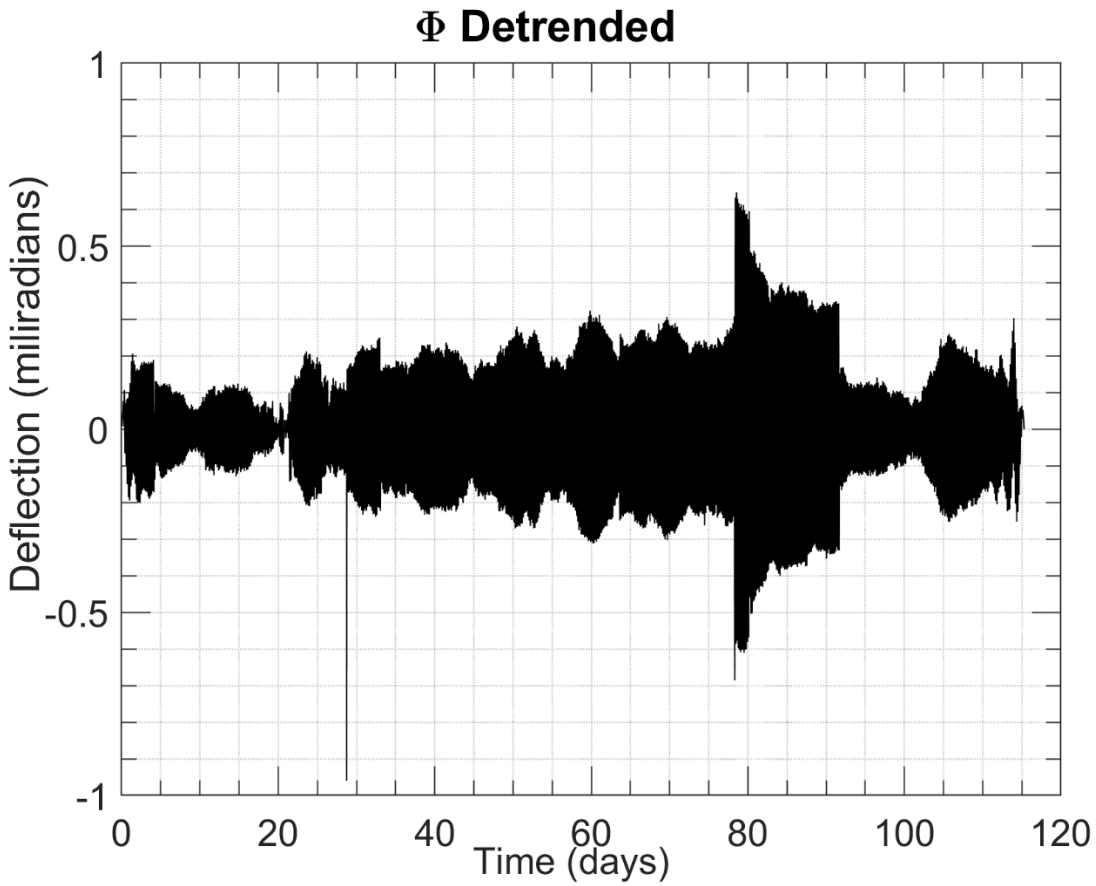

Figure 6.6: Plot of detrended data after application of high-pass filter

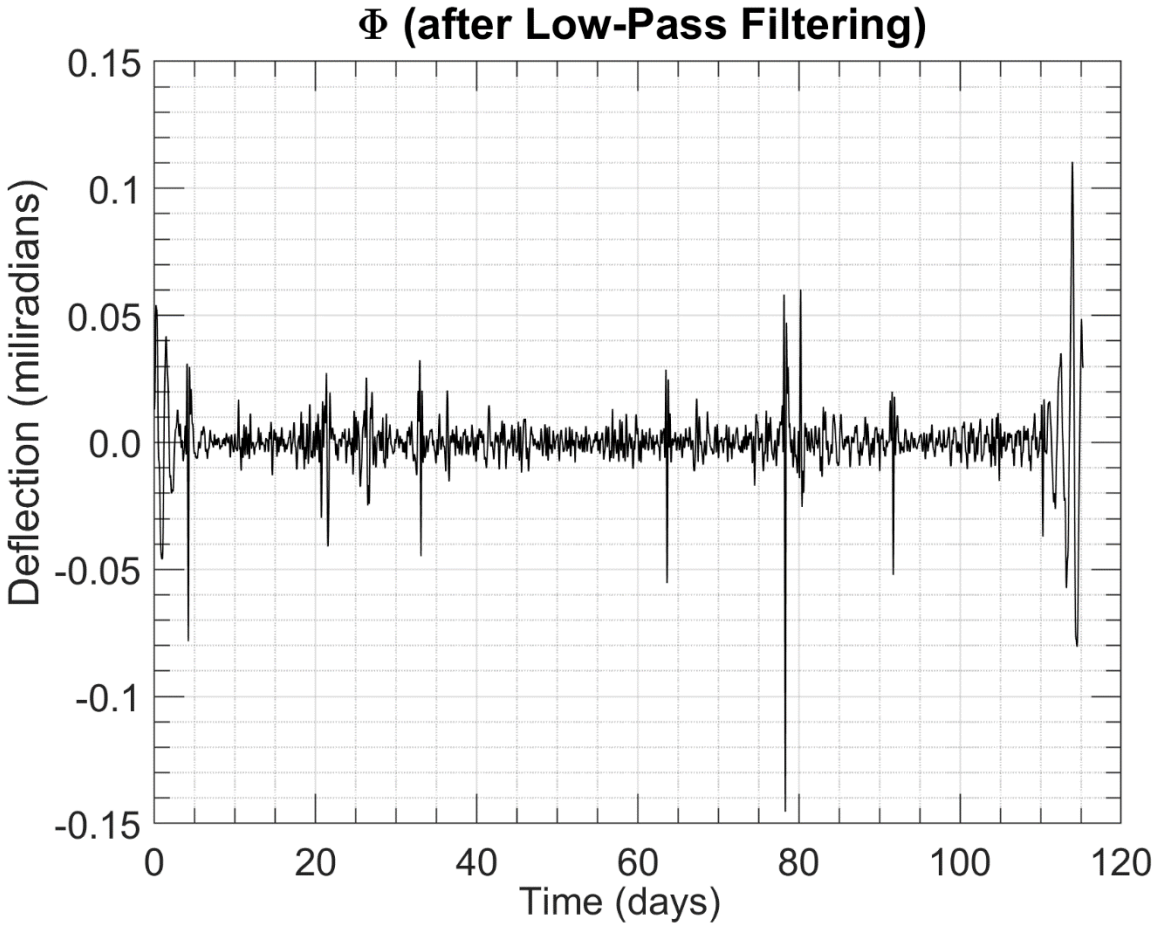

Figure 6.7: Plot of filtered data after application of low-pass filter

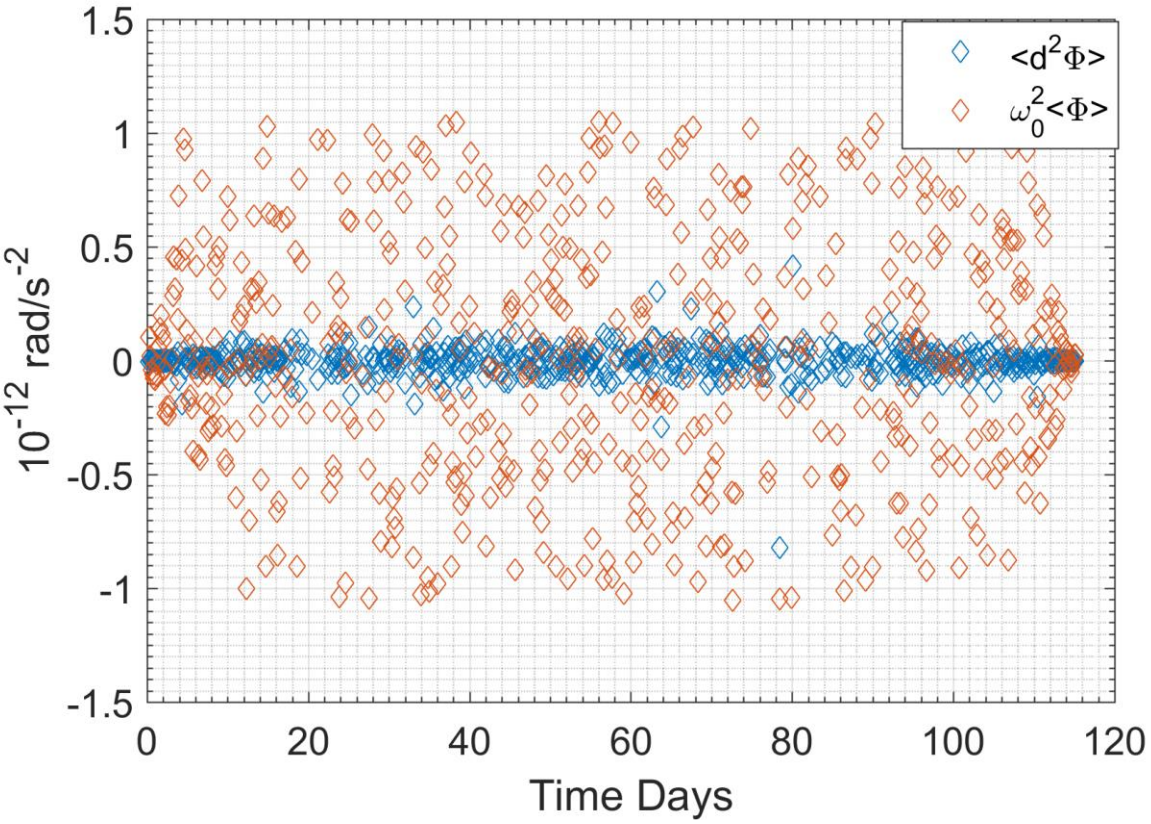

Figure 6.8: Differential acceleration of masses in the balance and acceleration due to other external torques.

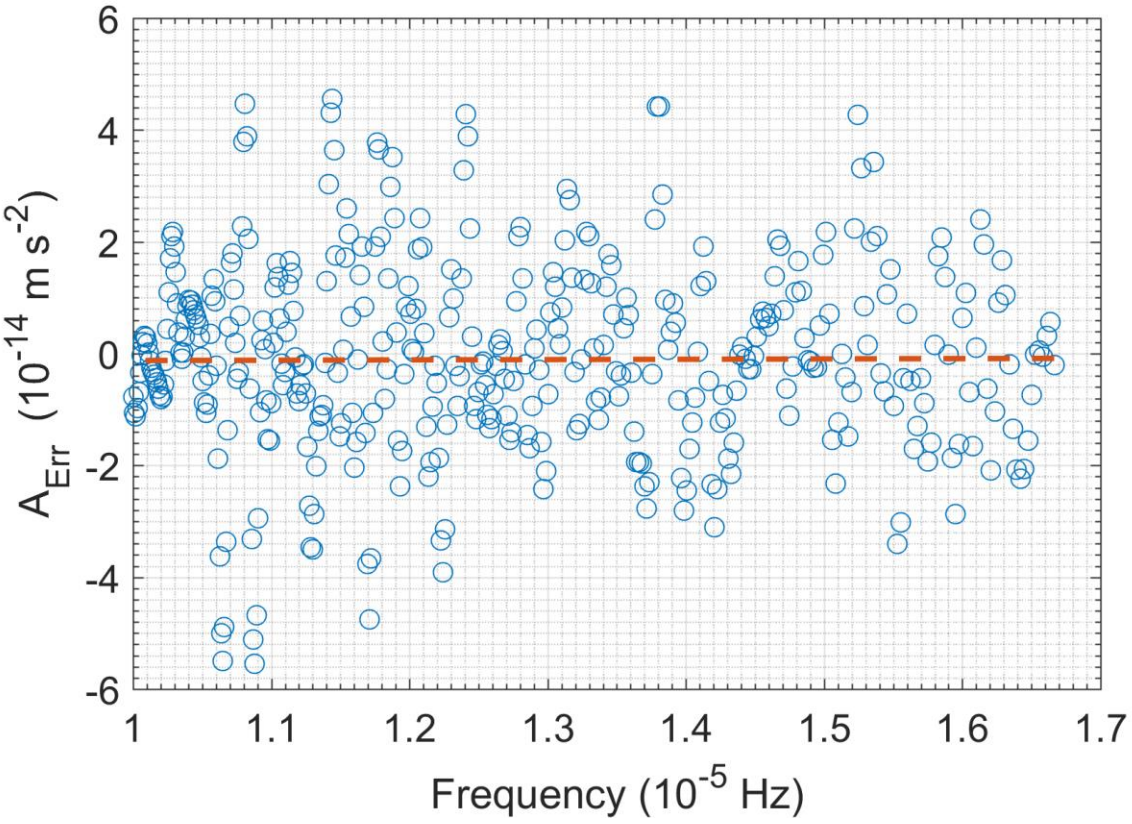

Figure 6.9: Results of inner product for frequencies adjacent to the diurnal frequency and the sidereal frequency

6.3.2 Results and Conclusions

This data-analysis method was applied to search for WEP-violations in the gravitational field of the sun (the solar attractor), and violations in the field of galactic dark matter. This section describes the results of the analysis for each case.

It is to be noted that the balance orientation was along the East-West axis. As shown in Chapter 3, the results obtained from operating the balance along the North-South orientation would have improved the results by a factor of ~ 0.625.

Solar Attractor:

The EP-violating signal in the gravitational field of the sun has a period of one solar day, or 86,400 s. The amplitude of the differential acceleration due to EP-violation calculated from our data is:

$$\Delta a_{\odot}(\mathrm{Al} - \mathrm{SiO_2}) = (1.06 \pm 3.46) \times 10^{-14}\ \mathrm{m\ s^{-2}} \tag{6.13}$$

The amplitude gravitational acceleration due to the sun on earth is $a_{\odot} \approx 0.0059\ \mathrm{m\ s^{-2}}$. The Eötvös parameter for the Solar attractor is:

$$\eta_{\odot}(\mathrm{Al} - \mathrm{SiO_2}) = \frac{\Delta a_{\odot}}{a_{\odot}} = [1.80 \pm 5.86] \times 10^{-12} \tag{6.14}$$

Galactic Dark Matter

We obtain the acceleration due to Galactic dark matter from the detailed analysis of Galactic dark matter distribution carried out by Burch and Cowsik [40]. Their analysis indicates that, at the location of the solar system, the speed of Galactic rotation is $\sim 240\ \mathrm{km\ s^{-1}}$. They also

calculated that the visible baryonic matter in the galaxy contributes a gravitational pull to counteract the centrifugal force due to this rotation to ~190 km s^{-1} of the rotation speed. Accordingly, the acceleration due to Galactic dark matter that contributes to any EP-violating torque:

$$A_{DM} = \left[\frac{V_C^2 - V_{vis}^2}{R_{GC}}\right] \cos\varphi(t) \cos a(t) \tag{6.15}$$

Here, V_c is the rotational speed of the Galaxy, at the distance of the solar system from the center of the galaxy, $V_c \approx 240$ km s^{-1}. V_{vis} is the contribution to this rotational speed from visible matter, $V_{vis} \approx 190$ km s^{-1}, and $\varphi(t)$ and $a(t)$ represent, respectively, the azimuth and altitude of the Galactic center in horizontal coordinates over the course of a sidereal day.

We assume that the gravitational acceleration is directed to the Galactic center and that the location of Sag A*, the supermassive black hole at the center of the galaxy, is a good approximation for the location of the Galactic center. Choosing the expressions for $\varphi(t)$ and $a(t)$ appropriate for the longitude and latitude of St. Louis, we obtain the following expression for the acceleration due to Galactic dark matter:

$$A_{DM} = 4.58 \times 10^{-11} \sin h(t) \text{ m s}^{-2} \tag{6.16}$$

Where $h(t)$ is the hour angle of the source. $h(t)$ evolves uniformly due to the rotation of the Earth with the sidereal frequency: $\omega_* = \frac{2\pi}{1 \text{ sidereal day}} = 7.2921 \times 10^{-5}$ rad s^{-1}. The amplitude of the acceleration is then: $a_{DM} = 4.58 \times 10^{-11}$ m s^{-2}.

The amplitude of the differential acceleration due to EP-violation calculated from our data is:

$$\Delta a_{DM}(\mathrm{Al}-\mathrm{SiO_2}) = (-3.58 \pm 3.46) \times 10^{-14}\ \mathrm{m\ s^{-2}} \quad (6.17)$$

And the Eötvös parameter for Galactic dark matter is:

$$\eta_{DM}(\mathrm{Al}-\mathrm{SiO_2}) = \frac{\Delta a_{DM}}{a_{DM}} = [-7.82 \pm 7.56] \times 10^{-4} \quad (6.18)$$

Conclusions

The collected data and results have identified several areas in which the instrument and analysis method can be improved. The noise in the data is substantial and further development of the analysis method is required. The use of the filters with methods discussed in Appendix 6.2 may yield further improvements in the results of the analysis. A more sensitive recording of the various sources of noise will allow for cross-correlation and subtraction of their influence. Improvements to the damping mechanisms will remove many of the troublesome high-frequency oscillations.

Appendix 6.1: Temperature, Pressure, and Humidity

The temperature data was obtained using thermistors placed around the instrument. The pressure and humidity data were obtained from a weather station placed within the insulation of the instrument. These thermistors were placed in the middle of the instrument and used to calculate temperature gradients across the instrument.

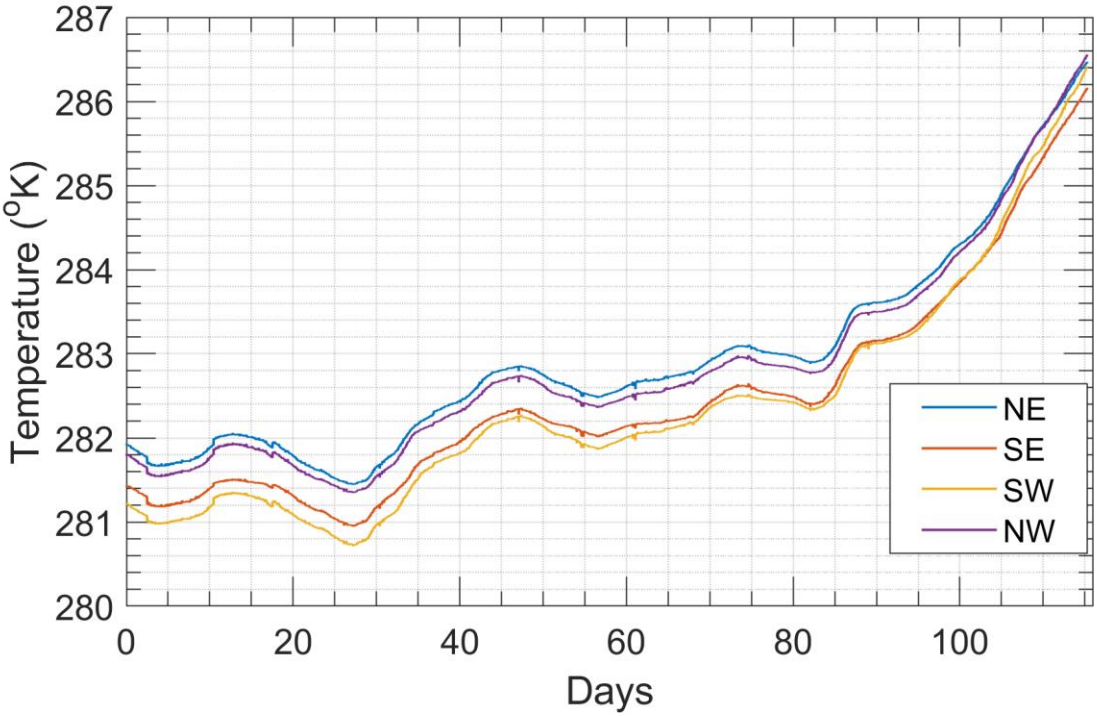

Figure A6.1.1: Plots of the thermistors placed at the North-East (M1), North-West (M2), South-West (M3), and South-East (M4) corners of the instrument.

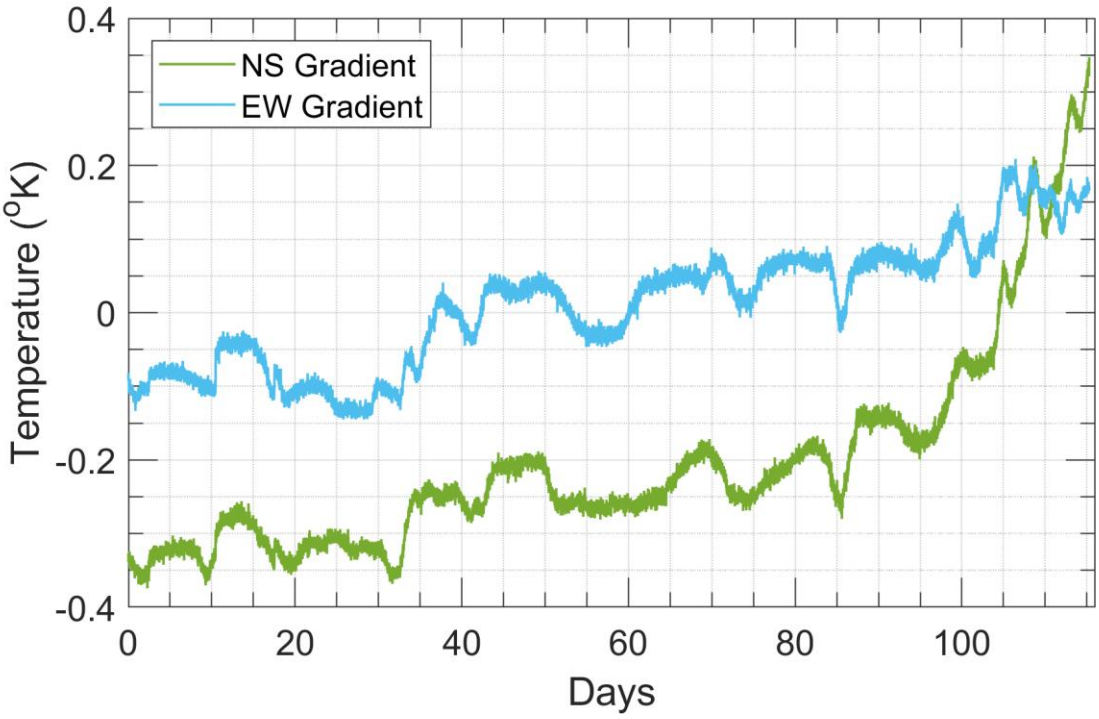

Figure A6.1.2: Temperature gradients across the instruments. North-South gradient in blue. East-West gradient in red.

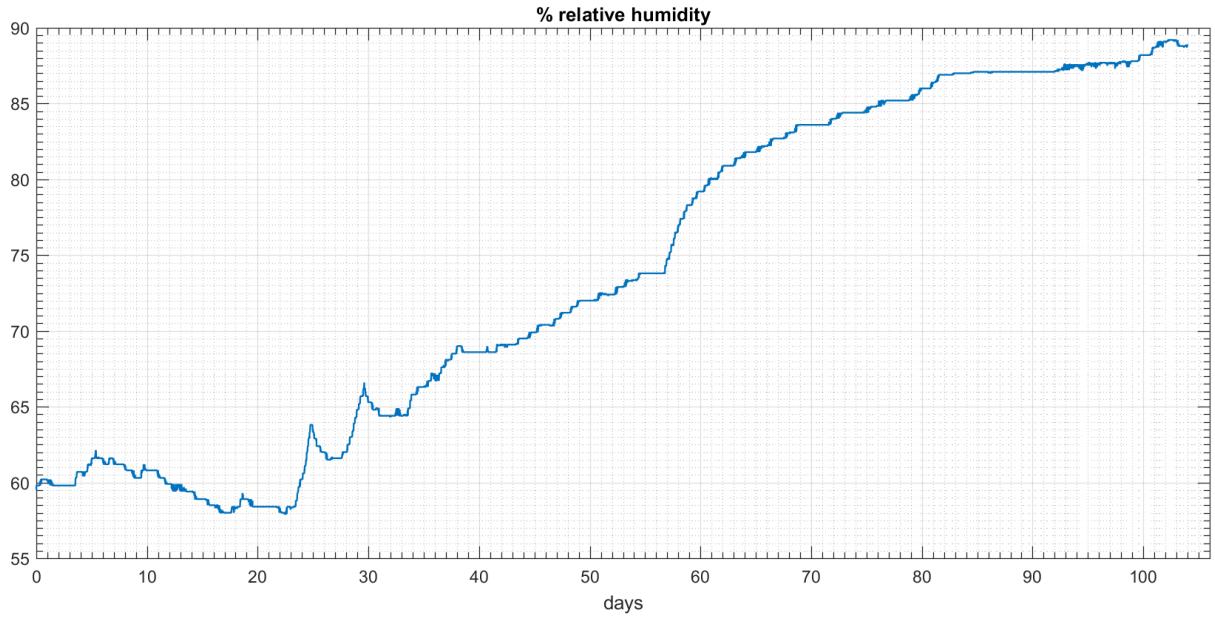

Figure A6.1.3: Percent Relative Humidity (from 1/22 to 5/6, 2018)

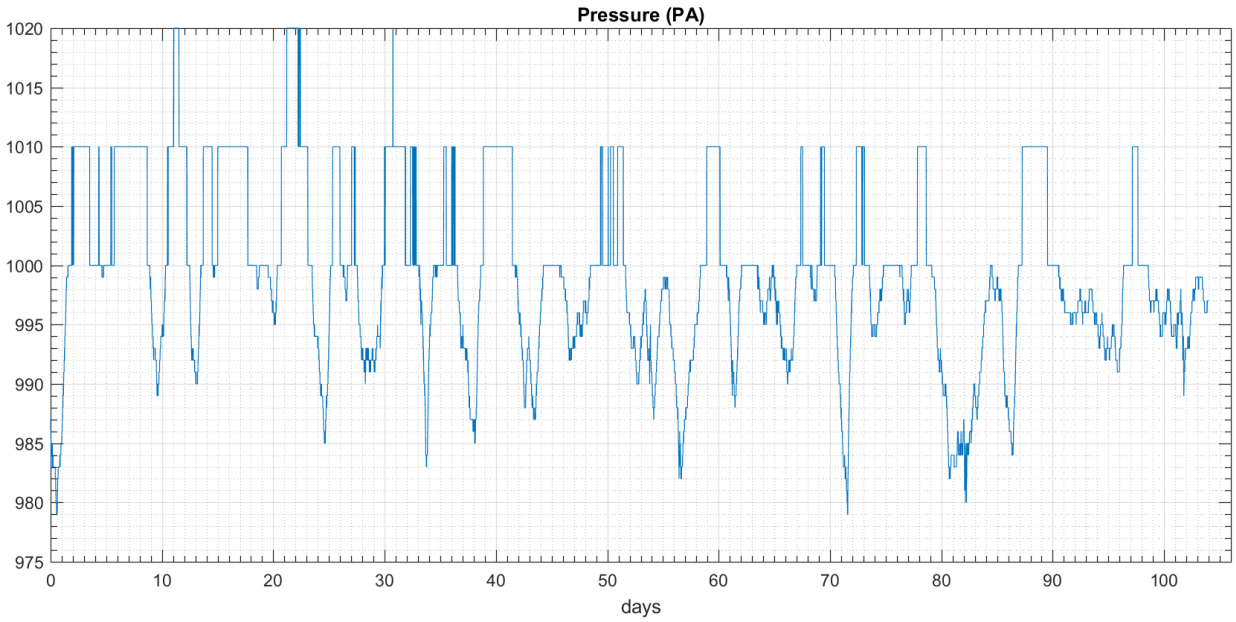

Figure A6.1.4: Pressure in Pascals (from 1/22 to 5/6,2018)

Appendix 6.2: Removal of Extraneous Feature from Data

This chapter will describe a few of the other methods investigated during the development of the analysis procedure.

A6.2.1 Trend Removal

The midpoints are calculated by first finding the peaks and valleys of the torsional oscillations. The data set is smoothed using a moving average over 1000 points. This removes the remove high-frequency oscillations, which prevent peak finding routines from identifying the peaks and valleys of the torsional oscillations. The peak finding routine can now estimate the location of the peaks and valleys of the data without fear of mislabeling peaks and valleys.

In this data segment, there are 81 peaks and 80 valleys (there is a peak at the beginning and end of the data). The number of midpoints will be equal to twice the number of valleys (160 midpoints).

The position midpoints are calculated by taking the sum of the peak and the valley and dividing by two. The time midpoints are calculated similarly, using the time data at the location of the peaks and valleys. Next, the linear trend is removed. The slope of the line to be subtracted is calculated by using the first and last position and time midpoints of the data. This line will be subtracted from both the data and the midpoints of the data (see Figures A6.2.1 a-c).

In order to minimize the introduction of artefacts in the analysis of forces acting on the balance during trend removal we only use the midpoints of the torsional oscillations, where the torque acting on the balance approach zero, to fit trends in the data.

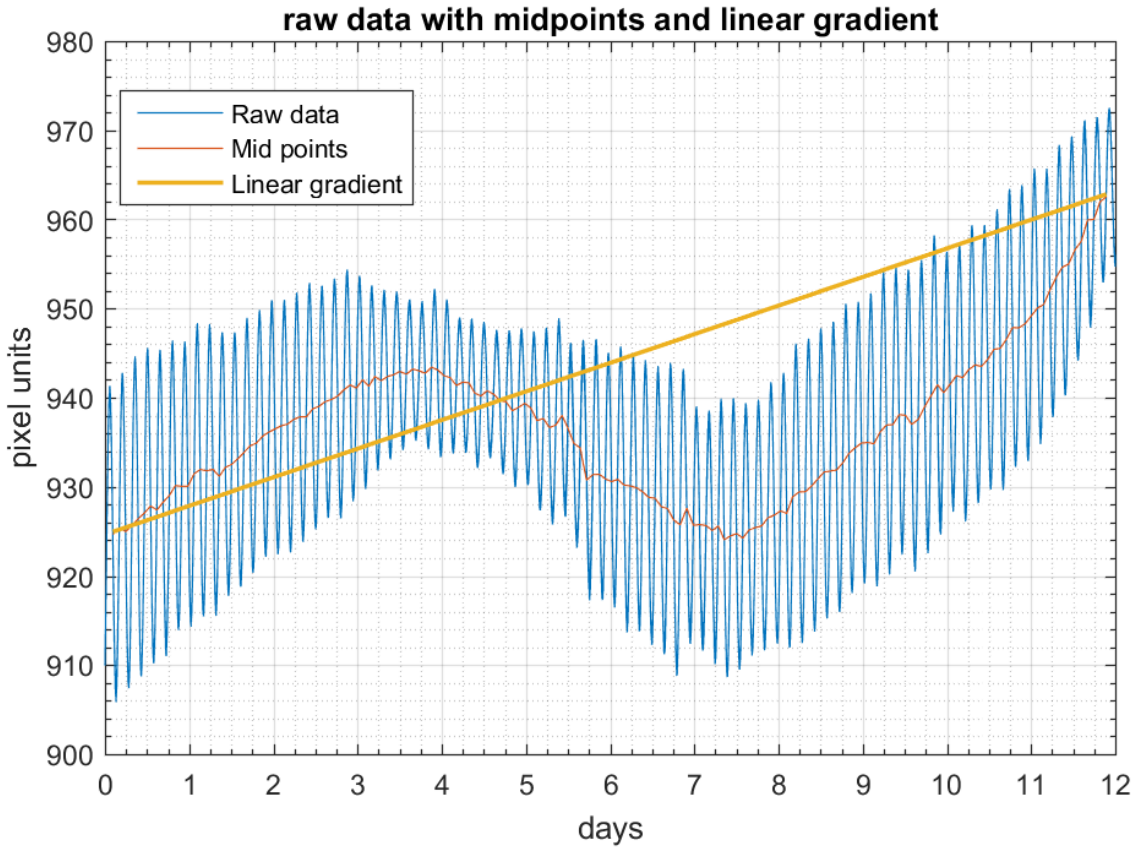

(a)

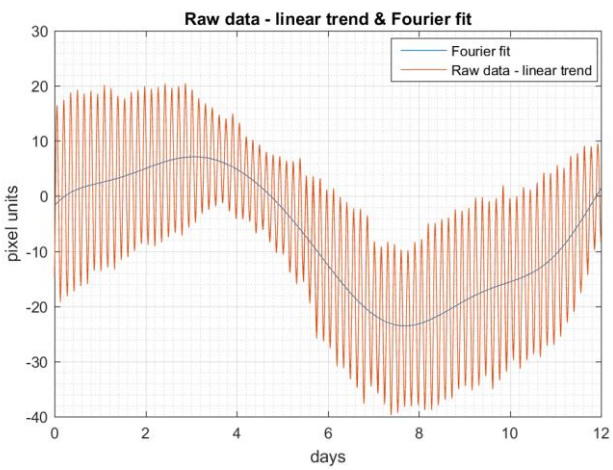

(b)

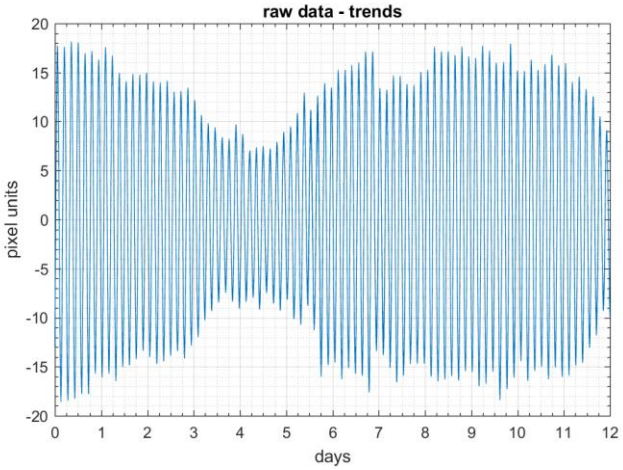

(c)

Figure A6.2.1: (a) Plot of data segment, linear trend and midpoints. (b) Plot of data segment and fit of midpoints after linear trend subtraction. (c) Detrended Data

The fitting model uses 5 sin terms and 5 cosine terms of a Fourier series to estimate and subtract the trend:

$$Fourier5(x) = a0 + \sum_{n=1}^{5} a_n \cos[n \times x \times w] + \sum_{n=1}^{5} b_n \sin[n \times x \times w] \quad \text{(A6.1)}$$

We must ensure that the frequencies being subtracted from the data are far removed from the signal frequency. In this example, the closest frequency subtracted from the data is: 2.306×10^{-5}, which is sufficiently removed from the diurnal and sidereal frequencies.

Coefficients	**Value of coefficients (with 95% confidence bounds)**
a0	-4.899 (-5.829, -3.969
a1	11.96 (10.13, 13.79)
b1	2.617 (-1.997, 7.232)
a2	-7.096 (-10.3, -3.894)
b2	-0.7568 (-5.655, 4.141)
a3	-1.523 (-2.332, -0.7132)
b3	-0.4052 (-3.391, 2.58
a4	-0.117 (-3.509, 3.275)
b4	1.928 (0.7279, 3.128)
a5	0.8937 (0.2402, 1.547)
b5	0.1129 (-1.463, 1.689)
w	4.612e-06 (4.112e-06, 5.112e-06)

Table A6.2.1: The parameters of the fit given by Equation 6.1, used to remove trends and drifts from the balance data

A6.2.2 Removal of Torsional Oscillations

Segment by Segment Fitting

This method removes the torsional oscillations by dividing each oscillation into segments and fitting each segment (see Figures A6.2.2a and A6.2.2b). Each segment can be fit well using a one-term exponential model, and I have used it as my fitting model for all the segments. Two "extreme" cases in the segmentation of the torsional oscillations occur at the location of a peak or valley, and the midpoint of the oscillation. Both cases shown are Figure A6.2.2.

A sub-segment consisting of several torsional oscillation is used to test this method. The results of the fit are shown in Figure A6.2.3. For each segment the fit will be subtracted from the data, removing the balance oscillations. This method did not work as well as desired, it caused distortion of the signal when implemented and a more carefully considered method of removing the oscillation was required.

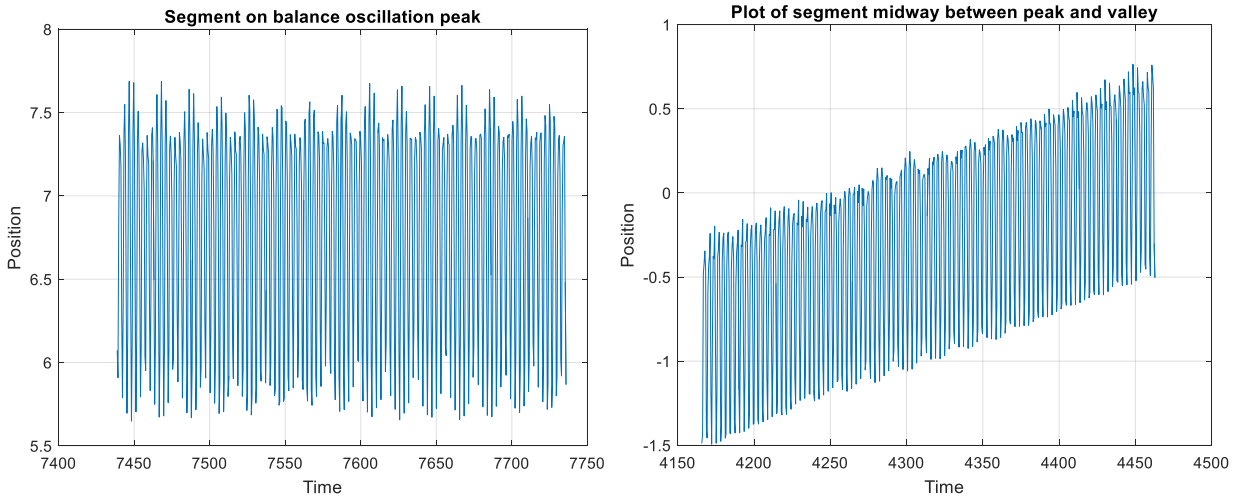

(a) (b)

Figure A6.2.2: (a) A data segment comprising a peak in torsional oscillations and (b) a segment located midway between a peak and a valley.

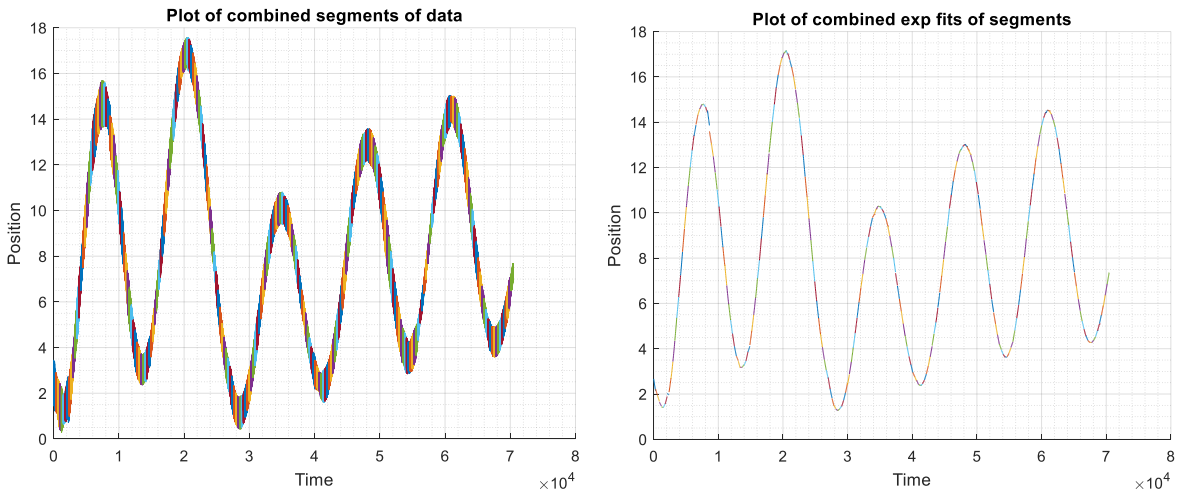

(a) (b)

Figure A6.2.3: (a) The data is segmented; each segment is plotted in a different color. (b) The balance oscillation reconstructed from the fit of each segment.

Half-Cycle Sinusoidal Fit

First, a smoothing procedure is applied to remove high-frequency oscillations. Then, a rough estimation of the peaks and valleys in the data is made using this smoothed data (see Figure A6.2.4). The data is divided into half-cycles using the locations of the peaks and valleys. However, the selection of the half-cycles can introduce noise into the system if the peaks and valleys are not chosen consistently and accurately. A quadratic fitting method is introduced to improve the selection of the peaks and valleys.

Using the rough estimate of the peak/valley location, a segment of the curve about this point, which comprising the peak or valley, is used to calculate the fit parameters. Then the time data in the segment is centered around the estimated peak location to improve the fit.

The following transformation is applied:

$$t \to x\colon\ x = t_{seg} - t_{p,v} \tag{A6.2}$$

The parameters of the fit are calculated by minimizing the square of the difference between the data and the fit:

$$\frac{\mathrm{d}}{\mathrm{d}a_{0,1,2}}\left(\sum_i d_i - (a_0 + a_1 x_i + a_2 x_i^2)\right)^2 = 0 \tag{A6.3}$$

Where d_i is the data. The coefficients a_0, a_1, and a_2 are obtained by solving Eq. 6.3 (Solution is given later in this section).

The location of the peak/valley is obtained by solving $\frac{\mathrm{d}}{\mathrm{d}x}(a_0 + a_1 x_i + a_2 x_i^2) = 0$:

$$x_{p,v} = -{}^{a_1}/_{2a_2} \tag{A6.4}$$

The location of the peak/valley is $x_{p,v} + t_{p,v}$. They are used to segment the data into half-cycles.

If the half-cycles are labelled by i, then each half-cycle is defined as the segment of the data corresponding to (see Figure A6.2.5):

- If i is odd:

$$\mathrm{hc_{i,odd}} = peaklocation\left(\frac{i+1}{2}\right) : valleylocation\left(\frac{i+1}{2}\right)$$

- If i is even:

$$\mathrm{hc_{i,even}} = valleylocation\left(\frac{i}{2}\right) : peaklocation\left(\frac{i}{2}+1\right)$$

The first half-cycle will begin at a peak, and the last half-cycle will end at a peak. There are 160 half-cycles in total in this segment of data.

Once the peaks and valleys have been accurately determined, the half-cycle will be fit using the original data (the data prior to smoothing). The fit model used is:

$$Fit(t) = a + b \times \sin\left[\frac{\pi}{t_f - t_0} \times (t - \bar{t})\right] \quad \text{(A6.6)}$$

$t = t_0, \ldots, t_f$ and $\bar{t} = \frac{t_f - t_0}{2}$. The parameters a and b are found by minimizing the least-squares difference:

$$\frac{\mathrm{d}}{\mathrm{d}(a,b)}\left(\sum_i d_i - (a + b \times \sin(t_i - \bar{t}))\right)^2 = 0 \quad \text{(A6.6)}$$

The solution to this equation is given below.

The sin term that is subtracted from the data averages out zero over the half-cycle (see Figures A6.2.6 for plots of half-cycles and the fit). The subtraction of this fit does preclude the direct extraction of the signal. This is because the component of the diurnal signal in each half-cycle is shifted and roughly centered about the zero-axis (see Figure A6.2.7).

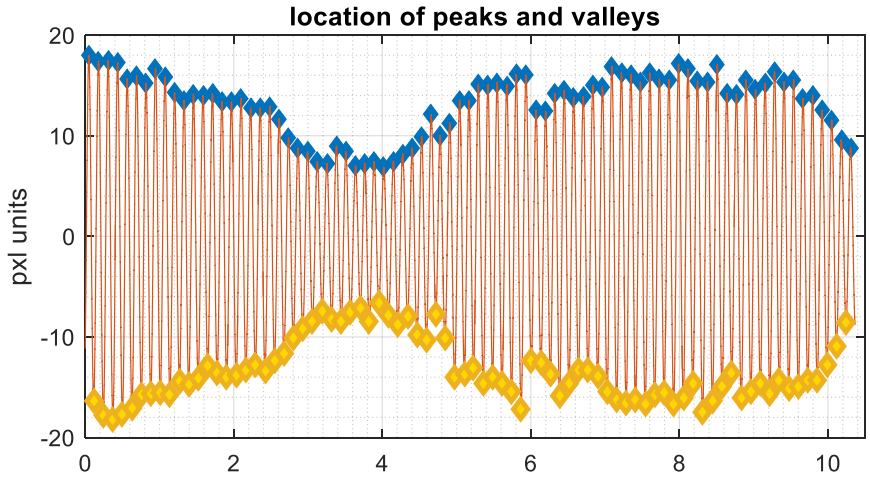

Figure A6.2.4: An estimation of the location of the peaks and valleys over 12-day data set.

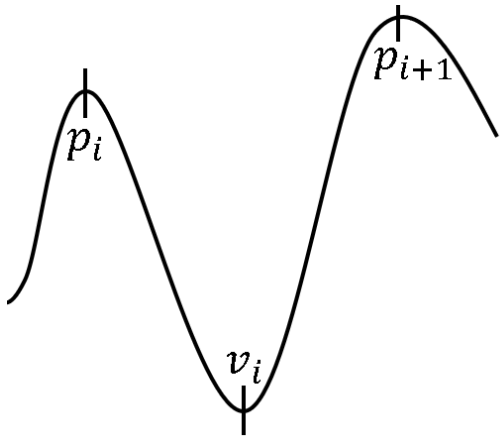

Figure S6.2.5: The first full cycle begins with a peak. Therefore, the downward slope of the first cycle starts at location p_i, and ends at location labelled by v_i. The upward slope begins at the location labelled by v_i and ends at the location of the next peak, labelled p_{i+1}.

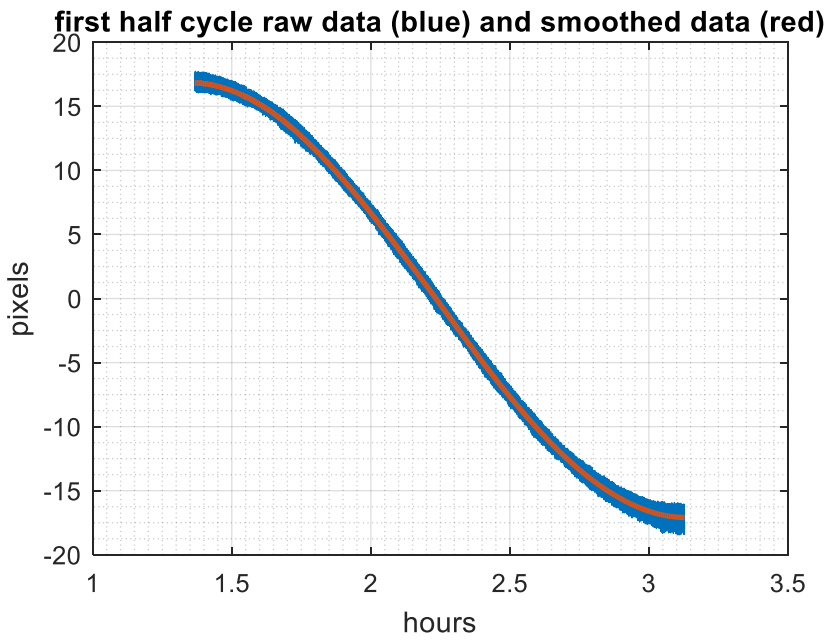

(a)

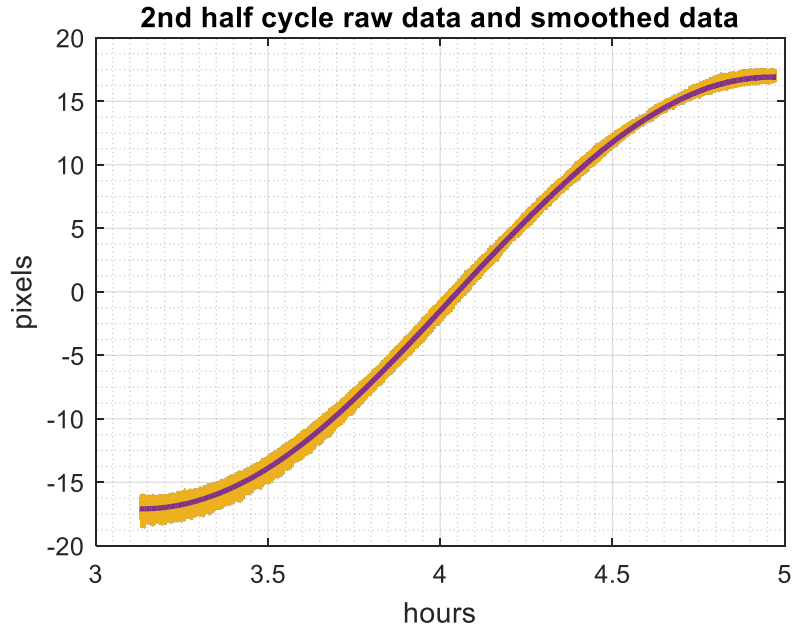

(b)

Figure A6.2.6: Plot of two half-cycles and their sinusoidal fits.

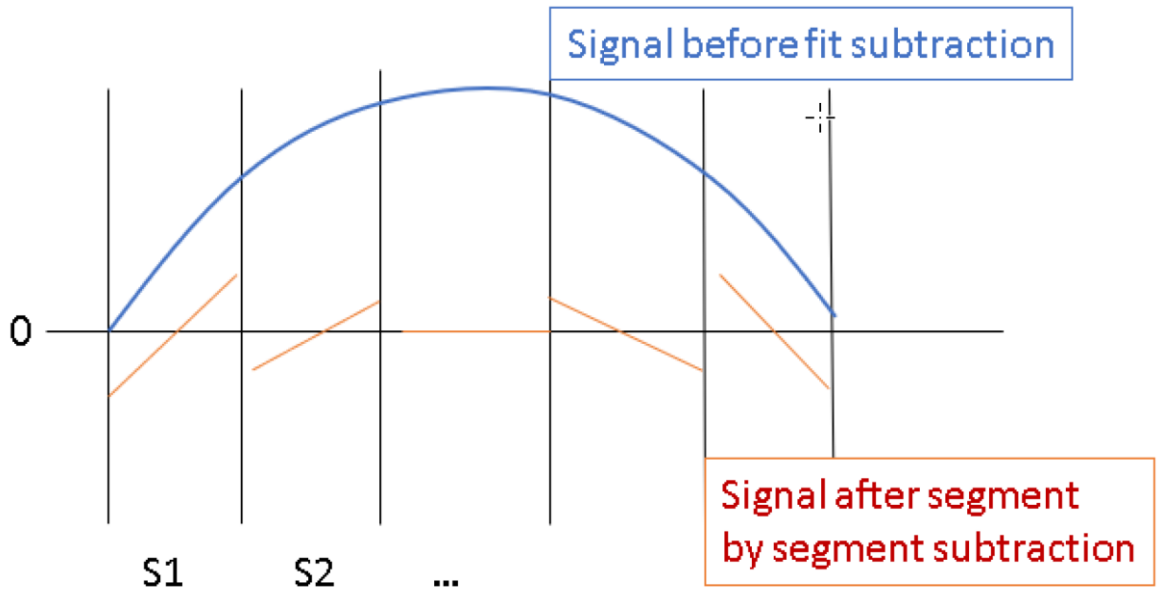

Figure A6.2.7: Effect of the subtraction of half-cycle fits on the signal. Each segment corresponds to a half-cycle.

The extraction of the amplitude of diurnal signals from the half-cycle segments must be obtained from the estimation of the average force acting on the balance over the half-cycle.

A6.2.3 Removal of High-frequency Oscillations

Fourier Terms Subtraction

The data will be separated into 400 second components and removed segment by segment. The last point in one segment will be the first point in the next segment, to keep continuity between segments.

The Fourier terms in each segment are calculated, and these segments are then subtracted from the data. Each term has a mean of zero are linear independence. Subtraction of these terms

should, theoretically, remove oscillatory signals in the segment with minimal distortion of the signal.

The Fourier terms whose Fourier coefficients were larger than 0.05 were chosen for subtraction from the data. For this data set, 6 frequencies for the sin and cosine terms were subtracted out (see Table A6.2.2). The fit of the high frequency oscillation are shown in Figure A6.2.7 and A6.2.8.

Sine frequencies	**Corresponding Sine amplitude**		**Cosine frequencies**	**Corresponding Cosine amplitudes**
0.326729584275798	0.0626168634135528		0.326885578348023	-0.107152034190069
0.326885578348023	0.142248512702126		0.326963575384135	-0.211939850774014
0.326963575384135	-0.238215034982217		0.327041572420248	0.192062767934582
0.327041572420248	-0.133705442235289		0.327197566492473	0.0635541481463025
0.377427657749006	0.101422145528972		0.377349660712893	0.0714029112450994
0.377505654785118	0.0521986499072465		0.377427657749006	0.062753249451748

Table A6.2.2: Fit of High-frequency Oscillations using Fourier Terms: The frequencies $\left(f_{pend} = \frac{\omega_{pend}}{2\pi}\right)$ with the amplitudes of the six largest coefficients of the sin and cosine terms.

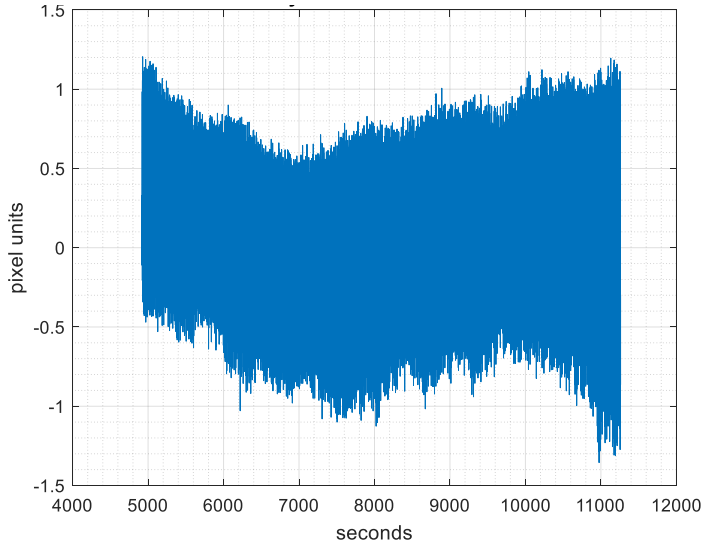

Figure A6.2.8: Plot of the high-frequency oscillation during a half-cycle

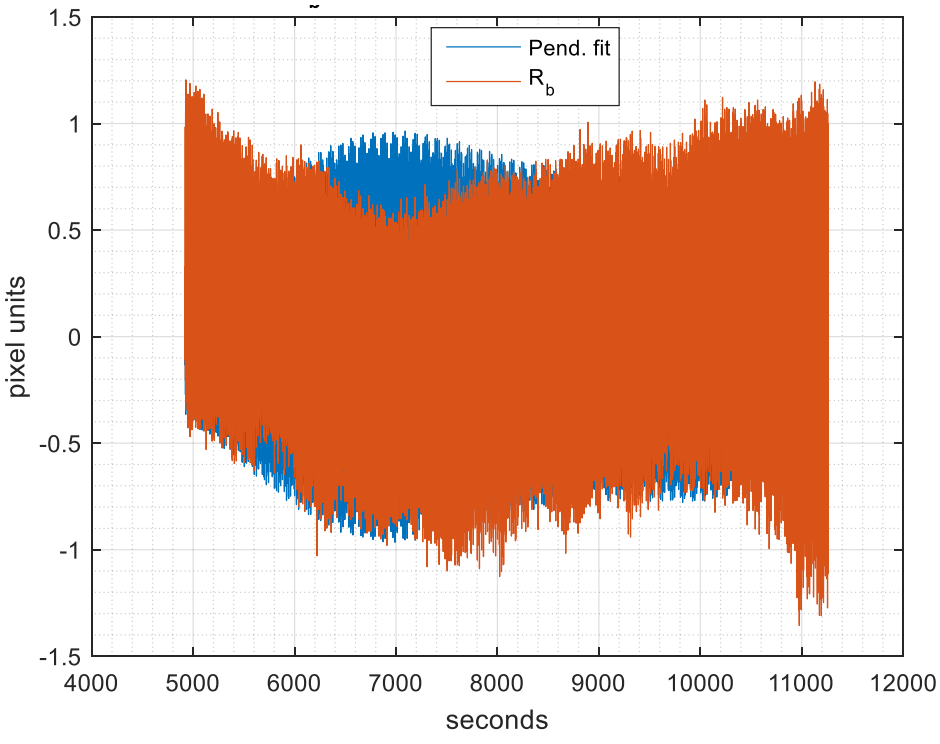

(a)

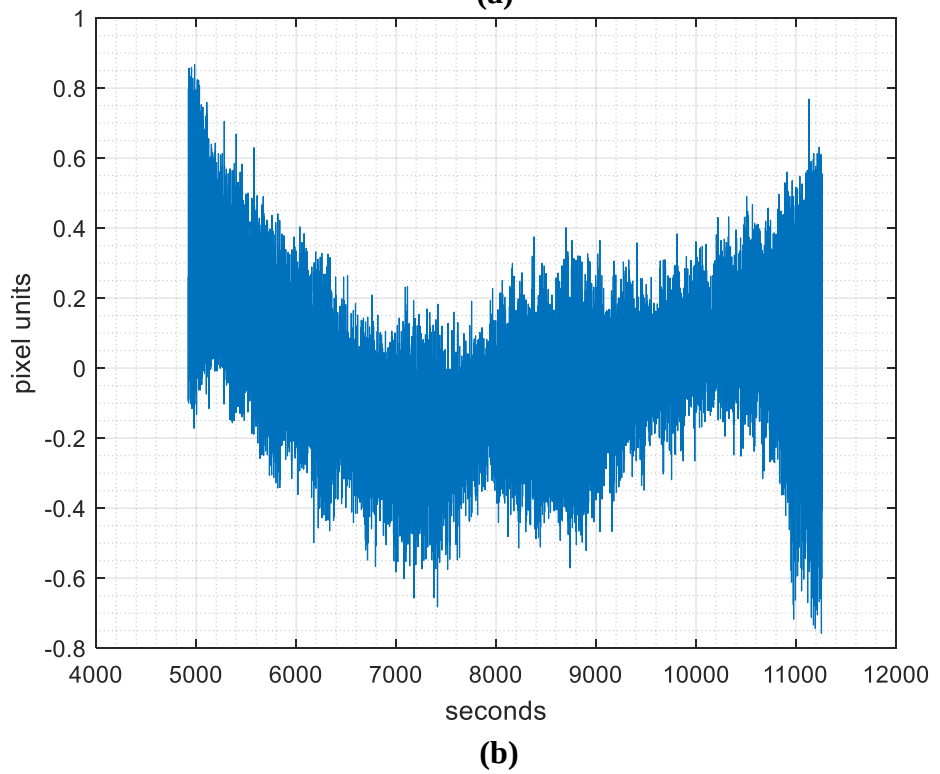

(b)

Figure A6.2.9: Plot of a segment with the torsional oscillations removed, the high-frequency oscillations are observed. (a) Plot of the data (labelled R_b) and its fit to the high-frequency oscillations (labelled Pend. Fit).(b) Plot of the difference between the data and the fit.

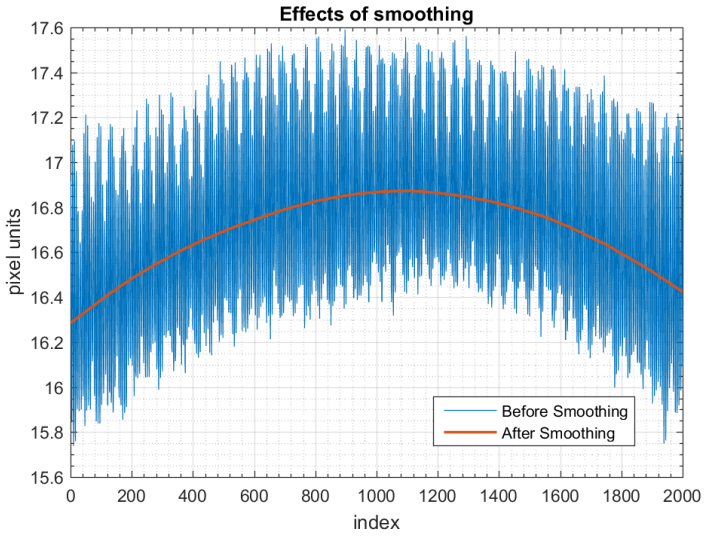

Figure A.6.10: The smoothing window usd 1001 points, 500 before the point of interest and 500 points after the point of interest.

Removal of High-frequency Oscillations using Smoothing

The pendular oscillations are removed by smoothing the data. The smoothing window usd 1001 points, 500 before the point of interest and 500 points after the point of interest. A close up of the plot of the data before and after smoothing is shown in Figure A6.2.9. The smoothing time constant is on the order of 5 mins, which is negligable in comparison to the roughly one day period of the EP-violating signals that we are interested in measuring.

A6.2.4 Signal Extraction from Calculation of Mean Acceleration

After the removal of the torsional and high frequency oscillations, the signal must be calculated by estimating the mean acceleration of the balance over a cycle or half-cycle. As

discussed in the previous section, the asymmetries and deviations in the torsional oscillation from a sinusoidal form are induced by external forces.

The second gradient of these features are also preserved during subtraction of the torsional oscillations and the high frequency oscillations and are a source of noise in the estimation of the mean acceleration. They present a significant challenge in the extraction of the signal.

Calculation of the 2nd Gradient

Once the residuals have been obtained, the half cycle is divided into 3 segments. This is done by dividing the length of the data segment by 3, rounding down to the nearest integer, and using this value to create 3 segments from the data. Then the mean of each segments is calculated, they are used to estimate the second gradient of the half cycle:

$$\ddot{\phi} = (mean_{seg1} + mean_{seg3} - 2 \times mean_{seg2})/(\Delta t_{hc}/3)^2 \qquad \text{(A6.9)}$$

The time associated with a value of the second gradient will be determined by taking the mean of the time range over which the half-cycle for which the second gradient was calculated.

The signal could not be recovered from this method. The attenuation of the signal is too great for practical application. The averaging procedure did not successfully remove the noise in the acceleration while retaining the signal.

Extraction Using a Sin Fit

This method extracts the mean acceleration by fitting the segment to a sin function with the same frequency as the EP-violating signal. First, the data is divided into 12 segments, and averaged. This method is demonstrated using the residual data (data after the removal of the torsional oscillations and high-frequency oscillations) from Figure 6.11b.

Next, this averaged residual data is fit using the following model:

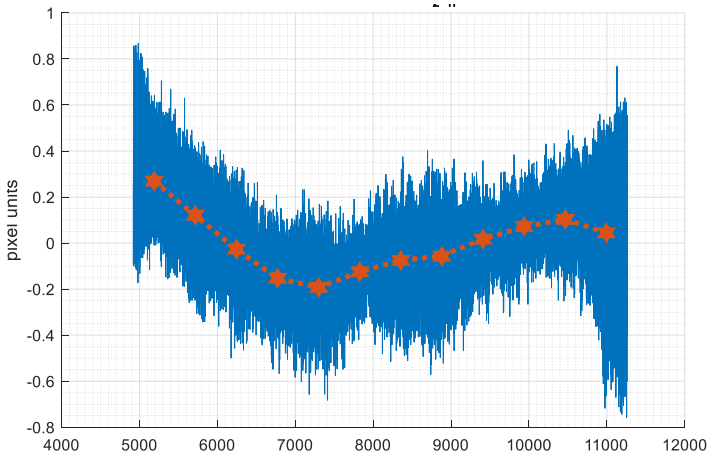

Figure A6.2.11: The residual data is divided into 12 segments and averaged. The averages of the segments are given by the line in red.

$$x + a \times \sin\left(\phi + \omega_{EP} \times (\overline{t_n} - t_0)\right) \tag{A6.10}$$

$\overline{t_n}$ is the mean time of segment *n*, t_0 is the initial time value of the half-cycle, and ϕ is the phase of the EP-violating signal at the initial time of the half cycle: $\phi = \omega_{EP} \times (t_0 - t_{zero})$, t_{zero} is the last time when the EP-violating signal was equal zero (e.g. midnight for a diurnal signal).

The expressions for x and a are found by minimizing the square of difference between the data and the fit (the solution is given below)

$$\frac{\mathrm{d}}{\mathrm{d}(a,b)}\left(\sum_n \bar{d}_n - \left(x + a \times \sin\left(\phi + \omega_{EP} \times (\bar{t_n} - t_0)\right)\right)\right)^2 = 0 \quad \text{(A6.11)}$$

$\bar{d}_n$is the mean residual data. he mean acceleration induced by the signal over the half cycle is:

$$\langle a \rangle_{h.c} = -\omega_{EP}^2 \times A_{EP} \times \sin\left(\phi + \omega_{EP} \times (\bar{t} - t_0)\right) \quad \text{(A6.12)}$$

$\bar{t}$ is the mean of the time data in the half-cycle.

Extraction using a Legendre Fit

The average acceleration acting on the balance will be estimated by fitting the residual data to Legendre polynomials, and obtained from the coefficient of the second order term of the fit. The fit is calculated using Legendre polynomials up to the 3rd order.

The Legendre polynomials are an orthonormal set of odd and even functions defined in the domain $[-1,1]$. These properties are ideal for this segment by segment analysis. Each half-cycle segment can be expanded using Legendre polynomials in a natural way. We map the time axis to the domain of the Legendre polynomials. If t_o denotes the initial time and t_f the final time, we define x_i as:

$$x_i = \frac{t_i - \bar{t}}{\Delta t/2} \quad \text{(A6.13)}$$

Where: $\bar{t} = \frac{t_o + t_f}{2}$ and $\Delta t = t_f - t_0$

The fit is defined as:

$$\phi(x_i) \approx \sum_{k=0}^{3} a_k \times P(k, x_i) \tag{A6.14}$$

The coefficients of the fit are calculated determined by taking the inner product:

$$a_k = \frac{\sum_{i=1}^{N} d_i \times P(k,x_i)}{\sum_{i=1}^{N} \left(P(k,x_i)\right)^2} \tag{A6.15}$$

Where d_i is the data. See Figure A6.2.11 for a plot of the fit.

The mean acceleration is obtained by taking the second derivative of Eq. 6.14:

$$\ddot{\phi} \approx \frac{\mathrm{d}^2}{\mathrm{d}x^2} \sum_{k=0}^{3} a_k \times P(k, x_i) = 3a_2 + 15 x_i a_3 \tag{A6.16}$$

When the averaged over the half-cycle, only the coefficient of the second order term survives:

$$\langle \ddot{\phi} \rangle \approx 3a_2 \tag{A6.17}$$

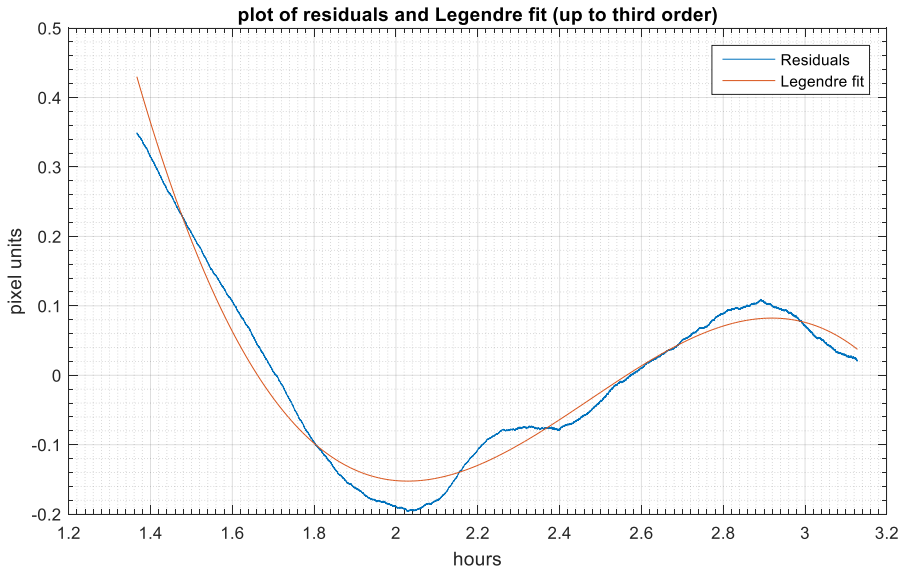

Figure A6.2.12: A plot of the residual data and its Legendre fit. The high-frequency oscillations in this example was removed using smoothing. This fit corresponds to the first half-cycle shown above in Figure A6.2.9(a)

Conclusion

The efficacy of the methods described in this section were measured by their ability to extract and an artificially generated EP-violating signal introduced into the data. When tested, these methods failed to adequately extract the signal.

After consideration of the properties of the balance and its response to external forces, a method of estimating the mean acceleration of the balance that can successfully extract an artificial EP-violating signals introduced into the data with an acceptably low attenuation.

Solution to Equation A6.3

Expanding Equation 6.3, we obtain the following system of equations:

$$a_2 \sum_i x_i^4 + a_1 \sum_i x_i^3 + a_0 \sum_i x_i^2 = \sum_i d_i \times x_i^2$$

$$a_2 \sum_i x_i^3 + a_1 \sum_i x_i^2 + a_0 \sum_i x_i = \sum_i d_i \times x_i$$

$$a_2 \sum_i x_i^2 + a_1 \sum_i x_i + a_0 N = \sum_i d_i$$

We define:

$S_1 \equiv \sum_i x_i$, $S_2 \equiv \sum_i x_i^2$, $S_3 \equiv \sum_i x_i^3$, $S_4 \equiv \sum_i x_i^4$, $D_{x_0} \equiv \sum_i d_i$, $D_{x_1} \equiv \sum_i d_i \times x_i$, and

$D_{x_2} \equiv \sum_i d_i \times x_i^2$

The solution to this system of equations is:

$$a_2 = \frac{D_{x_2}(S_1^2 - NS_2) + D_{x_1}(NS_3 - S_1S_2) + D_{x_0}(S_2^2 - S_1S_3)}{S_2^2 - 2S_2S_2S_3 + NS_3^2 + S_1^2S_4 - NS_2S_4}$$

$$a_1 = \frac{D_{x_2}(NS_3 - S_1S_2) + D_{x_1}(S_2^2 - NS_4) + D_{x_0}(S_1S_4 - S_2S_3)}{S_2^2 - 2S_2S_2S_3 + NS_3^2 + S_1^2S_4 - NS_2S_4}$$

$$a_0 = \frac{D_{x_2}(S_2^2 - S_1S_3) + D_{x_1}(S_1S_4 - S_2S_3) + D_{x_0}(S_3^2 - S_2S_4)}{S_2^2 - 2S_2S_2S_3 + NS_3^2 + S_1^2S_4 - NS_2S_4}$$

Solution to Equation A6.6

We set $\omega_{h.c} \equiv \frac{\pi}{t_f - t_0}$ and $\Delta t_i \equiv t_i - \bar{t}$. N is the number of data points in the segment. Expanding Equation 6.6, we obtain the following system of equations:

$$aN + b\sum_i \sin(\omega_{h.c}\Delta t_i) = \sum_i d_i$$

$$a\sum_i \sin(\omega_{h.c}\Delta t_i) + b\sum_i \sin^2(\omega_{h.c}\Delta t_i) = \sum_i d_i \sin(\omega_{h.c}\Delta t_i)$$

The solution to this system of equations is:

$$a = \frac{\sum_i d_i \times \sum_i \sin^2(\omega_{h.c}\Delta t_i) - \sum_i d_i \sin(\omega_{h.c}\Delta t_i) \times \sum_i \sin(\omega_{h.c}\Delta t_i)}{N\sum_i \sin^2(\omega_{h.c}\Delta t_i) - (\sum_i \sin(\omega_{h.c}\Delta t_i))^2}$$

$$b = \frac{N\sum_i d_i \sin(\omega_{h.c}\Delta t_i) - \sum_i d_i \times \sum_i \sin(\omega_{h.c}\Delta t_i)}{N\sum_i \sin^2(\omega_{h.c}\Delta t_i) - (\sum_i \sin(\omega_{h.c}\Delta t_i))^2}$$

Solution to Equation A6.11

We set $\Delta t_n \equiv \bar{t_n} - \bar{t}$. N is the number of data points in the segment. The system of equations to be solved is:

$$a\sum_n \sin^2[\phi + \omega_{EP}\Delta t_n] + x\sum_n \sin[\phi + \omega_{EP}\Delta t_n] = \sum_n \bar{d}_n \sin[\phi + \omega_{EP}\Delta t_n]$$

$$a\sum_n \sin[\phi + \omega_{EP}\Delta t_n] + 12x = \sum_n \bar{d}_n$$

We define:

$S_2 \equiv \sum_n \sin^2[\phi + \omega_{EP}\Delta t_n]$, $\quad S \equiv \sum_n \sin[\phi + \omega_{EP}\Delta t_n]$,

$D \equiv \sum_n \bar{d}_n$, and $\quad D_s \equiv \sum_n \bar{d}_n \sin[\phi + \omega_{EP}\Delta t_n]$

The solution to this system of equations is:

$$a = \frac{D \times S - 12D_s}{S^2 - 12S_2}$$

$$x = \frac{D_s \times S - D \times S_2}{S^2 - 12S_2}$$

References

[1] Einstein, A. (1907). On the relativity principle and the conclusions drawn from it. Jahrbuch der Radioaktivität und Elektronik, 4, 411-462.

[2] Clifford M. Will. *Theory and Experimentation in Gravitational Physics.* Cambridge University Press 1993.

[3] Will, C. M. (2009). The confrontation between general relativity and experiment. *Proceedings of the International Astronomical Union*. https://doi.org/10.1017/S174392130999038X.

[4] Dicke, R. H. (1964). *The Theoretical Significance of Experimental Relativity*. Retrieved from https://philpapers.org/rec/DICTTS

[5] Schiff, L. I. (1960). On Experimental Tests of the General Theory of Relativity. *American Journal of Physics*, *28*(4), 340–343. https://doi.org/10.1119/1.1935800

[6] Abercrombie, M. D. *Development of a Long-Period Torsion Balance for Tests of Einstein's Equivalence Principle and a Search for Normal Mode Torsional Oscillations of the Earth*. PhD thesis. Washington University in St. Louis, 2016.

[7] S. Weinberg. *Gravitation and Cosmology*. John Wiley & Sons, New York, 1972.

[8[Adelberger, E. G., Gundlach, J. H., Heckel, B. R., Hoedl, S., & Schlamminger, S. (2009). Torsion balance experiments: A low-energy frontier of particle physics. *Progress in Particle and Nuclear Physics*. https://doi.org/10.1016/j.ppnp.2008.08.002

[9] Braginsky, V. B., Manukin, A. B., & Keiser, G. M. (2005). Measurement of Weak Forces in Physics Experiments. *American Journal of Physics*. https://doi.org/10.1119/1.11161

[10] Su, Y. (1992). A New Test of the Weak Equivalence Principle. *Thesis (PH.D.) -- UNIVERSITY OF WASHINGTON, 1992.Source: Dissertation Abstracts International, Volume: 54-01, Section: B, Page: 0281.* Retrieved from http://adsabs.harvard.edu/abs/1992PhDT.....326S

[11] Wagner, T. A., Schlamminger, S., Gundlach, J. H., & Adelberger, E. G. (2012). *Torsion-balance tests of the weak equivalence principle*.

[12] Todd A. Wagner. *Rotating Torsion Balance Tests of the Weak Equivalence Principle.* PhD thesis, University of Washington, 2013.

[13] Nordtvedt, K. (1975). Quantitative relationship between clock gravitational “red-shift”; violations and nonuniversality of free-fall rates in nonmetric theories of gravity. *Physical Review D*, *11*(2), 245–247. https://doi.org/10.1103/PhysRevD.11.245

[14] Haugan, M. P. (1979). Energy conservation and the principle of equivalence. *Annals of Physics*, *118*(1), 156–186. https://doi.org/10.1016/0003-4916(79)90238-0

[15] Pound, R. V., & Rebka, G. A. (1960). Apparent Weight of Photons. *Physical Review Letters*, *4*(7), 337–341. https://doi.org/10.1103/PhysRevLett.4.337

[16] Amorim, A., Bauböck, M., Berger, J. P., Brandner, W., Clénet, Y., Coudé du Foresto, V., … Yazici, S. (2019). Test of the Einstein Equivalence Principle near the Galactic Center Supermassive Black Hole. *Physical Review Letters*, *122*(10), 101102. https://doi.org/10.1103/PhysRevLett.122.101102

[17] Will, C. M. (n.d.). *Covariant calculation of general relativistic effects in an orbiting gyroscope experiment*. https://doi.org/10.1103/PhysRevD.67.062003

[18] Everitt, C. W. F., DeBra, D. B., Parkinson, B. W., Turneaure, J. P., Conklin, J. W., Heifetz, M. I., … Wang, S. (2011). Gravity Probe B: Final Results of a Space Experiment to Test General Relativity. *Physical Review Letters*, *106*(22), 221101. https://doi.org/10.1103/PhysRevLett.106.221101

[19] Damour, T. (1996). Testing the equivalence principle: why and how? *Classical and Quantum Gravity*, *13*(11A), A33–A41. https://doi.org/10.1088/0264-9381/13/11A/005

[20] Damour, T. (2001). Questioning the equivalence principle. *Comptes Rendus de l'Académie Des Sciences - Series IV - Physics*, *2*(9), 1249–1256. https://doi.org/10.1016/S1296-2147(01)01272-0

[21] Damour, T., & Donoghue, J. F. (2010). *Equivalence Principle Violations and Couplings of a Light Dilaton*. Retrieved from https://scholarworks.umass.edu/physics_faculty_pubs

[22] Schlamminger, S., Choi, K.-Y., Wagner, T. A., Gundlach, J. H., & Adelberger, E. G. (n.d.). *Test of the Equivalence Principle Using a Rotating Torsion Balance*. https://doi.org/10.1103/PhysRevLett.100.041101

[23] Adelberger, E. G., Stubbs, C. W., Heckel, B. R., Su, Y., Swanson, H. E., Smith, G., … Rogers, W. F. (1990). Testing the equivalence principle in the field of the Earth: Particle physics at masses below 1 μeV? *Physical Review D*, *42*(10), 3267–3292. https://doi.org/10.1103/PhysRevD.42.3267

[24] Chen, Y.T. & H. Cook, Alan. (2019). Gravitational Experiments in the Laboratory. Y.T. Chen, A.H. Cook.

[25] Gillies, G. T., & Ritter, R. C. (1993). Torsion balances, torsion pendulums, and related devices. *Citation: Review of Scientific Instruments*, *64*(283). https://doi.org/10.1063/1.1144248

[26] Kovalik, J., & Saulson, P. R. (1993). Mechanical loss in fibers for low noise pendulums. *Review of Scientific Instruments*, *64*(10), 2942. https://doi.org/10.1063/1.1144388

[27] Ritter, R. C., Winkler, L. I., Gillies, G. T., 1798, C. H., A, V. der Z., W, M. C., … T, R. R. C. and G. G. (1999). Precision limits of the modern Cavendish device: thermal noise measurement regimes and strategies in the torsion pendulum. *Measurement Science and Technology*, *10*(6), 499–507. https://doi.org/10.1088/0957-0233/10/6/315

[28] Roll, P., Krotkov, R., & Dicke, R. (1964). The equivalence of inertial and passive gravitational mass. *Annals of Physics*, *26*(3), 442–517. https://doi.org/10.1016/0003-4916(64)90259-3

[29] Saulson, P. R. (1990). Thermal noise in mechanical experiments. *Physical Review D*, *42*(8), 2437–2445. https://doi.org/10.1103/PhysRevD.42.2437

[30] Adelberger, E. G., Heckel, B. R., & Nelson, A. E. (2003). TESTS OF THE GRAVITATIONAL INVERSE-SQUARE LAW. *Annual Review of Nuclear and Particle Science*, *53*(1), 77–121. https://doi.org/10.1146/annurev.nucl.53.041002.110503

[31] Abbott, B. P., Abbott, R., Adhikari, R., Ajith, P., Allen, B., Allen, G., … Zweizig, J. (2009). LIGO: the Laser Interferometer Gravitational-Wave Observatory. *Reports on Progress in Physics*, *72*(7), 076901. https://doi.org/10.1088/0034-4885/72/7/076901

[32] Marchesoni, F., Cagnoli, G., & Gammaitoni, L. (1994). Damping in low-frequency mechanical pendulums. *Physics Letters A*, *187*(5), 359–364. https://doi.org/10.1016/0375-9601(94)91109-6

[33] González, G. I., & Saulson, P. R. (1994). Brownian motion of a mass suspended by an anelastic wire. *The Journal of the Acoustical Society of America*, *96*(1), 207. https://doi.org/10.1121/1.410467

[34] Callen, H. B., & Welton, T. A. (1951). Irreversibility and generalized noise. *Physical Review*. https://doi.org/10.1103/PhysRev.83.34

[35] Callen, H. B., & Greene, R. F. (1952). On a theorem of irreversible thermodynamics. *Physical/ Review*. https://doi.org/10.1103/PhysRev.86.702

[36] Greene, R. F., & Callen, H. B. (1952). On a theorem of irreversible thermodynamics. II. *Physical Review*. https://doi.org/10.1103/PhysRev.88.1387

[37] Cowsik, R., Srinivasan, R., Kasturirengan, S., Kumar, A. S., & Wagoner, K. (2007). Design and performance of a sub-nanoradian resolution autocollimating optical lever. *Citation: Review of Scientific Instruments*, *78*. https://doi.org/10.1063/1.2714044

[38] Arp, T. B., Hagedorn, C. A., Schlamminger, S., & Gundlach, J. H. (2013). A reference-beam autocollimator with nanoradian sensitivity from mHz to kHz and dynamic range of 10^7. *Review of Scientific Instruments*, *84*(9), 095007. https://doi.org/10.1063/1.4821653

[39] Ellis, G. (2012). *Control system design guide: using your computer to understand and diagnose feedback controllers*. Retrieved from https://www.sciencedirect.com/book/9780123859204/control-system-design-guide

[40] Burch, B., & Cowsik, R. (2013). PROPERTIES OF GALACTIC DARK MATTER: CONSTRAINTS FROM ASTRONOMICAL OBSERVATIONS. *The Astrophysical Journal*, *779*(1), 35. https://doi.org/10.1088/0004-637X/779/1/35

[41] JPL Horizons webpage. ssd.jpl.nasa.gov/?horizons.

[42] Miller, A. H. (1934). The Theory and Operation of the Eötvös Torsion Balance with Plates I, II, III. In *Journal of the Royal Astronomical Society of Canada, Vol. 28, p.1* (Vol. 28). Retrieved from http://adsabs.harvard.edu/abs/1934JRASC..28....1M

[43] Misner, C. W., Thorne, K. S., & Wheeler, J. A. (1973). *Gravitation*.

[44] Nobili, A., & Anselmi, A. (2018). Relevance of the weak equivalence principle and experiments to test it: Lessons from the past and improvements expected in space. *Physics Letters A*, *382*(33), 2205–2218. https://doi.org/10.1016/J.PHYSLETA.2017.09.027

[45] Stubbs, C. W. (1993). Experimental limits on any long range nongravitational interaction between dark matter and ordinary matter. *Physical Review Letters*, *70*(2), 119–122. https://doi.org/10.1103/PhysRevLett.70.119

[46] Dark matter | CERN. (n.d.). Retrieved April 10, 2019, from https://home.cern/science/physics/dark-matter

[47] Fan, X.-D., Liu, Q., Liu, L.-X., Milyukov, V., & Luo, J. (2008). Coupled modes of the torsion pendulum. In *Physics Letters A* (Vol. 372). https://doi.org/10.1016/j.physleta.2007.08.020

[48] Liang, Z., Ying, T., Bang-Ming, G., Zhong-Kun, H., & Jun, L. (2003). An Abnormal Vibrational Mode of Torsion Pendulum. *Chinese Physics Letters*, *20*(8), 1206–1209. https://doi.org/10.1088/0256-307X/20/8/306

[49] Tu, Y., Zhao, L., Liu, Q., Ye, H.-L., & Luo, J. (2004). An abnormal mode of torsion pendulum and its suppression. *Physics Letters A*, *331*(6), 354–360. https://doi.org/10.1016/j.physleta.2004.09.007

[50] Ciufolini, I., & Wheeler, J. A. (1995). *Gravitation and inertia*. Retrieved from https://press.princeton.edu/titles/5635.html

[51] Bergé, J., Touboul, P., & Rodrigues, M. (2015). *Status of MICROSCOPE, a mission to test the Equivalence Principle in space*. Retrieved from http://www.ego-gw.it